Sensitizing Erbium with Nanocrystals

Jensen, Rasmus Vincentz Skougaard

Publication date:
2012

Document Version
Early version, also known as pre-print

Sensitizing Erbium with Nanocrystals

PhD Thesis

Rasmus Vincentz Skougaard Jensen

Aalborg University

June 29, 2012

Preface

This thesis marks the end and summary of my three years of Ph.D. studies at Aalborg University. It has been a time rich with all kinds of challenges and revelations about the nature of physics. This process has been helped immensely by a large number of people, through their caring, support and help, that I wish to thank them for.

Firstly I would like to thank Thomas Garm Pedersen for giving me the oppurtunity to undertake this project and skillfully supervising it, I have very much enjoyed Thomas' "do you have a blackboard and five minutes" approach to physics. The Serbina project members, Brian Julsgaard, Ying-Wei Lu, Arne Nylandsted Larsen, Kjeld Pedersen and Brian Bech Nielsen have all contributed to fruitful and excellent discussions at our meetings. In particular I would like to thank Ying-Wei Lu for providing me with excellent samples and Brian Julsgaard for his advice on optical setups. Everyday life at the department has been enjoyable, in particular I would like to thank Jesper Gadegaard, Thöger Kari Jensen, Peter Kjär Kristensen, Jens Rafaelsen and Esben Skousen for many nice discussions as well as laboratory assistance. In particular I would also like to thank Troels F. Rönnow, we have shared offices for nearly 8 years and I am grateful for all our talks, both related to work- and private life.

Aside from work, my free time has been enriched by the lovely people in Cycling Nord, you have all been a good support and excellent time in midst of the studies. In particular I would like to thank Henrik Thostrup Jensen for his advice on academia, plus many fun discussions and rides.

Finally I would like to thank my family and not the least my girlfriend Trine Marie Dippel. Your continued support and love through the ups and downs of this project has been amazing.

Contents

Chapter 1

General Introduction

Ever since the commercialization of the silicon transistor, silicon became and has been the stable work horse of the electronics industry, thanks to its excellent electronic properties and the ease of growing useful oxide layers. Today a modern computer chip can contain more than a billion transistors, each having a footprint less than 0.2 μm^2, illustrating the giant leaps silicon technology has made ever since its birth, as boldly predicted by Moore's law. In many ways, silicon is the ideal material for electronics manufacture, its conductance may be varied over orders of magnitude by the addition of dopants and its oxide is very stable and highly insulating. In addition it is very abundant, thus cheap, and may be processed to high purity with relative ease.

However, as the boundaries keep on being pushed, heat generation and bandwidth limitations from thin interconnects need to be addressed. A possible solution is optical interconnects and passive components integrated onto the chip. Whereas waveguides are quite easy to realise in silicon dioxide, integrating a light emitter onto silicon circuitry is not trivial. The indirect band gap nature of silicon makes it a poor choice for an optical source, instead direct band gap sources such as GaAs are much preferred. While it is possible to integrate a GaAs emitter onto silicon, this task is neither cheap nor comercially very viable. Thus, to make silicon truely viable for integrated optoelectronics an active, optical medium that can be readily integrated is needed.

One approach towards realizing a direct gap material that may be integrated readily with silicon technology is to nanostructure silicon. By forming small clusters of silicon in a suitable matrix, eg. silica, the carriers are greatly confined, leading to new physical properties inbetween that of a bulk material

and a molecule. Such a material may have a pseudo direct band gap greater than that of bulk silicon, typically corresponding to 600-900 nm emission. To tune this emission towards wavelengths commonly used for telecommunications, around 1530 nm, a dopant such as erbium may be introduced into the matrix. As it turns out, the small clusters act as sensitizers of the otherwise very weakly absorbing erbium ions and the first steps towards an integrated emitter have been taken. Operation at this wavelength has the added benefit of being in the low-loss window of silica.

The work in this thesis has been focused on the generation of 1530 nm light from silica films, doped with Er, sensitized by Si clusters. As an alternative, optical properties of α-Sn nanoparticles are investigated as they may be a direct route to this light generation. The second chapter serves as an introduction to the field and summarizes some of the results on silicon nanocrystals and erbium in silica, both the isolated and complete systems. A brief introduction to α-Sn is also given. The third chapter gives a brief introduction to tight binding and density functional theory, which are used for obtaining optical properties for α-Sn nanocrystals. Chapter four summarises the theoretical results obtained for both bulk and nanocrystalline α-Sn along with Si-Sn alloys, based on papers I, III and IV. Chapter five is a summary of the experimental results on particularly the interaction between silicon clusters and erbium in papers II and V, as well as a number of unpublished results on the SiO_2:Er and Si-nc/SiO_2:Er system.

Chapter 2

The Nanocrystal-Erbium System

2.1 Silicon Nanocrystals

The realization of effective photoluminescence from silicon-based structures dates back to 1990, when the first paper on porous silicon was published[1], where the confinement of carriers leads to a pseudo-direct band gap behaviour of silicon. This also paved the way for the first LEDs based on silicon as the active material[2,3]. By varying process parameters, it is possible to tune the size of the nanocrystallites in the porous silicon and thus also the optical and electrical properties[4]. While porous silicon continues to be an active field of research, it has seen limited commercial application for a number of reasons; notably the electrochemical etching process is somewhat undesirable in a production environment, as well as reproducibility and material degradation being issues[5].
Following this initial demonstration of quantum confined carriers leading to improved optical properties of silicon, several routes towards nanocrystalline silicon have been demonstrated, both by an aerosol process[6] or by deposition of a thin film of silicon rich silicon dioxide. The principle behind the thin film method is that at an equilibrium state, silicon will tend to seperate from the oxide[7] and as long as the diffusion length of silicon is not too long, it will tend to form into nanocrystals in the oxide. In the following, different routes towards producing silicon nanocrystals in thin film will be discussed. Following this the photoluminescence properties in both steady state and under pulsed excitation will be discussed. Finally we will briefly look at the theoretical work done on silicon nanocrystals.

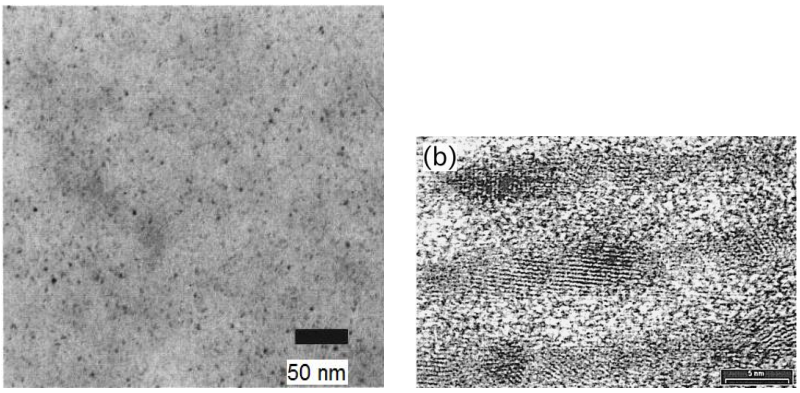

Figure 2.1: TEM images of Si nanocrystals prepared by annealing $SiO_{1.3}$ (left), from [16] and by annealing a multi-layer Si/SiO_2 film (right), from [9].

2.1.1 Production methods

There are several ways of depositing a thin film leading to silicon nanocrystals - briefly spoken there are three approaches commonly used. These are: deposition of a silicon rich silicon dioxide, SiO_x, deposition of a multi-layer film of alternating Si [8,9] or SiO [10] and SiO_2 layers and finally ion implantation of silicon into silicon dioxide [11]. Of these methods we have primarily used the Si/SiO_2 multi-layer approach, as this leads to excellent size control and dispersion. The deposition of these thin films may be carried out in a multitude of ways and has been demonstrated using plasma enhanced chemical vapour deposition [12,13], magnetron sputtering [14] and e-beam deposition. In all cases the film is subsequently annealed in an inert atmosphere, most commonly N_2, although Ar has also been used. It is believed that nitrogen helps reduce surface defects on the Si/SiO_2 interface, whereas Ar is completely inert [15], which is evident from the significantly more intense luminescence from N_2 annealed samples.
The connection between nanocrystal size and silicon excess in the sample is well understood. In the case of SiO_x films, less excess generally leads to smaller nanocrystals whereas a larger excess leads to larger nanocrystals, with mean radii of nanocrystals down to 1 nm reported [13,16]. For multi-layer Si/SiO_2 films the nanocrystal diameter after annealing is on the order of the Si layer thickness, in part due to the limited Si diffusion through the SiO_2 layers [9,17]. Typical TEM images of the two different structures may be seen in fig. 2.1. Regarding annealing, higher temperatures and longer times naturally lead to longer diffusion lengths for the silicon and

thus larger nanocrystals[18]. Temperatures around 700°C are needed to start silicon diffusion, amorphous nanocrystals are observed when annealing up to 900°C, whereas crystallisation of the amorphous nanocrystals take place at 1100°C[17], as evidenced by TEM and Raman spectroscopy[18]. Following the high temperature anneal to promote formation/crystallisation of nanocrystals, an anneal at typically 500°C is carried out in forming gas (95% N_2/5% H_2) in order to passivate dangling bonds at the nanocrystal/oxide interface, which, as will be seen, has a dramatic effect on the photoluminescence yield.

2.1.2 Photoluminescence

The photoluminescence from silicon nanocrystals in SiO_2 has been subject to intense research, however the exact mechanisms at play have not been agreed upon[19]. Most commonly defects at the nanocrystal surface and quantum confinement of the exciton are discussed as possible mechanisms. Early reports of luminescence in the blue-green are now mostly ascribed to defects in the SiO_2. Today, luminescence reports are in the range around 600 nm to 1050 nm, which is in good agreement with the 1.1 eV band gap of bulk silicon corresponding to 1130 nm emission. A typical spectrum from a multi-layer sample containing 20 periods of 2 nm Si/4 nm SiO_2 deposited by magnetron sputtering and then annealed at 1100°C in N_2 with following hydrogen passivation may be seen in Fig. 2.2.

The systems under investigation may vary wildly in production and composition. Depending on size and environment of the nanocrystals, different mechanisms may be at play, which is part of the reason for no universal mechanism being accepted. Given the role played by defects and non radiative pathways, as evidenced by the relatively low quantum efficiency, under 0.1%[20], of silicon nanocrystals, it is an important factor in any case. As mentioned, hydrogen passivation after nanocrystal crystallization has taken place is often applied and leads to an increase in photoluminescence yield by as much as an order of magnitude. In an impressive experiment attempting to measure the spatial distribution of the wave function and backed up by EPR measurements, Godefroo and coworkers proposed that the photoluminescence before passivation is due to interface defect states, whereas it is from a mode confined to the whole nanocrystal after passivation[21].

Time resolved photoluminescence spectroscopy has been used extensively to characterize silicon nanocrystals in SiO_2. A decay characteristic slower than a single exponential form is found, most often the stretched exponential is

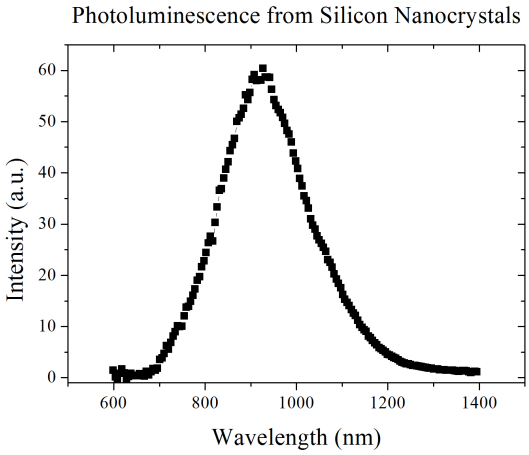

Figure 2.2: Photoluminescence spectrum from a multi-layer sample containing 20 periods of 2 nm Si/4 nm SiO_2, annealed at 1100°C in N_2 for 60 minutes and then hydrogen passivated at 500°C.

used,

$$I(t) = I_0 \exp\left[-\left(\frac{t}{\tau}\right)^{\beta}\right], \tag{2.1}$$

where β is a dispersion factor due to the distribution of nanocrystal sizes and electron transfer processes, depending on nanocrystal size and seperation. The time constant τ will depend on a host of factors, broadly spoken the size and environment of the nanocrystals[22–25]. A large part of the multiexponential nature of silicon nanocrystal may also owe to their pseudo-direct band gap, which facilitates several different decay pathways, both direct and phonon-assisted[26]. By measuring τ at different wave lengths, it is possible to deduce some size-dependence. It is found that decay times are generally shorter for lower wavelengths (smaller nanocrystals), which corresponds to the physical picture of the electron and hole being confined to a smaller volume and thus having a larger recombination rate. However migration of the electron-hole pair from the nanocrystal also plays a significant role, specifically recombination at non-radiative centers leads to a lowering of the decay time. This effect is also seen if observing similar samples with and without hydrogen passivation, the hydrogen passivated samples will tend to have longer lifetimes as non-radiative pathways are eliminated from the system.

2.1.3 Theoretical Modelling

Several theoretical models have been applied towards understanding electronic and optical properties of silicon nanocrystals. The most used candidates for treating nanocrystals up to several nanometers of size are tight-binding[26,27] and effective mass approaches[28], while *ab initio* methods like density functional theory may be used for small clusters[29]. Both silicon clusters passivated by hydrogen as well as silicon clusters embedded in SiO_2 and with simulated oxygen defect sites in the form of Si=O have been modelled. In the latter case it is found that Si=O introduces an almost constant energy electron and hole defect state into the otherwise size-dependent band gap[27], an example of this is shown in Fig. 2.3.

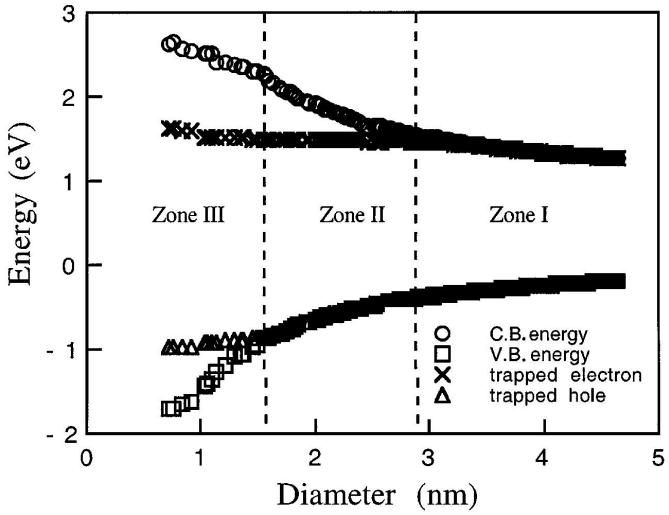

Figure 2.3: Calculated tight binding energy levels in a hydrogen-terminated silicon nanocrystal, with one Si=O bond on its surface. For smaller diameters, the defect state introduced by Si=O has a lower gap than the completely passivated crystal. Reproduced from[27].

2.2 Erbium in Glass

Erbium is a lanthanide with electronic configuration $[Xe]4f^{12}6s^2$. Most often encountered, and of the most interest in optical applications is the trivalent ion, which gives off its $6s$ electrons and one of the $4f$ electrons. The outer electrons are now $5s^25p^6$ which partially shield the $4f$ electrons,

which are responsible for the optical transitions. The splitting and energy levels of the $4f$ electrons due to spin-orbit interaction is shown in Fig. 2.4. It is the transition from the first excited state $^4I_{13/2}$ to the ground state that is responsible for emission around $1.53\mu m$, which is of particular interest. For isolated Er^{3+}, the intra $4f$ transitions are parity forbidden and hence

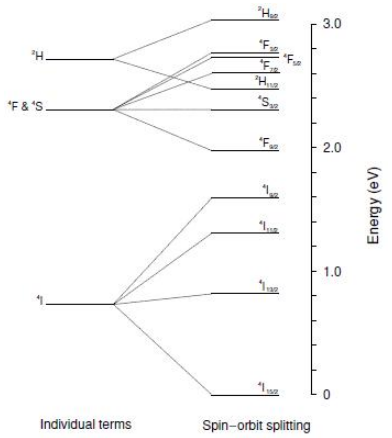

Figure 2.4: Splitting and energy levels in the Er^{3+} ion, due to spin-orbit interaction, from[30].

very slow. In the presence of an external perturbation, for example by sitting in a crystal host, the crystal field leads to mixing of the odd and even parity wave functions making the transitions slightly more dipole-allowed. Even then, the $^4I_{13/2} \rightarrow^4 I_{15/2}$ still exhibits a fairly long lifetime of up to 14 ms in silica[30] and even slower in other glasses[31]. In spite of this, the shielding of the $4f$ electrons by the outer electroncs leads to the transition energies varying only slightly with differing hosts. Spectral broadening owes to temperature dependent phonon effects and temperature independent inhomogenous broadening due to ions at different sites experiencing slightly different energy shifts[32], different crystal hosts may also give different amounts of splitting because of different strengths of the crystal field. Absorption bands are found around 1480 nm, 980 nm, 800 nm and 520 nm and at lower wavelengths, into the top of the $^4I_{13/2}$, $^4I_{11/2}$, $^4I_{9/2}$ and $^4S_{3/2}$ levels respectively. Whereas the $^4I_{13/2} \rightarrow^4 I_{15/2}$ is 100 percent radiative in nature, the higher states are dominated by non radiative multi-phonon assisted decay, leading to only weak luminescence from these[33].

2.3 Erbium sensitized by Si Nanocrystals

As seen, the absorption spectra of erbium in glass is discrete and in addition has a low absorption cross section (on the order of $10^{-21} - 10^{-20}$ cm^2 [30,33]). This means that commercial Erbium Doped Fiber Amplifiers (EDFAs) are usually pumped by rather expensive 980 nm lasers, which in addition are absorbed weakly [34]. A way to improve this is by the addition of silicon nanocrystals to the SiO_2 host, the nanocrystals couple strongly to the erbium ions [35,36]. The effect is two-fold, most significantly, the effective absorption cross section of the erbium ions is increased by several orders of magnitudes, to $10^{-21} - 10^{-20}$ cm^2 and the effective absorption spectrum becomes much broader. By using such an approach, gain at $1.53\mu m$ has been demonstrated in a top-pumped configuration using commercial LEDs and Er-doped silica with nanocrystals as the active medium [37]. Despite this achievement, performance is in many regards still inferior to conventional in-line pumped amplifiers. To achieve efficient gain, achieving population inversion is neccesary, meaning that all erbium ions in the sample should be coupled to nearby sensitizers. As such, careful control and understanding of this interaction is neccesary.

2.3.1 Production Methods

Many of the same methods used for the production of silicon nanocrystals in a silica matrix can also be applied, with erbium added to the SiO_2 source, or by simultaneous deposition of SiO_2 and erbium. Erbium concentrations should be kept below 10^{20} cm^{-3} in order to avoid cluster formation [38]. Annealing is carried out with similar results as in pure nanocrystal films, eg. temperatures around $1100°C$ are needed in order to obtain crystalline nanocrystals, whereas lower temperatures yield amorphous nanocrystallites/sensitizers as would be expected. Often, anneals are followed by hydrogen passivation. What is perhaps more surprising is that low temperature annealed samples may show higher photoluminescence yield and, more significantly, higher fractions of excited erbium [39–45] than high temperature annealed samples, even if determining the optimum Si excess at each anneal temperature [45], see Fig. 2.5 for an example. Thus, the sensitizers need not be crystalline (and thus fairly efficient optical emitters themselves), to effectively transfer energy to erbium ions [46]. Conceptually, the density of sensitizers at low anneal temperatures may be significantly higher than when many Si atoms are used to form large nanocrystals, whereas an amorphous sensitizer may contain much fewer atoms. This is essential to achieve a

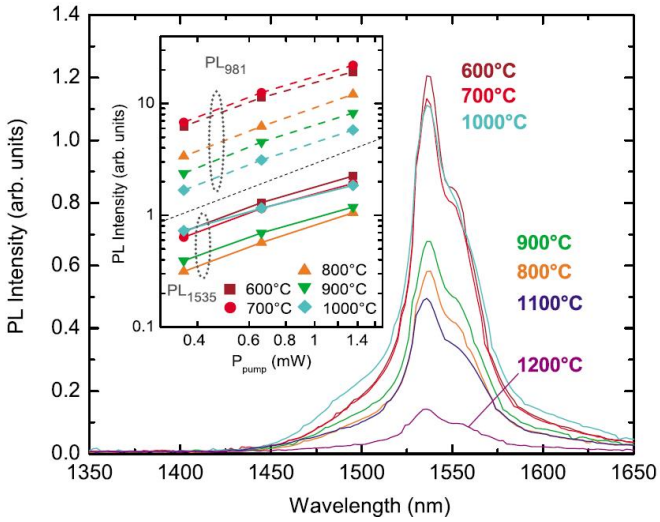

Figure 2.5: Photoluminescence spectrum from Er^{3+} sensitized in Si-rich silica, annealed at varying temperatures from 600-1200°C. Insert shows Er^{3+} signal at 981 and 1535 nm as a function of pump power. From [40].

high fraction of exciteable erbium through sensitizers. If assuming perfect coupling between each sensitizer and erbium, the optimum sensitizer concentration should be equal to the erbium concentration, for a typical erbium concentration of $2 \cdot 10^{19}\ cm^{-3}$, an equivalent sensitizer concentration leaves

2.3.2 Luminescence properties

Luminescence around 1535 nm is always present in succesfully sensitized samples, however transient behavior of the ${}^4I_{13/2} \rightarrow {}^4 I_{15/2}$ transition varies a lot across samples, particularly depending on annealing temperature and conditions, but also on the Si excess. For silica with low Si excess annealed at around 1100°C, lifetimes around 11 ms are reported, close to the lifetime observed for Er^{3+} in pure silica[30]. Generally decreasing temperature and increasing the silicon content decreases the lifetime, due to the stronger pertubation from the less ordered environment[47]. For low temperature annealed samples lifetimes as low as 0.5 ms are observed[40].
Apart from luminescence at 1535 nm, luminescence at 980 nm is also observed in all sensitized samples, corresponding to the ${}^4I_{11/2} \rightarrow {}^4 I_{15/2}$ transition, which leads to the conclusion that sensitization takes place into the ${}^4I_{11/2}$ level[40,48].

2.3.3 Sensitizer Interaction

The rate of transfer from sensitizers in silica to erbium ions has been commented on in several publications. By observing nanocrystal and erbium emission at temperatures from 20 K to 300 K, it is seen that while nanocrystal photoluminescence is strongly affected, becoming both more intense and much slower in accordance with[23], erbium emission is unaffected by temperature. This is only possible if the nanocrystal-erbium coupling is strong and much faster than the decay rate at room temperature. If we adopt a picture where some nanocrystals are coupled to erbium ions and the rest are not close enough with an erbium ion to interact with it and thus act like silicon nanocrystals would in a pure silica matrix[49]. The coupling, however, is not so strong as to make back transfer a problem, like it is in Er doped Si[50]. Studying the nanocrystal-erbium system using ns laser pulses reveals a similar picture, the interaction is faster than what may be resolved[22,48,51], a similar result is found for low temperature annealed sensitizers[42].
In order to further investigate the interaction between sensitizer and erbium, several experiments have been made attempting to determine the interaction distance. Briefly spoken, the interaction may either be short Dexter-like and require some degree of wave function overlap between the erbium $4f$ orbitals and the sensitizer's orbital[52]. It may perhaps be some longer range Förster dipole-dipole interaction[53]. While it may be simple to envision an experiment where one would construct a multilayer Si/SiO_2:Er/SiO_2 film, changing the thickness of the SiO_2:Er layer while keeping total SiO_2 layer thickness constant to see how the distance from erbium to sensitizer influences the total photoluminescence yield such a film is not easily made. First off, if the interaction distance is indeed short, it is neccesary to deposit homogenous films with subnanometer precision over several layers. While this challenge can be overcome, the diffusion of erbium is a much more serious challenge to overcome, erbium will diffuse several nm into the undoped silica if annealing to temperatures high enough to form crystalline nanocrystals[54]. Thus, succesful experiments are limited to low temperature annealed samples, in which the sensitizers are amorphous nanocrystals. In such cases, the interaction distance has been found to be very short, around 0.5 nm[55], or even in direct contact with the nanocrystals[56]. Followingly, the interaction is believed to be dominated by wave function overlap between sensitizer and the erbium $4f$ orbitals.

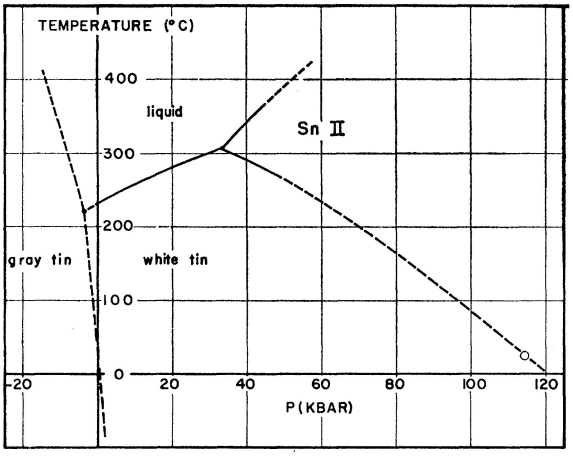

Figure 2.6: Phase diagram for Sn. Gray tin is the diamond structured, zero gap α-phase, whereas white tin is the metallic phase. Sn II is a high pressure Sn^{2+} phase, reproduced from ref.[58].

2.3.4 Theoretical Modelling

The amount of theoretical work on the nanocrystal-Er^{3+} is fairly limited due to the complexity of the system and the uncertainties regarding the transfer mechanism. A model was proposed in ref.[48,57]. The silicon nanocrystal wave functions are found using an effective mass approach as in[28] and their probability of exciting a nearby Er^{3+}-ion into the $^4I_{13/2}$ state via an intraband Auger proces as a result of hot carrier transitions is considered. Also excitation into higher-lying states by electron-hole recombination is considered. It is suggested that the first mechanism is responsible for initial, fast decay of Er^{3+} in the Si-NC:Er system and the second for the slower decay. In addition it is found that the electron-hole recombination mechanism is effectively a "contact" transfer mechanism and that dipole-dipole interaction (Förster transfer) is non-efficient.

2.4 α-Tin

α-Sn, or grey tin, is the preferred state for Sn below $13.2°C$, where it takes on diamond structure. At higher temperatures it is metallic in its body-centered tetragonal β-form[58], white-tin, see the phase diagram in fig. 2.6. Unlike the higher lying group IV semiconductors, α-Sn is a direct, zero-gap semiconductor, or a semimetal, as seen from the band structure in fig. 2.7.

That is, the band gap is 0 eV, but the density of states at the Fermi level is 0, thus α-Sn is usually not considered in conventional semiconductor applications. Where α-Sn shows promise is when nanocrystals are formed from

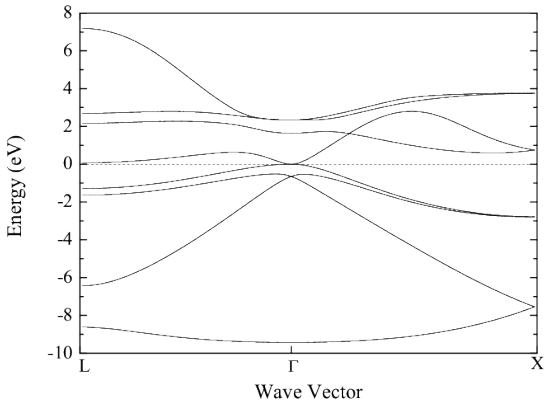

Figure 2.7: Band structure of α-Sn, calculated with tight binding parameters that reproduce the DFT-GW bandstructure including spin-orbit interaction, given in[59]. The dashed line at 0 eV indicates the Fermi level.

it. Thanks to the zero-gap nature of the bulk material, it is possible to tailor the band gap of the nanocrystals to even NIR applications[60–62] through their size. Such low band-gap nanocrystals are not realisable in Si or Ge due to the intriscally higher band gap of the bulk material. As is evident from the phase diagram in fig. 2.6, it is neccesary to strain stabilize α-Sn to prevent it from turning into β-Sn at room temperature. As it turns out, α-Sn nanocrystals may be strain-stabilized by embedding them in a suitable host, for instance Ge or Si[63–67]. The lattice mismatch between Si and α-Sn however is fairly large at 19.5% and as such it remains a challenge to grow α-Sn nanocrystals. An example of the absorption spectrum of α-Sn nanocrystals is seen in fig. 2.8. The crystals are grown on a Si(001) substrate by molecular beam epitaxial deposition of α-$Sn_{0.10}Si_{0.90}$ at $170°C$ and subsequent annealing at 800°C in vacuum where crystallisation takes place, as is confirmed be TEM in the study[67]. In this spectrum it is evident that there is absorption far into the infrared, highlighting the potential that α-Sn nanocrystals have in a spectral range that is not easily accesible.

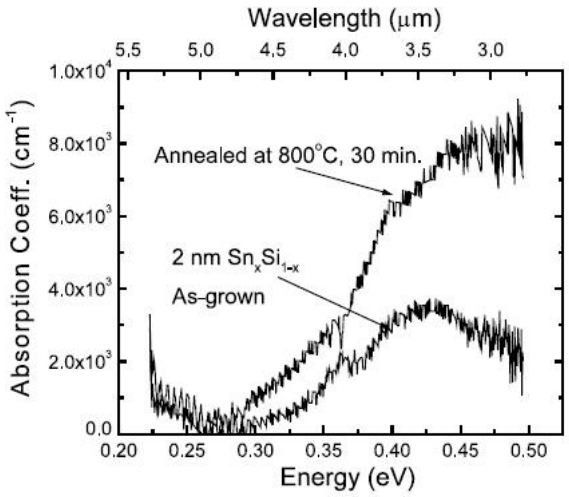

Figure 2.8: Fourier transform infrared spectroscopy measurement of the absorption coefficient for a thin film of $Sn_{0.10}Si_{0.90}$ annealed at 800°C, leading to the formation of nanocrystals. From ref.[67].

Chapter 3

Theoretical methods

There are a host of different methods available for calculating electronic structure in periodic solids, ranging from *ab initio* methods such as density functional theory (DFT) to empirical methods such as empirical pseudopotentials. Furthermore, in spite of the large number of electrons present in almost all systems, most methods solve single-electron Schrödinger equations for the outermost electrons in each atom, with a potential applied, meant to emulate the other electrons, the nuclei and their interaction. In all cases the initial goal is to accurately predict the electronic structure for relatively small unit cells with periodicity in three dimensions, eg. a bulk material. In the case of nanocrystals, this periodicity is not present and the unit cell may contain thousands of atoms, in order to describe nanocrystal a few nanometers large. This is also what gives rise to many of the interesting properties of nanocrystals as the breakdown of the periodicity means the band nature of solids is no longer an adequate description of nanocrystals, which instead undertake a more molecular-like behaviour. Under these circumstances, atomistic descriptions of the nanocrystal with the aim to solve the full Schrödinger equation, with each atom being described in terms of a local potential becomes increasingly demanding and for sufficiently large nanocrystals becomes computationally unfeasible. In this case the problem may be solved in terms of a less demanding description of each atom, as is done for instance in tight binding, where each atom is decribed by a number of localized orbitals, which strongly reduces the overall size of the basis needed for expanding the solution. Another possibility is to employ an effective mass model, where the nanocrystal is considered a three dimensional spherical potential well, with a potential jump on the edge corresponding to the work function difference between nanocrystal and host material.

3.1 Tight Binding

In the following a brief description of tight binding will be given and how it is applied to both bulk solids as well as nanocrystals. Furthermore it will be discussed how to calculate the optical response on the background of the tight binding wave functions.

The central idea of tight binding is to expand the one electron wave function in a linear combination of localized, atomic orbitals, centered at $\vec{R}$, $|\alpha, \vec{R})$, with α denoting the kind of orbital and in case of multiple atoms per unit cell also which atom it belongs to. For periodic solids the expansion in orbitals is usually combined with Bloch's theorem, eg. that if the wave function is expanded in plane waves, it can be be easily rewritten on the form[68]

$$\psi(\vec{r}, \vec{k}) = e^{i\vec{k}\cdot\vec{r}} u(\vec{r}, \vec{k}), \tag{3.1}$$

where $u(\vec{r}, \vec{k})$ is a function with the same periodicity as the crystal lattice. Thus for an arbitrary translation vector of the crystal lattice $\vec{T}$, it follows that $u(\vec{r} + \vec{T}, \vec{k}) = u(\vec{r}, \vec{k})$. Thus we construct our tight binding bloch functions

$$|\alpha, \vec{k}\rangle = \frac{1}{\sqrt{N}} \sum_{\vec{R}} e^{i\vec{k}\cdot\vec{R}} |\alpha, \vec{R}) \tag{3.2}$$

where N is the number of unit cells in the crystal and the summation should run over all lattice vectors $\vec{R}$ in the crystal. We now expand the n'th crystal wave function in terms of the Bloch tight binding orbitals in eq. 3.2

$$|n, \vec{k}\rangle = \sum_{\alpha} c_{n,\alpha} |\alpha, \vec{k}\rangle. \tag{3.3}$$

Inserting this into the Schrödinger equation and minimizing the the energy leads to the secular equation

$$(\overleftrightarrow{H} - E(\vec{k})\overleftrightarrow{S})\vec{c} = 0, \tag{3.4}$$

with

$$H_{m,m'} = \frac{1}{N} \sum_{\vec{R},\vec{R}'} e^{i\vec{k}\cdot(\vec{R}-\vec{R}')} (m', \vec{R}'|\hat{H}|m, \vec{R}), \tag{3.5}$$

$$S_{m,m'} = \frac{1}{N} \sum_{\vec{R},\vec{R}'} e^{i\vec{k}\cdot(\vec{R}-\vec{R}')} (m', \vec{R}'|m, \vec{R}), \tag{3.6}$$

with m being an index running over each orbital, on each site in the crystal. In a periodic crystal with N lattice sites, the summation on each site will give the same result, allowing us to simplify the summation to only one site,

$$H_{m,m'} = \sum_{\vec{R}} e^{i\vec{k}\cdot(\vec{R}-\vec{R_0})}(m', \vec{R_0}|\hat{H}|m, \vec{R}), \tag{3.7}$$

$$S_{m,m'} = \sum_{\vec{R}} e^{i\vec{k}\cdot(\vec{R}-\vec{R_0})}(m', \vec{R_0}|m, \vec{R}). \tag{3.8}$$

In practice, due to the localized nature of the atomic orbitals, it is assumed that the contributions from orbitals some cut-off distance away is negligible. In the calculations in this work, orbitals belonging up to the third nearest neighbour are considered. In principle, the matrix elements are multi-centered in nature, that is they should depend on the presence of all other atoms in the lattice. However, as first discovered by Slater and Koster [69], using a two-center form and exploiting symmetries of the atomic orbitals, simple expressions for the matrix elements may be derived in terms of $(\vec{R} - \vec{R_0})$ and a number of constants that may be either calculated (semi-)empirically or fitted to reproduce a given band structure. Taking for example bulk silicon, the experimental band structure may be accurately reproduced by the help of a $3s, 3p_x, 3p_y, 3p_z$ basis. As silicon has two distinct atoms in its unit cell, this corresponds to an expansion in 8 basis functions and thus a 8x8 eigenvalue problem, with each matrix element being easily calculable. Computationally the evaluation of such a problem is extremely quick, allowing evaluation for many seperate $\vec{k}$-points very rapidly. As an example, the band structure of silicon has been calculated, using the parameters from [70], shown in fig. 3.1. Inclusion of spin-orbit interaction (SOI) turns out to be fairly simple in tight binding and is a relevant correction particularly for heavier elements. Using instead spin polarized tight binding orbitals, introduces a number of simple coupling terms between p orbitals of different orientation in the Hamilton matrix, however this means that the matrix problem doubles in size.

For a nanocrystal, the periodicity of the solid breaks down and in effect only $\vec{k} = \vec{0}$ makes sense, which cancels out the phase factor. On the other hand, the basis size increases tremendously, as the unit cell also increases in size. As we are no longer considering a solid with periodic boundary conditions, the surface also needs to be treated, in order to avoid dangling bonds. The most simple way of doing this is by saturating each dangling bond by a single hydrogen atom, in practice this means that a silicon atom which has only 3 nearest neighbours in the nanocrystal would get an additional

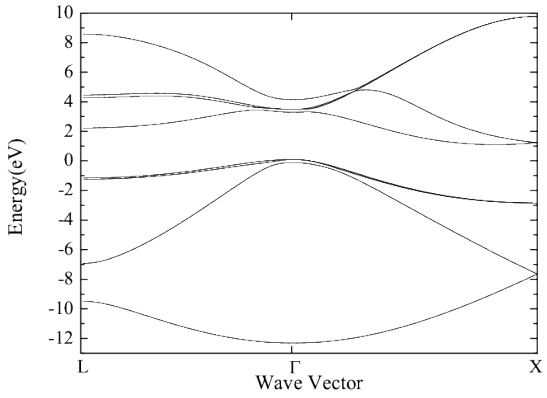

Figure 3.1: The band structure of silicon calculated from the tight binding parameters in [70], and including spin orbit coupling $\Delta = 0.044$eV.

hydrogen atom placed at the position of the fourth, missing atom.

3.1.1 Optical response

The aim of this section is to describe how to obtain the electric susceptibility from the tight binding wave functions. First and foremost, a general expression for the linear optical susceptibility for a semiconductor may be obtained by the means of first order pertubation theory [71],

$$\chi(\omega) = \frac{2e^2\hbar^2}{\epsilon_0 m_e^2 \Omega} \sum_{m\in c} \sum_{n\in v} \frac{|\langle m|\hat{p_z}|n\rangle|^2}{E_{mn}\left\{E_{mn}^2 - \hbar^2(\omega + i\Gamma)^2\right\}} \tag{3.9}$$

this taken in the limit of zero temperature. This ensures full occupation of the valence bands, v and no occupation of the conduction bands, c, which also ensures that there is no intra-band contribution to the susceptibility or indirect transitions. The summation $m \in c$ runs over all conduction band states and similarly for the valence bands and $n \in v$. The remaining challenge is to calculate the so called momentum matrix elements $\langle m|\hat{p_z}|n\rangle$. Centrally, the idea is to exploit the commutator relation $\hat{\vec{p}} = \frac{im_0}{\hbar}\left[\hat{H}, \vec{r}\right]$ to rewrite the matrix elements. Assuming that the overlap between neighbouring cells is vanishing, it follows that $(m, \vec{R'}|\vec{r}|n, \vec{R}) = (\vec{R}\delta_{nm} + \vec{d}_{nm})\delta_{\vec{R}\vec{R'}}$, where the two terms may be interpreted as inter and intra-atomic terms

respectively. Putting the tight binding eigen functions in eq. 3.3 into the momentum matrix element this may be reduced to [72],

$$\begin{aligned}\langle n,\vec{k}|\vec{p}|m,\vec{k}\rangle &= \frac{m_0}{\hbar}\sum_{\alpha,\beta} c_{n\beta}(\vec{k})^* c_{m\alpha}(\vec{k})\nabla_{\vec{k}}\langle\beta,\vec{k}|H|\alpha,\vec{k}\rangle \\ &+ \frac{im_0}{\hbar}\left(E_{n,\vec{k}} - E_{m,\vec{k}}\right)\sum_{\alpha,\beta} c_{n\beta}(\vec{k})^* c_{m\alpha}(\vec{k})\vec{d}_{\alpha\beta}. \quad (3.10)\end{aligned}$$

While the first inter-atomic term is fully determined from the band structure, the second intra-atomic term, which is occasionally omitted, has the quantity $\vec{d}_{\alpha\beta}$, which must be fitted, as we do not know the explicit form of the tight binding basis functions. As the derivative in p_z changes the parity in the z-direction, for an orbital pair to contribute, one of the orbitals should be odd in the z-direction. Thus, when evaluating p_z in a basis set containing only s and p orbitals, the only orbital pair contributing to the term is s and p_z. This also means that there is only one $\vec{d}_{\alpha\beta}$ to fit, which may be done to best reproduce the experimental absorption spectrum, before extending the calculation to predict optical properties of eg. nanocrystals. As an example, the absorption spectrum for Si has been calculated, including both the inter- and intra-atomic terms and including the contribution from each, seen in fig. 3.2, with the value $d_{s,p_x} = 5.2$ eVÅ. In practice, the integration over the first Brillouin zone may be greatly simplified by only integrating over the irreducible Brillouin zone and further by dividing this into several tetrahedra and applying an interpolation scheme, like in [73,74]. As may be seen from fig. 3.2 the predicted absorption properties when using the full expression yields a satisfying result, in the sense that the low energy structure and approximate magnitude is in agreement with experiment.

3.2 Density Functional Theory

The central theorem of DFT is that the properties of a many-body electronic system depend only on the ground state electronic density $n(\vec{r})$ through some arbitrary functional, as discovered by Hohenberg and Kohn [76]. While the proof of this is quite simple and elegant it does not tell us which functional we should put the electron density into, to obtain for instance the total energy of the system, or how to solve the equations. As such much of the effort spent on DFT is on developing suitable functionals and developing algorithms for solving the equations. We start by considering the hamiltonian for a system

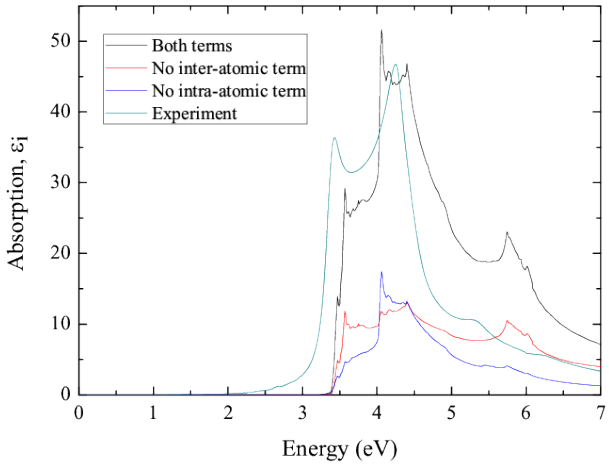

Figure 3.2: Absorption spectrum of silicon calculated from the tight binding band structure. The light blue line is the experimental result from[75], the black, red and blue lines are experimental calculations including both, only intra- and only inter-atomic terms, respectively.

of many electrons and fixed nuclei in some external potential

$$\hat{H} = -\frac{1}{2}\sum_i \nabla_i^2 + \frac{1}{2}\sum_{i\neq j}\frac{1}{|\vec{r}_i - \vec{r}_j|} + \sum_i V_{ext}(\vec{r}_i), \tag{3.11}$$

where the Coulomb electron-electron interaction is included in the second term and the electron-nuclei interaction is contained in the external potential V_{ext}. What the Hohenberg-Kohn theorem states is that the external potential is uniquely determined within a constant by the ground state electron density

$$n_0(\vec{r}) = |\psi_0(\vec{r_1}, \vec{r_2}, ...\vec{r_n})|^2. \tag{3.12}$$

Conversely, if we know the full form of V_{ext} this allows us to determine the full hamiltonian of our system and thus determine all excited states as well, hence all properties of the system. The second part of the theorem states that a functional for the total energy of the system may be stated in terms of the electron density, given by

$$E_{HK}[n] = T[n] + E_{int}[n] + E_{II} + \int V_{ext}(\vec{r})n(\vec{r})\mathrm{d}^3r \tag{3.13}$$

with $T[n]$ being the kinetic energy functional, $E_{int}[n]$ is the electron-electron interaction, E_{II} is the nuclei interaction energy, and the last term is the interaction of the density with the external potential. The ground state energy then becomes a matter of identifying the electron density $n_0(\vec{r})$ that minimizes this functional. It is important to note that this theorem only gives us the ground state energy, it tells us nothing about the excited states. Furthermore, this functional is rather elusive, we do not know its explicit form. The next step towards practical implementation of DFT is that made by Kohn and Sham[77]. The central ansatz is that the ground state density of the interacting many electron system is equal to that of some chosen non-interacting system. This allows us to consider the system in terms of a number of independent particles, in a local, effective potential. In practice, the calculations are carried out on this auxiliary, independent system through the auxiliary hamiltonian

$$\hat{H}_{aux} = -\frac{1}{2}\nabla^2 + V_{eff}(\vec{r}). \tag{3.14}$$

Insofar, the form of this effective potential is unknown. For a system of N electrons obeying this hamiltonian, the system has one electron in each of the first N states and as such the ground state density is given by

$$n(\vec{r}) = \sum_i^N |\psi_i(\vec{r})|^2. \tag{3.15}$$

In a similar fashion the total kinetic energy of the independent particle ensemble is given by

$$T_{KS} = -\frac{1}{2}\sum_i^N \langle\psi_i|\nabla^2|\psi_i\rangle, \tag{3.16}$$

the Coulomb interaction of the electron density with itself is given by

$$E_H[n] = \frac{1}{2}\int \frac{n(\vec{r})n(\vec{r'})}{|\vec{r}-\vec{r'}|}\mathrm{d}^3r\mathrm{d}^3r'. \tag{3.17}$$

Finally, this allows us to evaluate the total energy in this picture,

$$E_{KS} = T_{KS} + \int V_{ext}(\vec{r})n(\vec{r})\mathrm{d}^3r + E_H + E_{XC}[n], \tag{3.18}$$

where again, V_{ext} is the external potential due to nuclei and external fields and we have introduced the exchange and correlation functional $E_{XC}[n]$,

which includes all many-body effects. Comparing eq. 3.18 with eq. 3.13 allows us to determine the form of the exchange-correlation functional

$$E_{XC}[n] = T[n] - T_{KS} + E_{int}[n] - E_H[n]. \tag{3.19}$$

Thus the exchange-correlation functional's aim is to compensate the difference in kinetic and interaction energy between the real many-electron system and the independent electron system. Obviously, the explicit form of the exchange-correlation energy functional is exceedingly complex, however it may be very well approximated.
Finally by taking the functional derivative of eq. 3.18 with respect to the density, we may arrive at the much celebrated Kohn-Sham equations:

$$H_{KS} = -\frac{1}{2}\nabla^2 + V_{ext}(\vec{r}) + V_H(\vec{r}) + V_{xc}(\vec{r}), \tag{3.20}$$

and the secular equation

$$(H_{KS} - \epsilon_i)\psi_i(\vec{r}) = 0, \tag{3.21}$$

where ϵ_i are the Kohn-Sham eigenvalues. This gives an equation for each electron that must be solved and this solution gives rise to the electron density, which in turn determines the external potential V_{ext} which each electron equation has to be solved self consistently for.
The simplest approximation to the exchange-correlation (XC) functional is that achieved by considering an uniform electron gas, from which an analytical solution can be achieved in terms of the local density, hence the name Local Density Approximation (LDA). More complicated functionals exist that also depend on the local density gradient, however the LDA turns out to be an excellent approximation in many cases.
In practice, solving the Kohn-Sham equations for all electrons in a system of many atoms is computationally unfeasible, when the properties of interest are determined only by the outermost electrons in each atom. Instead, each atom and its core electrons are represented by a pseudopotential, which replicates the correct behaviour of the outer electrons in the atom, outside some cut-off radius. In turn, this reduces the number of electrons that need to be solved for dramatically.

3.3 Beyond DFT

As mentioned, DFT only promises to accurately determine the ground state energy, however it makes no assertions of the excited states in the system. As

it turns out, the addition of an electron to an isolator causes a discontinuity in the exchange-correlation potential, which may be described in terms of the energy dependent electron self-interaction and thus not in terms of the density[78,79]. This is the predominant reason for the underestimation that DFT with various functionals makes to the band gap in semiconductors. While the band gap predicted by exact DFT (eg. where the XC potential is fully determined) may be found accurately with the help of a suitable XC functional, this band gap will also be too small and additional self energy terms are needed in order to obtain correct conduction band states[80]. However, knowing at least the first excited states is important in order to asssess several physical quantities, in all kinds of materials.
A particularly succesful framework for the determintion of the excited states is the GW approximation. Due to Coulombic repulsion each electron is surrounded by a positive screening potential, forming a quasi-particle. Mathematically this quasi-particle is described by the single particle Green's function G, which requires the complete self energy $\sum$, that includes and describes all exchange and correlation effects. Due to the complex nature of the self energy in extended systems, only an approximate to it may be obtained. In the GW approximation (GWA) the the self energy is expanded in the screened interaction W and single particle Green's functions G, thus

$$\sum \approx GW, \tag{3.22}$$

which gives name to the approximation. While this theory was proposed already in 1965 by Hedin[81], computational and practical constraints has kept it from being used until the eighties[82,83]. As we shall see, when applied to most semiconductors, the resulting band structures closely reproduce experimental values. An example of this is silicon, which as always has attracted much attention due to its dominant industrial role. The band structure of Si with and without the GW corrected energies is shown in fig. 3.3, taken from[84]. The found band gap of 1.25 eV is in very good agreement with the experimental value of 1.17 eV and similarly the direct gap is found to be 3.36 eV compared to the experimental value of 3.40 eV. As is also seen, the correction to the valence band states is marginal, the LDA approximation is indeed a very good one for the valence bands. The conduction bands, however, are shifted by an almost constant value across the band structure. This nearly equal shifting of the conduction band states is often found in GW calculations.

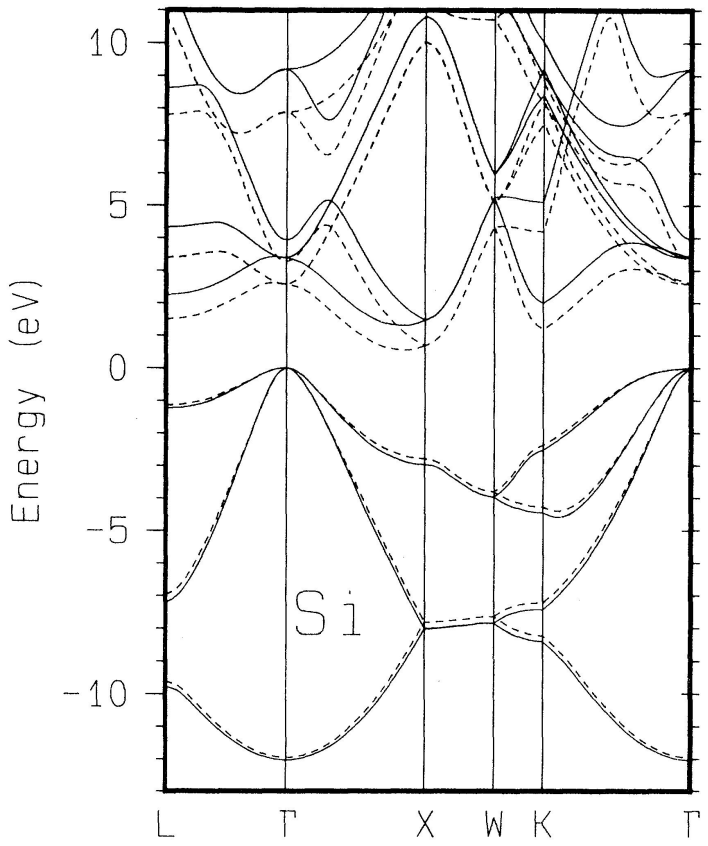

Figure 3.3: Calculated band structure of silicon on the basis of DFT. The dashed lines represent the LDA band structure, whereas the solid lines represent the LDA+GW calculation. From[84].

Chapter 4

Theoretical Modelling

4.1 α-Sn

In comparison to the the higher-lying group IV elements, the theoretical work on α-Sn is very limited. In particular, the modelling of α-Sn nanocrystals is limited to small nanocrystals[85–87] for all but an effective mass, $\vec{k} \cdot \vec{p}$ method[88]. An accurate method for determining electronic and optical properties of nanostructures is tight binding, which also allows for surface effects to be included. However, prior to this, sufficiently accurate tight binding parameters did not exist[85,89–91].

4.1.1 Bulk modelling

The electronic structure of α-Sn may be modelled very accurately within the LDA+GW framework, however using the DFT package *abinit* the inclusion of spin-orbit interaction (SOI) in the GW calculation is not possible. A way around this, that has the added benefit of saving computational power, is to calculate the GW-shifts seperately and apply them to an LDA band structure, with SOI included. This was done in ref.[59]. Then, tight binding parameters were fitted to the GW-corrected band structures, at various degrees of strain, resulting in 3 sets of parameters for $-5\%, 0\%$ and 5% uniform, tensile strain. The varying degrees of tensile strain allows for the calculation of nanocrystals under strain, as they need to be strain-stabilized in their matrix, as discussed in sec. 2.4. The band structure as well as the TB fit may be seen in fig. 4.1. An excellent way to check the accuracy of the band structure is to calculate the dielectric constant and compare it to the experimental findings. While this may be done on the basis of the GW band structure, in a highly accurate framework (see for instance ref.[92]), however

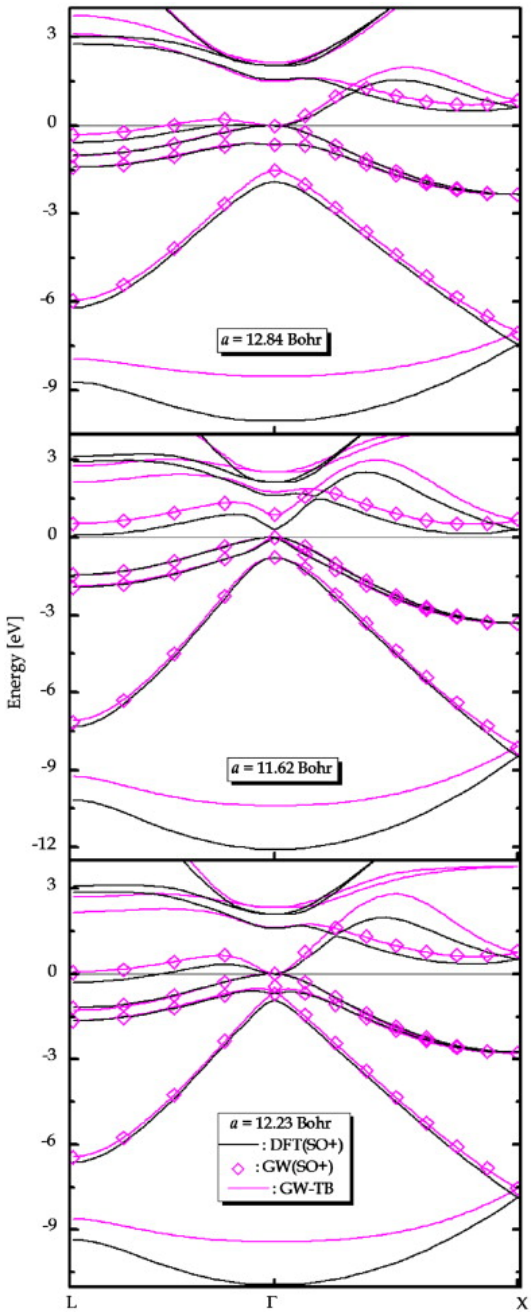

Figure 4.1: DFT band structure of α-Sn under varying degrees of strain. Black lines are energies from the DFT band structure (including SOI), magenta squares are the GW corrected values and the magenta lines are from the TB-fit to the GW band structure, from ref. [59].

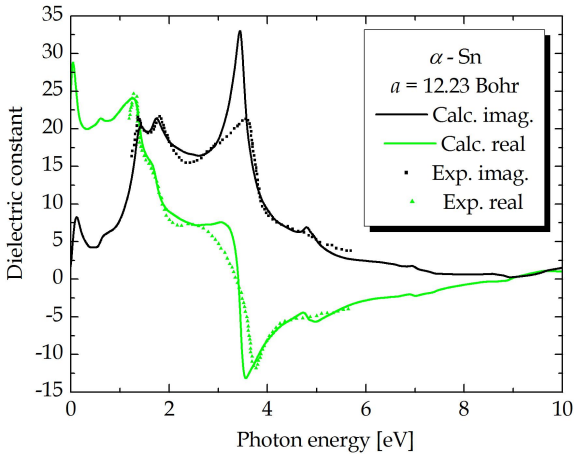

Figure 4.2: Real and imaginary dielectric constant, calculated for α-Sn based on the TB band structure (solid lines), dotted line is the experimental value. From ref.[59].

such an approach is quite complicated and very computationally taxing. A much simpler, computationally fast approach is to use the TB band structure and the method outlined in sec. 3.1.1. This has the added advantage of also testing whether the TB fit is good, outside the fitted interval, as a poor fit outside the fitted interval would result in a poorly corresponding dielectric constant, as this is obtained by integrating over the full Brillouin zone. The calculated and experimental values for the dielectric constant may be seen in fig. 4.2, with the value 3.2 eVÅfound for the momentum matrix element, fitted to minimize the deviation from the experimental result. As may be seen the agreement with experiment is very good and the features corresponding to the first transitions in the band structure is apparent in the ímaginary dielectric constant as well. Also the splitting of the peak around 1.8 eV is due to SOI, this highlights the importance of including SOI in the calculation, in order to produce the experimental results truthfully. We now have a reliable set of TB parameters and may proceed to apply those to nanocrystals.

4.1.2 α-Sn nanocrystals

We calculated the properties of both faceted and round nanocrystals, to investigate if there are any structural effects and as faceted α-Sn nanocrystals have been observed experimentally[64]. The faceted nanocrystal are con-

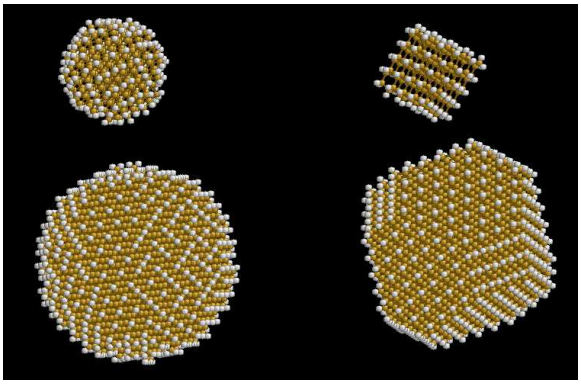

Figure 4.3: Illustration of α-Sn nanocrystals. The left are round crystals whereas the right are faceted. The golden atoms are Sn atoms, whereas the white surface atoms are H.

structed as octaeders, truncated by (111) facets, as in[64], see fig. 4.3 for an illustration. As the surface atoms have dangling bonds, these are saturated with hydrogen atoms, in order to supress surface states. The hydrogen atoms are treated like single s orbitals with $H_{ss\sigma} = -4$ eV and $H_{sp\sigma} = 4$ eV, considering only nearest neighbour interaction, for α-Sn we apply the TB parameters from ref.[59]. Nanocrystals ranging from SnH_4 and up to $Sn_{2317}H_{756}$ for round and $Sn_{2293}H_{756}$ for faceted crystals were constructed. This corresponds to a nanocrystal radii of up to 2.65 nm, which covers the observed experimental species reasonably[63,64,66]. The effective radii of the faceted crystals were calculated by considering a round nanocrystals with an equivalent number of Sn atoms. Also, as observed species are strain stabilized, we consider nanocrystals under -5% and 5% tensile strain as well. The energy gaps found for various sized nanocrystals may be seen in fig. 4.4. As expected, for unstrained nanocrystals the band gap tends to zero, as in bulk, as the radius becomes large. Interestingly, the nanocrystals cover an energy range around 0.1-1 eV, a range not normally available to small nanocrystals, as the bulk band gap energy of most materials prevent this. Given good optical properties, this may make them interesting candidates in NIR applications. Furthermore we see that strain plays a quite large role, with up to 0.5 eV separation between unstrained and strained crystals, as such strain engineering is expected to be relevant in applications. The differences between faceted and round crystals is found to be neglible, expectedly they would play a bigger role if surface effects were treated in a more accurate manner.

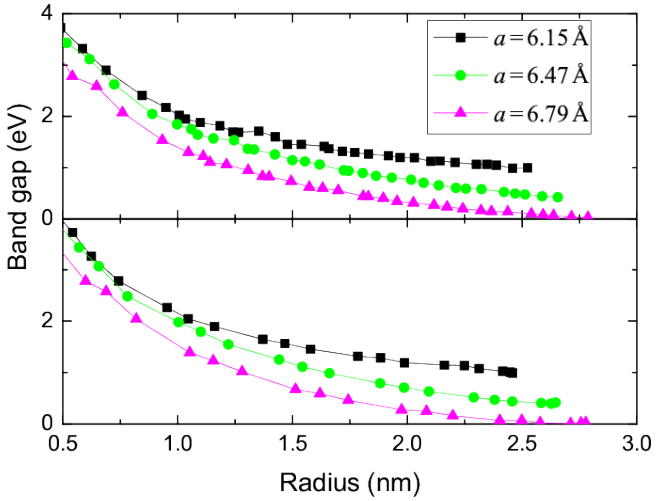

Figure 4.4: Band gap versus radius for α-Sn nanocrystals in both strained and unstrained geometries. Top panel is for spherical nanocrystals, bottom panel is for faceted nanocrystals.

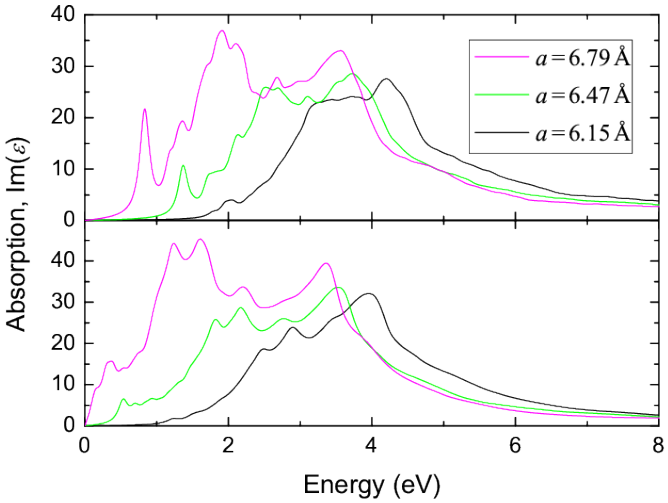

Figure 4.5: Imaginary dielectric constant for round α-Sn nanocrystals in strained and unstrained (a=6.47 Å) configurations. Top panel is for $Sn_{275}H_{172}$ and bottom panel is for $Sn_{1863}H_{605}$.

The imaginary part of the dielectric constant was then calculated for various sized nanocrystals, see fig. 4.5. As is seen, there is an immediate onset of absorption at an energy corresponding to the band gap energy. The direct onset of absorption is believed to be due to the direct gap nature of α-Sn and is particularly promising for applications in optical absorbers, for instance NIR detectors. Particularly for large nanocrystals (bottom panel in fig. 4.5) the absorption spectrum becomes increasingly bulk-like (see fig. 4.2), as expected. While it may be tempting to conclude that tensile strained nanocrystals absorb more strongly, much of this owes to the $1/E$ dependence of the dielectric constant. Calculating the oscillator strength, it may be seen that it is around 10% stronger for tensile strained nanocrystals.
Finally, as excitonic effects are not included in the calculation of the optical properties, we attempt to assess the size of such effects. The scale of the exciton binding energy is given by the effective Rydberg, $Ry^* = 13.6\text{eV}\cdot\mu/\epsilon(0)^2$, with μ the reduced, effective electron-hole mass and $\epsilon(0)$ is the static dielectric constant. Based on experimental values we may find $\mu = 0.024m_0$. The static dielectric constant may be obtained by Kramers-Kronig transformation of the imaginary dielectric constant to obtain the real part, for bulk,

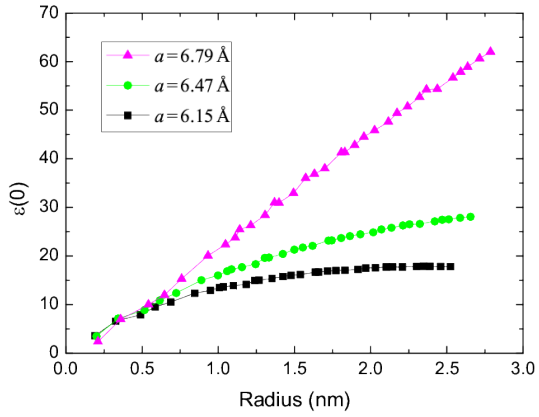

Figure 4.6: Calculated static dielectric constant $\epsilon(0)$ for α-Sn nanocrystals of varying radii and in both unstrained (a=6.47Å) and strained configurations.

unstrained α-Sn we find $\epsilon(0) = 25$. This corresponds to an effective Rydberg of 0.58 meV. In nanocrystals, the static dielectric constant is reduced, see fig. 4.6. This yields somewhat larger effective Rydbergs, particularly for compressed α-Sn, which has semiconductor-like character in bulk. In any case values no greater than 2.3 meV are found for tensile strained nanocrystals. Tensile strained nanocrystals show much stronger screening as bulk, tensile strained α-Sn has more metal-like character. In any case, these numbers are upper bounds, as intraband screening will contribute further to the dielectric screening, at finite temperature. Also, as we see, excitonic binding appears to be very weak and as such we do not expect α-Sn nanocrystals to be affected greatly by exciton effects.

4.2 The SiSn System

In order to further investigate the properties of Sn-Si systems, we study the SiSn alloy. We aim to determine the electronic and optical properties of this system, as previously we will determine the properties under uniform, tensile strain to account for real world conditions. Also, the optical properties are determined by using a TB parameterization to extrapolate the electronic structure to the whole Brillouin zone. The TB parameters may also be useful for studying α-Sn nanocrystals in a Si matrix, in order to account for the Si-Sn bonds on the interface in such a system.

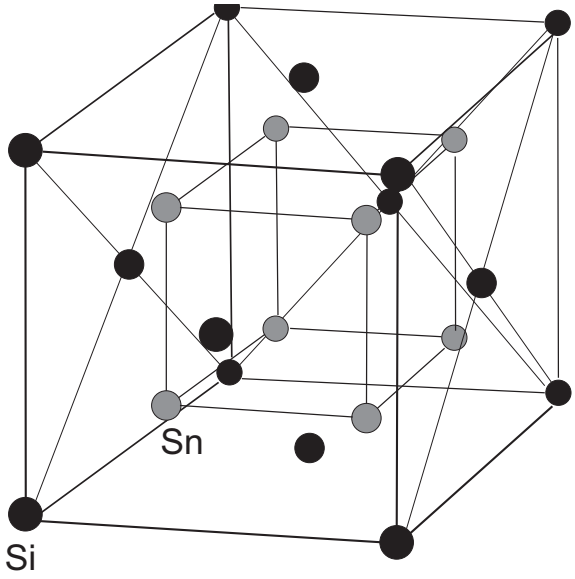

Figure 4.7: The crystal structure used for $SiSn_2$. Black atoms are Si, grey atoms are Sn.

We start off as for α-Sn by calculating the band structure under -5%, 0% and 5% uniform, tensile strain. A two-atom SiSn unit cell with zinc-blende symmetry was constructed and relaxed. In order to assess stability, the total energy per unit cell for the relaxed unit cell is compared with Si and Sn, calculated using a similar approach and pseudopotentials. Furthermore, we relax the $SiSn_2$ structure formed by the 3-atom unit cell with Si at $(0, 0, 0)$ and Sn at $\pm(\frac{1}{4}, \frac{1}{4}, \frac{1}{4})$ in a fcc lattice, see fig. 4.7. This is done to investigate whether a compound like this could be thought to form in SiSn alloys and in that case, which properties it would have. In table 4.1 we have summarized the results and the cost of formation for the compounds. Starting with the lattice constants found for Si and α-Sn, we see that they are slightly smaller than the experimental values, 5.40Åversus 5.43Åfor Si and 6.41Åversus 6.49Åfor α-Sn. This underestimation of the binding is normal for LDA and in good agreement with other theoretical results in similar frameworks[93–98]. For SiSn we observe a lattice constant inbetween that found for Si and α-Sn which is as expected, as is the observation from the cost of formation, that it is a metastable phase. Notably, we also see that the silicide, $SiSn_2$ may form more favorably than SiSn, while clearly still instable it may be stabilized under suitable conditions. We have not found any mentions of $SiSn_2$ in the litterature which may be a sign that the strain

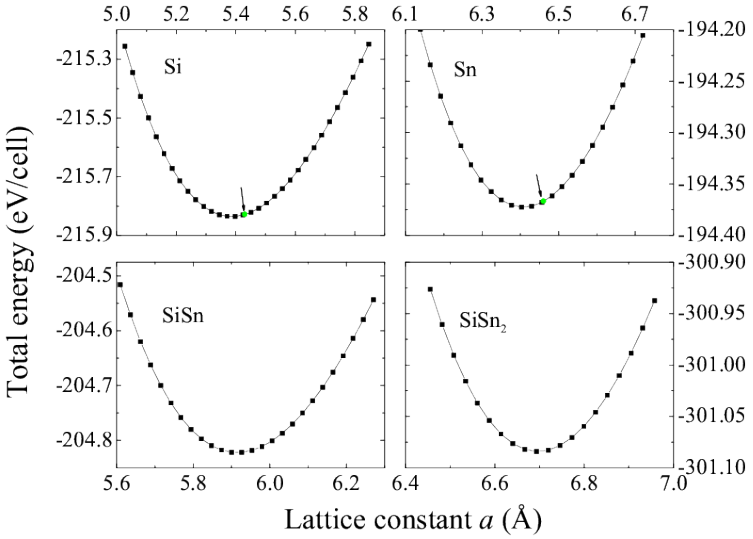

Figure 4.8: The total DFT energy versus the lattice constant a for Si (top left), α-Sn (top right), SiSn (lower left), $SiSn_2$ (lower right). Experimental values for Si and Sn are marked by arrows and green dots.

Compound	Energy/cell	a_0	Cost of formation/atom
Si	-215.84 eV	5.43Å	0
α-Sn	-194.37 eV	6.49Å	0
SiSn	-202.04 eV	5.93Å	3.07 eV
$SiSn_2$	-300.97 eV	6.68Å	0.41 eV

Table 4.1: Total energy calculated for Si, α-Sn, SiSn and $SiSn_2$, the equilibrium lattice constant a_0 and the cost of formation per atom in SiSn and $SiSn_2$ relative to Si and α-Sn.

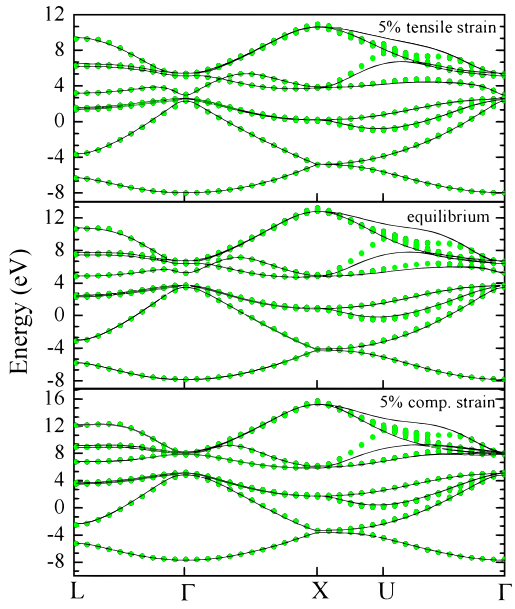

Figure 4.9: DFT+GW band structure for SiSn (points) and TB fit (lines). Top panel is for 5% tensile strain applied to the geometry, middle is equilibrium and the lower is for 5% compressive strain.

stabilization of this compound is not easy.
Following the initilization and relaxation of the geometry, we calculated the LDA band structure including SOI under -5%, 0% and 5% tensile strain. Following a procedure similar to that used for α-Sn, we proceeded to calculate GW corrections and applying them to the LDA band structure. Finally, we fit tight binding parameters to the corrected band structures, this was done by using a mix of Si[99] and α-Sn[59] *sp* parameters, including up to third nearest neighbour, as an initial guess. The error between the TB band structure and the DFT band structure within the $L \to \Gamma \to X$ path in $\vec{k}$-space was then minimized by varying the TB parameters. The corrected band structures and their fits may be seen in fig. 4.9. Within the fitted region, the fit is excellent for all bands and even outside the fitted interval, the fit remains very good for all valence bands and the first conduction bands.

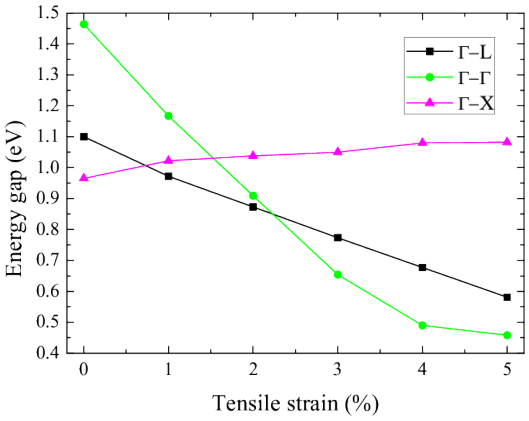

Figure 4.10: Calculated transition energies for the $\Gamma \rightarrow L$, $\Gamma \rightarrow \Gamma$ and $\Gamma \rightarrow X$ in SiSn, for varying degrees of tensile strain. The points are results from the calculation, the line serves as a guide to the eye.

While higher conduction bands may not be reproduced quite accurately, we are mostly interested in the lower conduction bands to determine the optical properties at low energies. We observe that SiSn is an indirect band gap semiconductor in equilibrium, whereas under 5% tensile strain, the gap has become direct. In order to further investigate the behaviour of this effect, we have calculated band structures for $1, 2, 3$ and 4% tensile strain as well. From these we have extracted $\Gamma \rightarrow \Gamma$, $\Gamma \rightarrow L$ and $\Gamma \rightarrow X$ transition energies and plotted them as a function of applied tensile strain, in fig. 4.10. As it turns out the transition to direct gap happens at $\approx 2.2\%$ tensile strain, a finding in good agreement with those of ref.[100], however we report a slightly larger direct band gap, due to the more accurate estimate of the conductions bands in the GW corrected calculation. From an applications point of view, this highlights the possibilities and importance of strain engineering of SiSn compounds, for instance for NIR applications. In order to further investigate what properties SiSn compounds will have, we turn our attention to the silicide $SiSn_2$. In contrast to the semiconducting nature of SiSn, $SiSn_2$ has metallic characteristics, as seen from the band structure in fig. 4.11. We attribute this behaviour to the silicide $SiSn_2$, having a more 'β-like" phase, contributing to metallic properties. This is also a possible explanation for the more favorable formation of $SiSn_2$ as compared to SiSn, following table 4.1, as the β-phase of Sn is more energetically favorable than the α-phase at

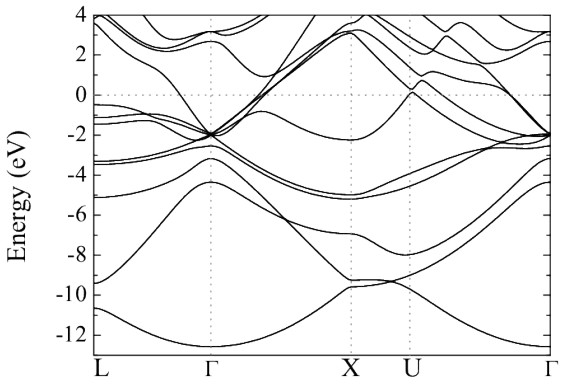

Figure 4.11: DFT band structure of $SiSn_2$, with the Fermi level at 0 eV, as marked by the dotted line.

room temperature. It should be kept in mind, that despite the lower cost of formation, this comes at the expense of a large lattice mismatch with Si and as such, some of this lower cost of formation is offset by strain energy. Under all circumstances, $SiSn_2$ formation could have detrimental effects to optoelectronic devices based on SiSn alloys. Finally, we wish to determine the optical properties of SiSn, following the method outlined in sec. 3.1.1. This method requires knowledge of the momentum matrix elements $p_{sp,Si}$ and $p_{sp,\alpha-Sn}$, in order to predict the optical properties of SiSn. The value $p_{sp,\alpha-Sn} = 3.2eV$ may be obtained from ref.[59], however the value of $p_{sp,Si}$ may not be readily retrieved from the literature. Thus, we adopt the TB parameters for Si from ref.[99] and calculate the optical spectra on this basis. Then these are fitted to the experimental spectra from ref.[75], via the matrix element $p_{sp,Si}$, such that the low energy features from the experiment are reproduced in the theoretical results. On the basis of this approach we arrive at $p_{sp,Si} = 5.2eV$, the resulting theoretical spectra compared to the experiment is shown in Fig. 4.12. The agreement is very reasonable in the sense that the low energy part of the spectrum is produced reliably. It is worth stressing that excitonic effects are not included and as such the low energy peaks are to be associated with intense band edge transitions and not exciton states. Lastly, the optical spectra of SiSn may then be calculated, now that we know both momentum matrix elements. Doing this for various strain configurations, the spectra may be seen in fig. 4.13.

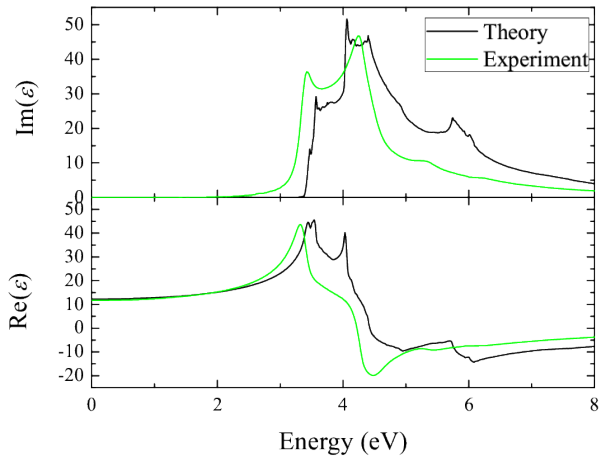

Figure 4.12: Calculated optical spectra for Si (black lines) compared to the experimental values (green lines) from ref.[75].

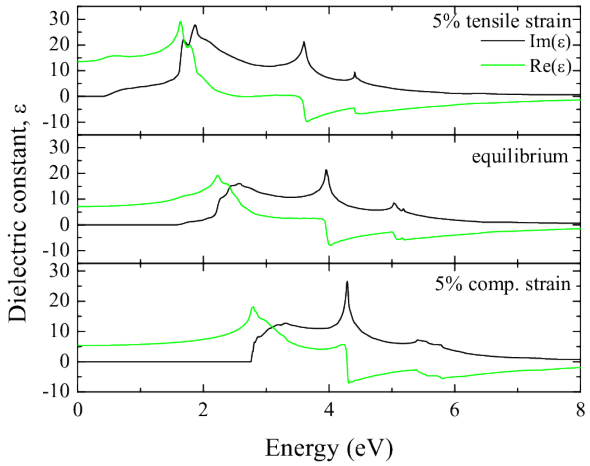

Figure 4.13: Calculated dielectric constant for SiSn under tensile strain (top panel), equilibrium (middle) and compressive strain (bottom). The black line is the imaginary part of ϵ and the green line is the real part.

Chapter 5

Experimental Results

5.1 Er^{3+} Lifetime in Silica

The goal of this study was to investigate photoluminescence properties of Er^{3+} in glass in theabsence of nanocrystals, as a function of annealing temperature. This is done in order to gain deeper insight into the interaction between nanocrystals and erbium particularly in low temperature annealed samples, where the environment around erbium certainly is more pertubed than in high temperature annealed glass.

5.1.1 Method

The SiO_2:Er samples are produced by depositing 100 nm of SiO_2:Er on a Si substrate, using magnetron sputtering. The SiO_2:Er+NC samples are produced by sputtering 20 periods of 2 nm Si and 4 nm SiO_2:Er on a Si substrate. Subsequently, the samples are annealed at 5-1100°C in N_2 for one hour. Finally some of the the samples are hydrogen passivated at 500°C for one hour in 5% H_2,95% N_2. The SiO_2:Er samples are available both with and without hydrogen passivation.
As the amount of light emitted by the non-sensitized samples is very low, particularly for the low temperature annealed samples, it is neccesary to make an experimental setup that is as sensitive as possible. Thus, a NIR-PMT is used in conjunction with a 1500 nm long pass filter for light collection. The advantage of this compared to a spectrometer is twofold, first of the entire Er^{3+} peak centered at 1535 nm is collected and second the losses inherent to a spectrometer are avoided. As the PMT is not sensitive in the area above 1650 nm, this gives a fairly narrow spectral window, still.
For excitation, a nanosecond pulsed Nd:YAG laser operating at 10 Hz in

conjunction with an optical parametric oscillator (OPO) is used. This allows for scanning the excitation wavelength, to pump Er^{3+} resonantly. To obtain time resolved spectra, an exictation wavelength is chosen and the trigger pulse from the laser triggers a multi-channel scaler, which temporally resolves the signal from the PMT. The wavelength used for excitation in the time resolved spectra is 520 nm, unless otherwise noted. A schematic of the experimental setup may be seen in fig. 5.1. Due to the temporal nature of the signal having an initial fast behaviour and a slow long component, a spectrum with high time resolution (80-320 ns) of the initial part of the complete spectrum is joined with a lower resolution spectrum with a longer time range.

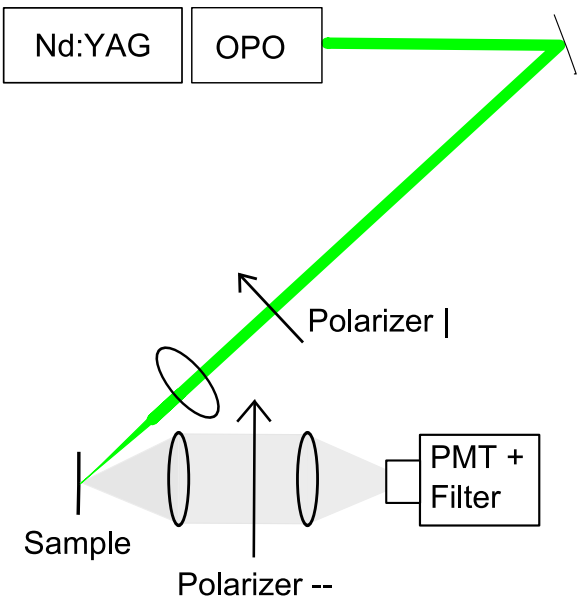

Figure 5.1: Experimental setup used to capture time resolved photoluminescence from samples with Er-doped silica deposited on top of Si. The trigger pulse from the Nd-YAG laser starts the multi-channel scaler which allows for temporal resolution of the photoluminescence recorded by the PMT.

5.1.2 Results and Discussion

First a PLE scan is performed, in order to assess which wavelengths are suitable for excitation and to ensure that only resonant excitation of erbium takes place in the samples, and that no significant sensitizing effects

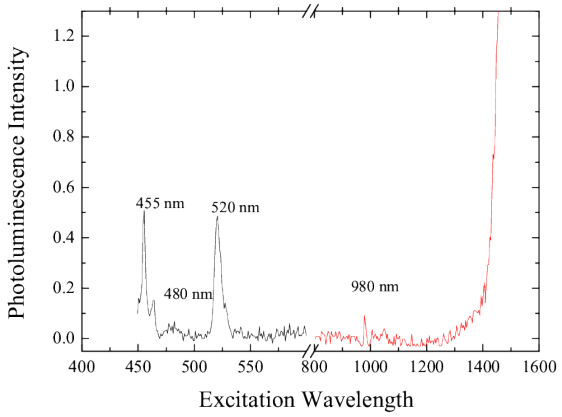

Figure 5.2: Photoluminescence at 1530 nm, from SiO_2:Er samples, as a function of the excitation wavelength. Peaks correspond to various energy transitions in Er^{3+}.

are present. Such a scan is seen in fig. 5.2. As is evident, only transitions corresponding to energy transitions in Er^{3+} yields any significant photoluminescence yield. The peak at 980 nm thus corresponds to excitation into the $^4I_{11/2}$ level, whereas the 520 nm peak corresponds to $^4S_{3/2}$ and higher energy peaks to even higher energy levels. The increase at 1400 nm and beyond corresponds to resonant excitation directly into the $^4I_{13/2}$ level. Samples annealed at lower temperatures exhibit the same behaviour. As such we are led to believe that there are no sensitizers present in our samples and only resonant excitation of Er is possible. Time resolved spectra are then obtained, with 520 nm excitation, as this yielded the most light output. Initial components of each spectrum, regardless of temperature, are characterized by an immediate fast decay, followed by an ingrowth and then finally a long, slow, temperature dependent decay ($3\mu s$-$10.5ms$). The vast majority of the emitted light is caused by the slow component. An example of such an emission pattern is shown in fig. 5.3. As excitation takes place into the $^4S_{3/2}$ level, the ingrowth may be explained by relaxation to $^4I_{13/2}$ being neccesary before emission can take place. However, emission with a fast temporal character does take place before this, this may be ascribed to fast processes (e.g. Auger) causing an initial high population of the $^4I_{13/2}$ level, with a subsequent fast process, such as upconversion, causing the quick depopulation of this initial population. The same behaviour

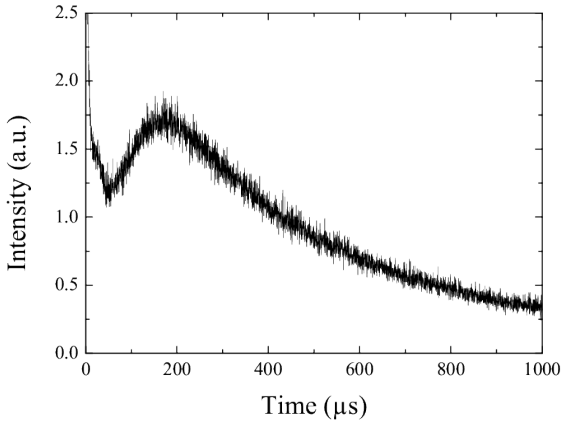

Figure 5.3: Time resolved spectrum from Er^{3+} in SiO_2, taken from a sample annealed at 900°C in N_2, followed by H-passivation at 500°C. The spectrum is characterized by an initial fast decay, followed by an ingrowth (≈ 100 μs) and a long, slow decay.

is found when pumping with 980 nm into the $^4I_{11/2}$ level. A similar result was found for SiO_2:Er with nanocrystals in ref.[22], in this paper where the erbium was sensitized by nanocrystals the initial fast population was ascribed to hot carriers in the nanocrystals relaxing to the ground exciton state and exciting the erbium to the $^4I_{13/2}$ state. Obviously, this can not be the case here, although a somewhat similar explanation may be feasible. In any case, both with and without nanocrystals, this is an area worthy of much more study, though one often overlooked as the focus is often on steady state PL or the slow PL from erbium. However, we will focus on the slow component from now and onwards. As is seen in fig. 5.4, the decay time is generally increasing with temperature. This is not surprising and the case of deposited glass annealed at low temperatures is somewhat comparable to glass damaged during ion implantation of Er-ions. In such studies[101,102], an increase in erbium lifetime is also observed with increasing anneal temperatures, this is believed to be due to the glass having many defects, introducing non-radiative pathways which leads to shortening of the $^4I_{11/2}$ lifetime. These defects are annealed away as temperature increases, inhibiting non-radiative pathways. The non-passivated samples show a large deviation for the low-temperature annealed samples and no explanation for this is readily available. However it is remarkable that the high temperature

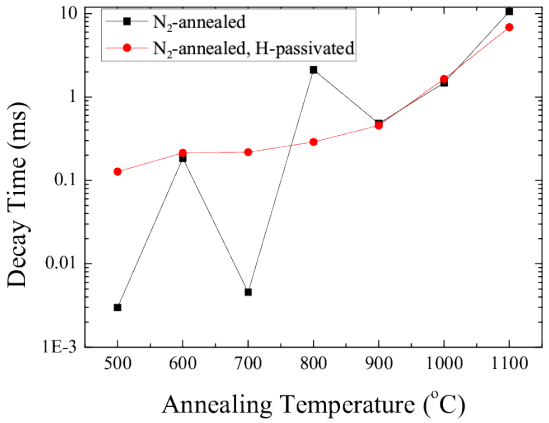

Figure 5.4: Lifetime of the slow part of the 1530 nm emission from SiO_2:Er samples at various annealing temperatures, for both unpassivated and H-passivated samples.

annealed non-passivated sample shows longer decay than the H-passivated sample. The value of 10.58 ms for the non-passivated sample is close to that observed in high quality SiO_2 [30] and is a sign that a good defect free film is formed. The quicker decay of the H-passivated sample may actually be because of OH-defects being introduced during passivation, leading to more non-radiative pathways being available in the H-passivated samples. The total yield, in this case the time-integrated signal from each sample, is illustrated in fig. 5.5. For the hydrogen-passivated samples there is a tendency towards growth, some plateauing at 700-800$°C$ and then further activation as the temperature is increased. The general tendency of increasing yield with temperature is in part explained by the longer lifetime of each excited erbium ion as the annealing temperature increases and the glass environment of the erbium ion becomes more defect free. The effect of hydrogen annealing on the total yield in these samples is uncertain and due to the variance observed in the lifetime of the the non-passivated samples, further investigation is needed to draw final conclusions on this part of the subject. From an applications point of view, however, it is highly relevant to be able to access as many erbium ions as possible in the material. To get an estimate of how many erbium ions are excited in the samples, relative to eachother we need to compensate for the non-radiative decay. Thus we calculate the

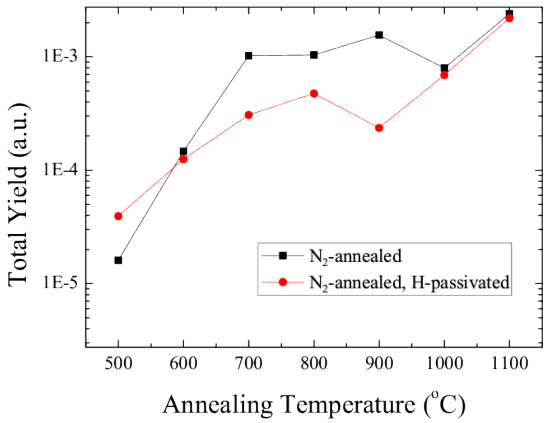

Figure 5.5: Total yield from the 1530 nm peak, from SiO_2:Er samples annealed at various temperatures, for both unpassivated and H-passivated samples.

active erbium concentration, in a simple 2-level picture from

$$Y \propto [\mathrm{Er}^{3+}]\frac{\tau}{\tau_{rad}} \tag{5.1}$$

where τ_{rad} is the radiative lifetime of erbium in absence of non-radiative pathways and τ is the measured decay time for a given annealing temperature. Due to the variance in the non-passivated samples, the relative erbium activation is only estimated for the passivated samples and is plotted in fig. 5.6. As is seen the optimal erbium activation takes place around 800°C which is consistent with the results found in ref. [102]. At higher temperatures, starting cluster formation may lead to a lower amount of active erbium ions. However, this effect is disguised in the yields, as non-radiative pathways quench a great deal of the luminescence at low anneal temperatures. We now turn our attention towards the samples where erbium is sensitized with nanocrystals.

5.2 Effective Er^{3+} Cross Section in SiO_2:Er+NC

The aim of this series of experiments was to investigate the dependence of photoluminescence properties of SiO_2:Er+NC as a function of the annealing temperature. This includes both steady state and transient behaviour, from

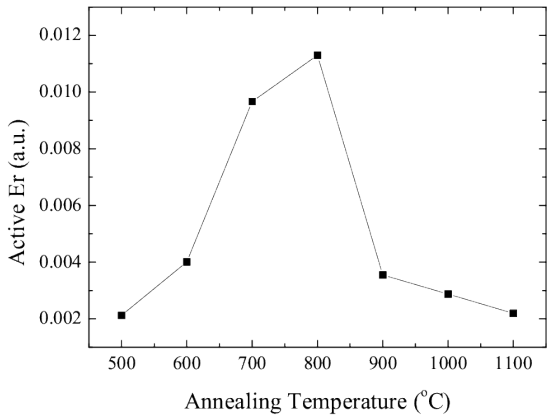

Figure 5.6: Approximation of the relative activation of Er^{3+} in different samples as a function of the annealing temperature in H-passivated samples.

the latter it is possible to extract the effective cross section for Er^{3+} in the presence of nanocrystals and gain deeper understanding of the interaction.

5.2.1 Method

The samples are made by depositing multiple alternating layers of 2 nm Si and 4 nm SiO_2:Er on a Si substrate using magnetron sputtering. The samples are then annealed at temperatures from 500-1150°C in N_2 for 1 hour and are then passivated in 95% N_2, 5% H_2 for 1 hour.
The experimental setup is somewhat the similar to the one in fig. 5.1, but except for a pulsed laser, an Ar^+-ion laser at 488 nm is used in conjunction with a chopper wheel triggering the multichannel scaler, this allows for long pulses with lower intensity, which is neccesary to record the rise time. Instead of a longpass filter, a monochromator is used in conjunction with the PMT. Initial steady state photoluminescence is recorded with the chopper wheel off. Time resolved spectra are recorded with the chopper wheel at varying frequencies from 55-210 Hz depending on the decay time of the sample. To calculate the effective cross section, we measure the rise time at varying pump intensities, with a known spotsize. The spotsize was measured by sweeping a razor blade through the beam at the sample position in along the long and short axis of the beam, as the incoming beam is elliptical. To vary the pump intensity a set of polarizers are used, by varying the angle of

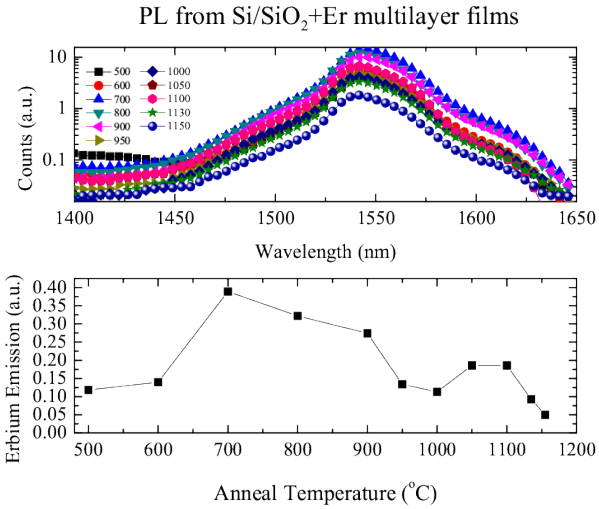

Figure 5.7: Top: Photoluminescence spectra from SiO_2:Er+NC samples annealed at various temperatures. Bottom: Integrated photoluminescence signal as a function of the sample anneal temperature.

the first polarizer with respect to the second, it is possible to regulate the incoming power.

5.2.2 Results and Discussion

As is apparent from fig. 5.7 the spectral shape of the erbium-related emission does not change appreciably with the annealing temperature, meaning that the energy levels in the Er^{3+} ion are not significantly altered by the slightly varying glass environment. The integrated erbium luminescence does, however change significantly, leading to maximum luminescence at 700°C, before decreasing and having a local maximum at 1100°C and decreasing again at higher temperatures. The phenomenon at 700°C is seen in the litterature[40–42] and ascribed to so called luminescence centers being formed at these lower annealing temperatuers and acting as erbium sensitizers. As temperature increases crystalline Si nanocrystals are formed and act as sensitizers. When temperature is increased even further, the Si starts to melt together and the structure of the films breaks down. Next, the decay time of the Er^{3+} luminescence at 1530 nm is measured and fitted with a bi-exponential. The $1/e$ lifetimes as a function of the annealing temperature are seen in fig. 5.8, as is seen there is a local maximum at 800°C, and a

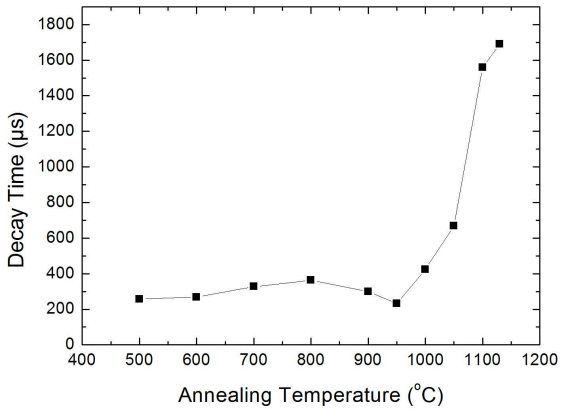

Figure 5.8: Decay times for erbium in SiO_2:Er+NC samples as a function of the annealing temperature.

general increase with temperature. The general increase with temperature is easily understood in terms of the glass forming a more ordered network leading to longer Er^{3+} lifetimes, as is also seen for the case of SiO_2:Er. The local maximum at 800°C may possibly arise from the fact that amorphous nanocrystal formation starts to set in around 900°C, due to the increased silicon diffusion. This may bring even further disturbances to the glass network, before a temperature high enough to fully repair the glass is met and a decay in the ms regime is met. In any case, the decay times are faster than in the pure silica samples, which is likely due to the disturbances brought by the increased silicon content in the samples. The natural question to ask is, if decay times are not particularly slow, e.g. we possibly have a high amount of non-radiative channels, why is the luminescence then maximized at 700-800°C?. Two possible scenarios are that the sensitizers are simply more efficient at some annealing temperature, another is that the number of sensitizers is maximized at some given temperature. A way to investigate this in detail is to determine the effective cross section for the erbium sensitized by the nanocrystals. In a simplified two-level picture of the Er-nanocrystal system, the cross section may be derived from,

$$\frac{1}{\tau_{rise}} = \sigma\phi + \frac{1}{\tau_{decay}} \tag{5.2}$$

where σ is the (effective) cross section, ϕ is the incoming photon flux, and τ_{rise} and τ_{decay} are the rise and fall times of the erbium luminescence, under

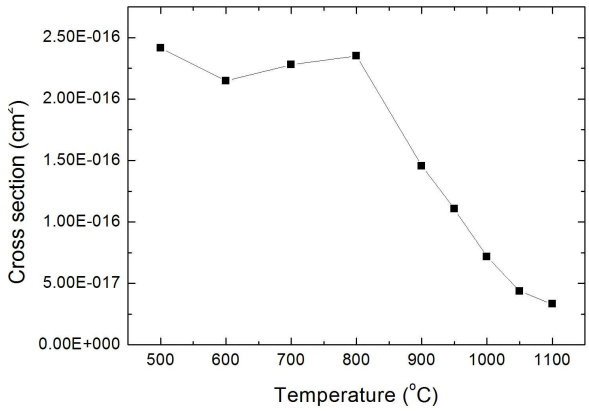

Figure 5.9: Effective cross section for erbium in SiO_2:Er+NC, as a function of the annealing temperature.

long-pulsed excitation. By varying the excitation intensity, the cross section may thus be determined. As is seen in fig. 5.9 the cross section remains almost constant until $800°C$, where it drops off and decreases with increasing anneal temperature. As such, it seems as if the formation of nanocrystals that takes place changes the interaction dynamics between erbium and sensitizer. Up to $800°C$ it would appear that the number of sensitizers is optimized, as the luminescence is maximized here, dispite the effective cross section not being increased. As was seen in sec. 5.1, $800°C$ is also around the temperature that yields the highest active Er fraction, which may in part explain why sensitization is optimized at this temperature. For the high temperature annealed samples, it appears that the crystalline nanocrystals are not neccesarily the best sensitizers in terms of cross section, but are mostly aided by more efficient erbium luminescence from the much more ordered silica matrix.

5.3 Er^{3+} Diffusion in Silica

The interaction between nanocrystals and Er^{3+} in silica is one that has been much discussed and investigated, yet some controversy is still present regarding which mechanism is at play. Commonly, one wishes to determine the distance dependence of the interaction, in order to ratify whether a Förster or Dexter interaction is in play, as discussed in section 2.3.3. However, high

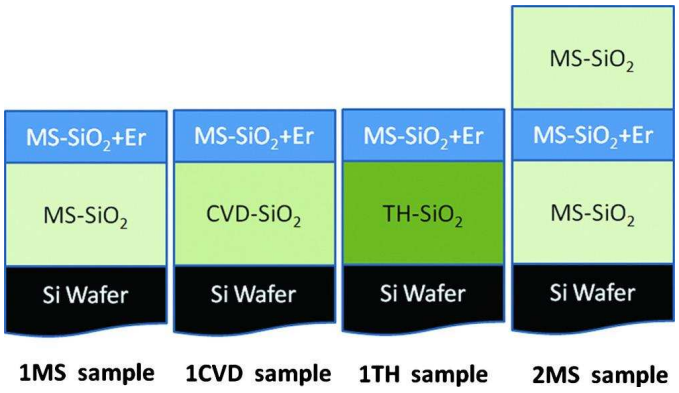

Figure 5.10: Illustration of the film structure, for determing erbium diffusivity. In the MS films the thickness of the SiO_2 layer was 350 nm, in the CVD layer it was 220 nm, in the TH layer it was 250 nm. In all cases the SiO_2+0.2 at.% Er layer was around 50 nm.

temperatures are needed in order to form crystalline nanocrystals in the films considered for such an interaction study. It becomes a valid, but largely ignored, question whether erbium diffusion plays a significant role, which we set out to investigate in[54]. Thus the aim was to determine the diffusivity for erbium in silica, by using SIMS (Secondary Ion Mass Spectroscopy)

5.3.1 Method

A number of samples were prepared on top of Si wafters, consisting of 220-350 nm of SiO_2 with around 50 nm of magnetron sputtered SiO_2 + 0.2 at% Er on top were prepared. The pure SiO_2 layers were prepared by both magnetron sputtering (MS), chemical vapour deposition (CVD) and thermal heating in a wet oxygen ambiance (TH), to investigate the effect of differently grown SiO_2. Finally, in the MS system, a sample with SiO_2 on both sides of the SiO_2+Er layer was prepared. For an overview of the samples, see fig. 5.10. After preparation the samples were cut in pieces, one piece from each sample was used as a reference and the rest were annealed at temperatures from 1000-1100°C for 1.5-7 hours, with lower temperature samples annealed for longer times, due to the lower diffusion rate at lower temperature.
Er concentration profiles were then obtained by secondary ion mass spectroscopy (SIMS) of samples both before and after annealing. In the instrument a $100 \times 100 \mu m^2$ area was sputtered with Bi^+ ions, while Cs^+ ions were

used for the mass analysis of the area. To convert the sputtering time to a depth scale, the sputtered crater depth was subsequently determined with a surface profiler.

5.3.2 Results and discussion

To determine the diffusion rate, the concentration profile of the as-deposited sample was convolved with a Gaussian function $f(x) = A/(\sqrt{2}\pi\sigma)\exp(-x^2/2\sigma^2)$ to best reproduce the concentration profile from the annealed samples. This corresponds to diffusion according to Fick's second law, with $\sigma^2 = 2Dt$, where D is the diffusion coefficient and t is the annealing time. The front factor A, close to unity, is to compensate for slightly different areas under the distributions. An example of this fit may be seen in fig. 5.11, for the MS-SiO_2/SiO_2+Er/MS-SiO_2 sample annealed at $1100°C$. As is obviously apparent, Er has diffused into the pure SiO_2 layers on both sides and no surface effects are apparent. Investigating the diffusion coefficient at different temperatures, as seen in fig. 5.12 allows to determine the temperature dependence of the diffusion coefficient according to the Arrhenius equation

$$D(T) = D_{T_0} \exp\left[-\frac{\Delta E}{k_b}\left(\frac{1}{T} - \frac{1}{T_0}\right)\right], \tag{5.3}$$

where k_b is Boltzmann's constant, T is the anneal temperature, T_0 is the reference temperature and ΔE is the activation energy. Fitting according to this, we obtain an activation energy $\Delta E = 5.3 \pm 0.1$ eV, with the prefactor $D_{T_0} = 1.76 \pm 0.08 \cdot 10^{-16}$ cm^2/s at a reference temperature $T_0 = 1346°$ K, with the uncertainties coming from the statistical error of the fit and a 2% uncertainty of the depth scale. Diffusion was also investigated in the one-layer samples, however a surface effect causing pile-up of Er takes place, which was not investigated further, instead only a region at least a diffusion length away from the surface was fitted. The results from these samples are also shown in fig. 5.12. Somewhat surprisingly, the diffusion coefficient is not very sensitive to the type of SiO_2, in fact diffusion in the less dense MS-SiO_2 appears to be faster than in CVD or thermal SiO_2, however this is within the statistical error of the experiment and as such demand further investigation. Compared to the 2MS sample, the diffusion coefficients from the one-layer samples appear greater by a factor of two, even for the 1MS sample, which certainly indicates some surface effect that is not understood at this point.
Most importantly, however, is the determination of a diffusion constant for Er in SiO_2, which is relevant under any circumstances. For instance, if we

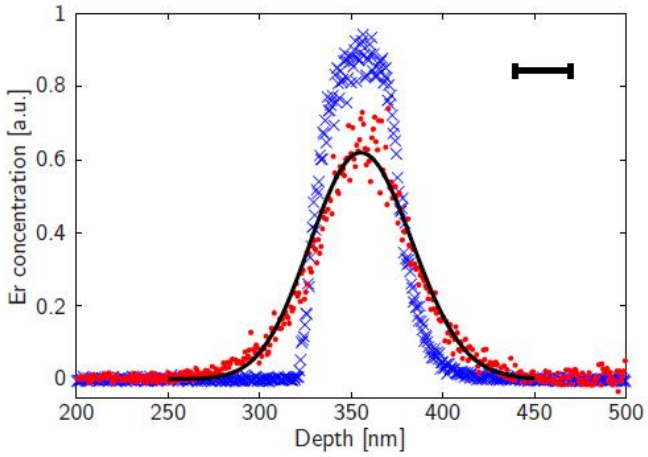

Figure 5.11: The Er SIMS profile of the MS-SiO_2/SiO_2+Er/MS-SiO_2 sample before (blue crosses) and after annealing at 1100° C (red dots) as well as the fitted result (black line), corresponding to a diffusion length, $L = 2\sqrt{Dt}$ of 31 nm.

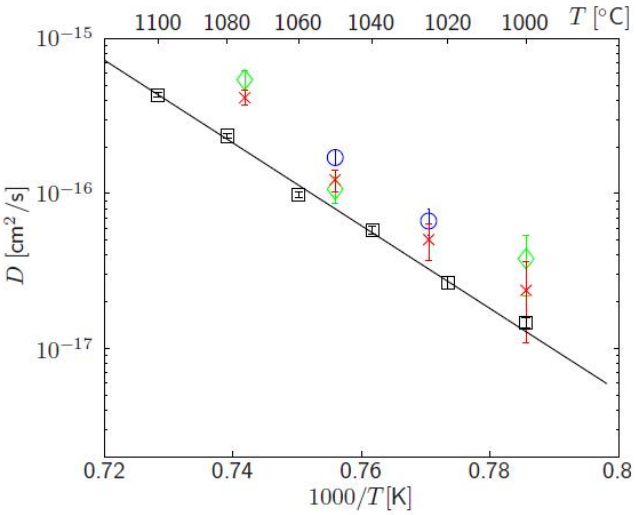

Figure 5.12: Diffusion coefficient versus temperature for Er in thermally grown SiO_2 (blue circles), CVD grown SiO_2 (green diamonds) and magnetron sputtered SiO_2 (red cross). The black straight line is an Arrhenius fit according to eq.5.3.

want to perform an experiment with a buried SiO_2+Er layer and annealing takes place at 1100°C, for 1 h, we obtain a diffusion length of 25 nm. Clearly, any subsequent assumptions about the Er only being in the buried layer following the anneal will be wrong.

5.4 Nanocrystal-Er^{3+} Interaction Distance

Having now determined the importance of erbium diffusion, it is possible to properly design an experiment to determine the distance dependence of the interaction between Er^{3+} and Si nanocrystals. From this it should be possible to infer whether a Förster or Dexter mechanism is responsible for the interaction. Thus, the goal was to determine the distance dependence of the interaction mechanism.

5.4.1 Method

The samples are produced by RF-magnetron sputtering, with the substrate heated to 200°. The sample structure is illustrated in fig. 5.13. First a buffer layer of SiO_2 is deposited, followed by 10 superlayer structures consisting of (10 - d) nm SiO_2, d nm SiO_2:Er and 1.5 nm Si, finally a 50 nm SiO_2 capping layer is applied. The thickness, d, of the SiO_2:Er layer is varied and samples with 0, 0.3, 0.6, 0.9, 1.2, 1.5, 2.0 and 3.0 nm are fabricated. The samples are annealed at 700° C in N_2 for one hour, followed by hydrogen passivation in 95% N_2 and 5% H_2. The annealing temperature and time was kept at 700°C, as previous studies[54] have shown that this should give no appreciable diffusion of erbium in silica, thus the position of the erbium in relation to the silicon is well-defined. The samples are excited by a continous wave laser diode at 405 nm, with the pump flux being adjusted by varying the spot size on the sample. Photoluminescence above 1100 nm was detected with a monochromator and a near-infrared sensitive photomultiplier tube. Photoluminescence at 700-1100 nm was detected using a CCD.

5.4.2 Results and Discussion

The samples exhibit broadband Si-related photoluminescence from 700 nm and upwards as well as a characteristic and much more intense peak centered around 1535 nm arising from Er^{3+} $^4I_{13/2} \rightarrow ^4 I_{15/2}$ luminescence.
The total PL-yields from the Si and Er peaks from the 3.0 nm Er-layer sample are plotted in fig. 5.14 as a function of the pump intensity. The Er intensity yields information about the efficiency of the sensitization, whereas

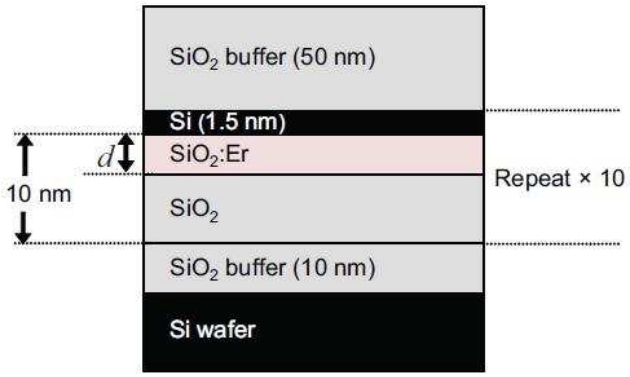

Figure 5.13: Sample structure used for determining the interaction distance. Multilayer samples with increasing SiO_2:Er layer thickness, with the total layer thickness constant are fabricated.

the Si intensity gives information about electron-hole dynamics in the Si sensitizing layer. While the Si peak seems to scale linearly with the pump intensity, the Er peak exhibits saturation at high pump intensities, owing to a finite number of Er ions that can be excited and decay radiatively, which sets the upper limit for the Er peak.
We assume the energy transfer rate between erbium and sensitizer to be on a simple one-dimensional form, $P(x) = P_0 \exp(-x/x_0)$, where x is the distance between sensitizer and erbium and x_0 is the characteristic interaction distance. Defining Γ as the decay rate of the $^4I_{13/2}$ state, the total luminescence yield as a function of d in the limit $d \gg x_0$ can be found to be:

$$Y_\infty = C \ln\left(\frac{P_0}{\Gamma} + 1\right) \equiv A I_{sat} \ln\left(\frac{I}{I_{sat}} + 1\right), \tag{5.4}$$

where I_{sat} is the intensity required to for having the pumping rate P_0 equal to the decay rate, Γ. In the linear regime, $I \ll I_{sat}$, A is the slope. This model has been fitted in fig. 5.14, the agreement is very reasonable and reproduces the logarithmic behaviour at large intensity, although no saturation is observed. In the following we will use I_{low} for the intensity in the regime where the behaviour is linear and I_{high} in the regime where saturation effects play a role, both are marked in fig. 5.14. The yield is now measured at low and high intensities for the different samples and is plotted as a function of the Er-layer thickness in fig. 5.15, as well as the ratio of high and low yield versus thickness. Although there are some sample variation related errors to the measurements, there is a clear difference between the distance de-

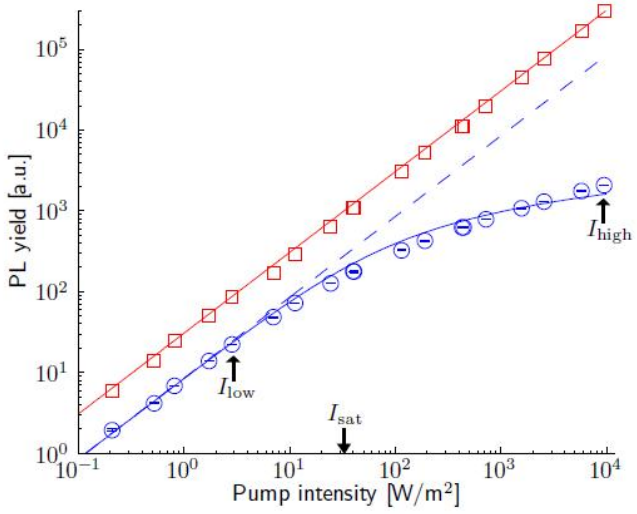

Figure 5.14: The photoluminescence yield from the 1535 nm Er^{3+} peak (circles) and from the nanocrystal-related luminescence at 750-900 nm (squares), as a function of the pump intensity, taken on the sample with 3.0 nm Er-layer.

pendence for the low (panel (a)) and high (panel (b)) excitation intensities. The higher excitation rate and thus saturation effects causes the interaction distance to appear longer. This is examined further in panel (c) where the normalized ratio of high to low-excitation intensity is shown, which has the advantage of cancelling out systematic sample-to-sample variation. From panel (c) it is very clear that the yield ratio increases with increasing Er-layer thickness. We chose the model $Y = A[1 - \exp(-x/x_0)]$, corresponding to a one-dimensional Dexter model, to describe the distance dependence of the interaction. To model the yield ratio we thus arrive at the expression

$$\frac{Y_{high}}{Y_{low}} = A\frac{1 - \exp(-x/x_{high})}{1 - \exp(-x/x_{low})}. \tag{5.5}$$

This model apparently fits the data quite nicely, with the fitting parameters $x_{low} = 0.21 \pm 0.06nm$ and $x_{high} = 0.54 \pm 0.10nm$ and $x_{high}/x_{low} = 2.6 \pm 0.4$. The yield models for Y_{high} and Y_{low} are also added to the corresponding panels, with the interaction distances derived from the fit to panel (c). This gives a better estimation to x_{low} as compared to what we would get from fitting to panel (a), as the result from such a fit is very sensitive to the

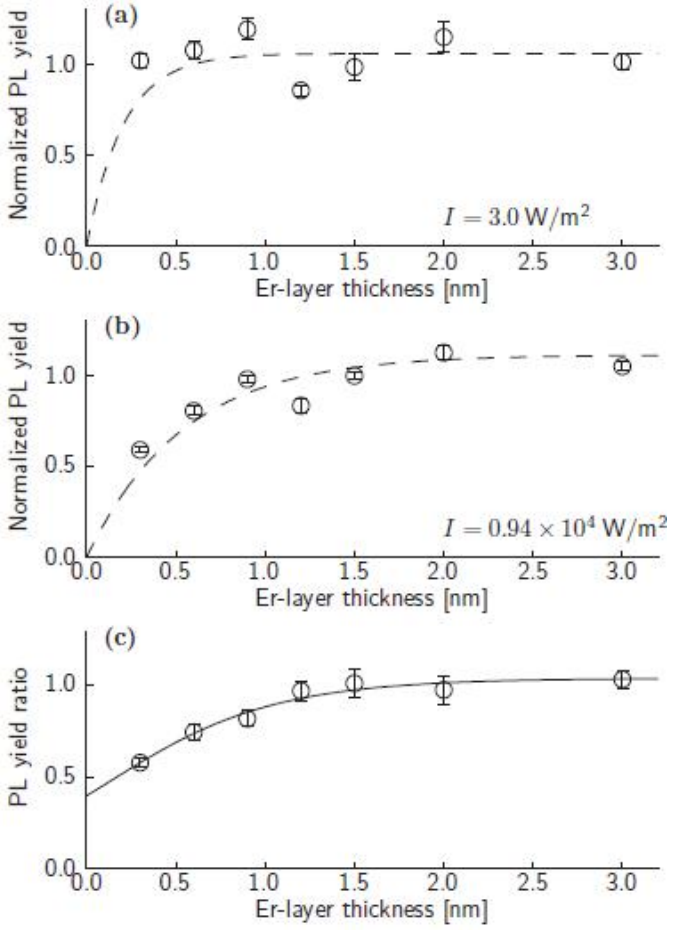

Figure 5.15: Dependence of the integrated photoluminescence around 1535 nm, from Er^{3+} on the Er-layer thickness. Panels (a) and (b) were recorded at low and high intensities. In panel (c) the ratio of yields at high and low intensities, Y_{high}/Y_{low} is plotted and fitted to eq.5.5.

uncertainty arising from sample-to-sample variations. We now turn to the Si luminescence as a function of the erbium layer thickness, seen in fig. 5.16 for both low (panel (a)) and high pump (panel (b)) fluences. As is evident in both cases, the yield decreases with the layer thickness over the entire range and no saturation effects are apparent. A model, $y = A_1 \exp(-d/x_1) + A_2 \exp(-d/x_2)$ is used to fit the data, with the first term describing the short range interaction with the erbium ions and the second term a long range interaction term. The fit to the low intensity excitation is $x_1 = 0.21 \pm 0.03$ nm, $x_2 = 4.2 \pm 1.2$ nm, and $A_2/A_1 = 0.19 \pm 0.04$. For panel (b) we obtain $x_1 = 0.24 \pm 0.05$ nm, $x_2 = 2.9 \pm 0.6$ nm and $A_2/A_1 = 0.40 \pm 0.09$. Indeed, the x_1 term is found within uncertainties to be the same as the low-intensity sensitizer-erbium interaction distance x_{low}. As such it would appear that the short-distance interaction is insensitive to the pump flux. The Si luminescence is always quenched by the presence of Er ions, regardless of pump intensity (see fig. 5.16) but show no saturation effect, as seen in fig. 5.14. As such a constant proportion of energy seems to flow to the Er, if no unexcited Er is available, excitation to higher levels than $^4I_{13/2}$ takes place, leading to no additional Er luminescence and thus a saturation effect for Er. In summary, saturation effects play a significant role when trying to estimate the characteristic interaction distance. Such a behaviour has been observed previously [103] and it was suggested that Er-Er energy transfer leads to the increased length scale. This can not be ruled out, however it is apparent that the saturation effect is significant, as it dominates the short scale interaction at higher pump intensities.

It is also noteworthy that the interaction distance found is so short that it is in essence inter-atomic and thus on the limit of experimental resolution, as also noted elsewhre [56]. However it is easily seen from the distance depence of the yield ratio in fig. 5.15, that there must be a distance dependence of the transfer mechanism, as otherwise each erbium ion would be excited and saturate in the same manner, which is clearly not the case. Whether a Förster or Dexter interaction is responsible for the energy transfer is not totally clear, as a 3D Förster model may give rise to a similar plane-to-plane behaviour, as noted in [104]. What is certain is that the interaction distance is very short, 0.22 ± 0.02 nm, on the order of inter-atomic distances and thus wave function overlap is a requirement for efficient transfer. As seen for the Si yield, additional processes may take place in addition to the Si-Er energy transfer, which may prove an interesting topic for further investigation.

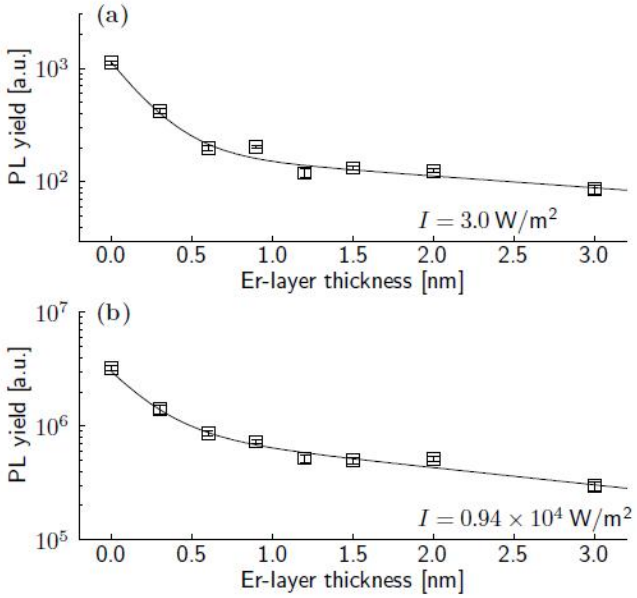

Figure 5.16: Dependence of the integrated photoluminescence at 700-950 nm, from the nanocrystals, as a function of the Er-layer thickness. Panels (a) and (b) are obtained at low and high pump flux. Lines are fitted as double exponential decays.

Chapter 6

Summary

Ever since photoluminescence was first realised from quantum confined carriers in porous silicon, the development towards integrated nanocrystal systems compatible with conventional silicon processing technology has been very rapid. In particular erbium doped silica with nanocrystals is a promising candidate for optoelectronic integration. However a number of questions still remain unanswered for this system.

The work in this thesis is divided in two, the first concerns understanding and optimizing the interaction between erbium and silicon nanocrystal sensitizers. The second investigates alternative structures in the form of α-Sn, embeddable in silicon, that may be used for optoelectronic application.

With regards to the first topic, erbium and Si nanocrystals, the annealing conditions for formation and sensitizing were studied and an optimum was found at around 700-800°C, in agreement with previous experiments. Annealing conditions for erbium in silica was then studied as an isolated system and it was found that optimal activation of erbium takes place at around 800°C, which is lower than the temperature needed to form crystalline nanoclusters. This effect may explain the lower yield in the nanocluster-erbium samples at higher annealing temperatures.

The diffusion characteristics of erbium in silica was found and the diffusion coefficient with respect to temperature was found. The interaction between nanocluster and erbium was then studied by varying the distance between thin silicon layers and thin erbium-doped silica layers. The samples were processed at temperatures allowing minimal erbium diffusion, yet high enough to allow nanoclusters to form. It was found that the interaction is very short-range, on the order of 0.5 nm, which in practice makes it hard to discern between a Förster or Dexter interaction, although it is likely to be

the latter.
Concerning α-Sn, a DFT calculation of the band structure including the GW correction for the conduction band was carried out for varying degrees of strain. Tight binding parameters were fitted to these band structures, providing an excellent fit. To test these parameters, the optical absorption spectrum was calculated from the tight binding band structure and compared with experiment, again providing excellent agreement. The tight binding parameters were then applied to α-Sn nanocrystals and the band gap and optical absorption was investigated as a function of nanocrystal size and applied strain. We found α-Sn nanocrystal to be exciting candidates for integration with silicon, providing a tuneable band gap all the way into the near-infrared. Finally we investigated zinc-blende Si-Sn and $SiSn_2$ in the GW framework in order to assess its role as a candidate for optoelectronics. While we found $SiSn_2$ to be a metallic phase, we found SiSn to become a direct gap semiconductor at 2.2% applied tensile strain, with a band gap of 0.85 eV. At lower strain we found it to be an indirect band gap semiconductor, like Si. We then fitted tight binding parameters to the SiSn band structures and calculated the optical spectra, which reflected the electronic properties well. This confirmed the notion of SiSn also being a promising candidate for optoelectronic integration with Si.

Chapter 7

Summary in Danish

Lige siden fotoluminescens fra kvantebegrænsede ladningsbærere første gang blev observeret i porøst silicium, er der sket massiv forskning i at integrere nanokrystallinske systemer med konventionel silicium teknologi. Særligt erbium doteret silika indeholdende nanokrystaller er et lovende bud med henblik på optoelektronisk integration. Der er dog stadig en række ubesvarede spørgsmål der trænger sig på, for dette system.
Arbejdet i denne afhandling er delt i to; den første del handler om forståelse og optimering af interaktionen imellem erbium og sensitiverende silicium nanokrystaller. I den anden del undersøges alternative strukturer til nanokrystal-erbium systemet, i form at α-Sn indlejret i silicium, som også er en potentiel kandidat til optoelektroniske anvendelser.
For erbium og Si nanokrystaller har vi undersøgt hærdningsbetingelserne for dannelse og sensitivering og fundet en optimal temperatur ved 700-800$^{\circ}C$, i overensstemmelse med andre forsøg. Hærdningsbetingelserne for erbium i silika, uden nanokrystaller, blev efterfølgende undersøgt og vi fandt optimal aktivering af erbium ioner ved omkring 800$^{\circ}C$, hvilket er lavere end den temperatur der skal til for at danne krystallinske nanokrystaller. Denne effekt er en mulig forklaring på den lavere effektivitet der observeres i nanokrystal-erbium prøver ved højere hærdningstemperaturer.
Diffusionsegenskaberne for erbium i silika blev efterfølgende undersøgt, og diffusionskonstanten blev bestemt som en funktion af temperaturen. Med denne viden blev interaktionen imellem nanokrystaller og erbium undersøgt, ved at variere afstanden imellem tynde silicium lag og tynde erbium-doterede silika lag. Prøverne blev bagt ved temperaturer der sikrede minimal erbium diffusion, men høj nok temperatur til at danne nanokrystaller. Det blev vist at interaktionsafstanden er meget kort, omkring 0.5 nm, hvilket i praksis

gør det svært at skelne imellem en Förster eller Dexter interaktion, selvom det er mere sandsynligt at det er den sidstenævnte.
For α-Sn har vi lavet DFT beregninger af båndstrukturen, inklusive GW korrektioner til ledningsbåndene, under forskellige grader af træk og tryk. Disse båndstrukturer dannede udgangspunkt for et fit af tight binding parametre. For at afprøve disse parameter blev det optiske absorptionsspektrum for α-Sn beregnet på baggrund af dem og sammenholdt med det eksperimentelle spektrum, med glimrende overensstemmelse imellem teori og praksis. Efterfølgende brugte vi tight binding parametrene til at undersøge α-Sn nanokrystaller og båndgabet såvel som den optiske absorption blev undersøgt som funktion af nanokrystal størrelse og træk/tryk. Resultaterne viser at α-Sn nanokrystaller er spændende bud på et integrerbart system i silicium, i kraft af et tunbart båndgab der går hele vejen ud i den infrarøde del af spektret. Endelig undersøgte vi zinc-blende Si-Sn og $SiSn_2$ inden for GW teorien, for at vurdere dets potentiale indenfor optoelektroniske anvendelser. Det blev fundet at $SiSn_2$ er en metallisk fase, men at SiSn er en halvleder der får et direkte båndgab under 2.2% træk, med et båndgab på 0.85 eV. Ved lavere træk er båndgabet indirekte, ligesom i silicium. Endelig lavede vi også et fit af tight binding parametre til SiSn båndstrukturen og brugte den til at udregne det optiske spektrum, hvilket afspejlede de elektroniske egenskaber. Dette bekræftede vores antagelse om at også SiSn kan være et interessant bud til optoelektronisk integration med Si.

Chapter 8

List of Publications

Publications

- T. G. Pedersen, C. Fisker and R. V. S. Jensen, "Tight-binding parameterization of alpha-Sn quasiparticle band structure", J. Phys. Chem. Solids, 71, 18 (2010)
- Y.-W. Lu, B. Julsgaard, M. C. Petersen, R. V. S. Jensen, T. G. Pedersen, K. Pedersen, B. B. Nielsen and A. N. Larsen, "Erbium diffusion in silicon dioxide", App. Phys. Lett, 97, 141903 (2010)
- R. V. S. Jensen, T. G. Pedersen and A. N. Larsen, "Quasiparticle electronic and optical properties of the Si-Sn system", J. Phys.: Condens. Matter, 23, 345501 (2011)
- R. V. S. Jensen, T. G. Pedersen and K. Pedersen, "Optical properties and size/shape dependence of alpha-Sn nanocrystals by tight binding", Phys. Stat. Sol. C, 8, 1002 (2011)
- B. Julsgaard, Y.-W. Lu, R. V. S. Jensen, T. G. Pedersen, K. Pedersen, J. Chevallier, P. Balling and A. N. Larsen, "Er sensitization by a thin Si layer: Interaction-distance dependence", Phys. Rev. B, 84, 085403 (2011).

Bibliography

[1] L. T. Canham. Silicon quantum wire array fabrication by electrochemical and chemical dissolution of wafers. *App. Phys. Lett.*, 57:1046, 1990.

[2] A. Halimaoui, C. Oules, G. Bomchil, A. Bsiesy, F. Gaspard, R. Herino, M. Ligeon, and F. Muller. Electroluminescence in the visible range during anodic oxidation of porous silicon films. *App. Phys. Lett.*, 59:304, 1991.

[3] Nobuyoshi Koshida and Hideki Koyama. Visible electroluminescence from porous silicon. *App. Phys. Lett.*, 60:347, 1992.

[4] A. G. Cullis, L. T. Canham, and P. D. J. Calcott. The structural and luminescence properties of porous silicon. *J. App. Phys.*, 82:909, 1997.

[5] M. A. Tischler, R. T. Collins, J. H. Stathis, and J. C. Tsang. Luminescence degradation in porous silicon. *App. Phys. Lett.*, 60:639, 1992.

[6] K. A. Littau, P. J. Swajowski, A. J. Muller, A. R. Kortan, and L. E. Brus. A luminescent silicon nanocrystal colloid via a high-temperature aerosol reaction. *J. Phys. Chem*, 97:1224, 1993.

[7] R. E. Johnson and A. Muan. Phase diagrams for the systems Si-O and Cr-O. *J. Amer. Cera. Soc.*, 51:430–433, 1968.

[8] L. Tsybeskov, K. D. Hirschman, S. P. Duttagupta, M. Zacharias, P. M. Fauchet, J. P. McCaffrey, and D. J. Lockwood. Nanocrystalline-silicon superlattice produced by controlled recrystallization. *App. Phys. Lett.*, 72:43, 1998.

[9] M. Zacharias, L. Tsybeskov, K. D. Hirschman, P. M. Fauchet, J. Bläsing, P. Kohlert, and P. Veit. Nanocrystalline silicon superlattices:

fabrication and characterization. *J. Non-Cryst. Solids*, 227-230:1132 – 1136, 1998.

[10] M. Zacharias, J. Heitmann, R. Scholz, U. Kahler, M. Schmidt, and J. Bläsing. Size-controlled highly luminescence silicon nanocrystals: A SiO/SiO_2 superlattice approach. *App. Phys. Lett.*, 80, 2002.

[11] G. Ghislotti, B. Nielsen, P. Asoka-Kumar, K. G. Lynn, A. Gambhir, L. F. Di Mauro, and C. E. Bottani. Effect of different preparation conditions on light emission from silicon implanted SiO_2 layers. *J. App. Phys.*, 79:8660, 1996.

[12] F. N. Timofeev, A. Aydinli, R. Ellialtioglu, K. Turkoglu, M. Gure, V. N. Mikhailov, and O. A. Lavrova. Visible photoluminescence from siox films grown by low temperature plasma enhanced chemical vapor deposition. *Sol. Stat. Comm.*, 95:443, 1995.

[13] T. Inokuma, Y. Wakayama, T. Muramoto, R. Aoki, Y. Kurata, and S. Hasegawa. Optical properties of Si clusters and Si nanocrystallites in high-temperature annealed SiO_x films. *J. App. Phys.*, 83:2228, 1998.

[14] Qi Zhang, S. C. Bayliss, and D. A. Hutt. Blue photoluminescence and local structure of si nanostructures embedded in SiO_2 matrices. *App. Phys. Lett.*, 66:1977, 1995.

[15] A. R. Wilkinson and R. G. Elliman. The effect of annealing environment on the luminescence of silicon nanocrystals in silica. *J. App. Phys.*, 96:4018, 2004.

[16] Fabio Iacona, Giorgia Franzo, and Corrado Spinella. Correlation between luminescence and structural properties of Si nanocrystals. *J. App. Phys*, 87:1295, 2000.

[17] C. G. Ross, D. Barba, and Martin F. Structure and luminescence of silicon nanocrystals embedded in SiO_2. *Int. J. Nanotechnol.*, 5:984, 2008.

[18] I. Stenger, B. Gallas, L. Siozade, C.-C. Kao, S. Chenot, S. Fisson, G. Vuye, and J. Rivory. Evolution of the optical properties of Si nanoparticles embedded in SiO_2 as function of annealing conditions. *J. App. Phys.*, 103:114303, 2008.

[19] J. Heitmann, F. Müller, M. Zacharias, and U. Gösele. Silicon nanocrystals: size matters. *Adv. Mater*, 17:795, 2005.

[20] A. J. Kenyon, P. F. Trwoga, C. W. Pitt, and G. Rehm. Luminescence efficiency measurements of silicon nanoclusters. *App. Phys. Lett.*, 73:523, 1998.

[21] S. Godefroo, M. Hayne, M. Jivanescu, A. Stesmans, M. Zacharias, O. I. Lebedev, G. Van Tendeloo, and V. V. Moschkalov. Classification and control of the origin of photoluminescence from Si nanocrystals. *Nat. Nanotech.*, 3:174, 2008.

[22] I. Izeddin, A. S. Moskalenko, I. N. Yassievich, M. Fujii, and T. Gregorkiewicz. Nanosecond dynamics of the near-infrared photoluminescence of Er-doped SiO_2 sensitized with Si nanocrystals. *Phys. Rev. Lett.*, 97:207401, 2006.

[23] M. L. Brongersma, P. G. Kik, A. Polman, K. S. Min, and H. A. Atwater. Size-dependent electron-hole exchange interaction in Si nanocrystals. *App. Phys. Lett.*, 76:351, 2000.

[24] C. Dufour, S. Chausserie, and F. Gourbilleau. Silicon-rich/silica multilayers: A means to provide a link between the excitonic 1D quantum confinement and the photoluminescence parameters. *J. Lumin.*, 129:73, 2009.

[25] L. Ferraioli, M. Wang, G. Pucker, D. Navarro-Urrios, N. Daldosso, C. Kompocholis, and L. Pavesi. Photoluminescence of silicon nanocrystals in silicon oxide. *J. Nanomat.*, page 43491, 2007.

[26] C. Delerue, G. Allan, C. Reynaud, and O. Guillois. Multiexponential photoluminescence decay in indirect-gap semiconductor nanocrystals. *Phys. Rev. B*, 73:235318, 2006.

[27] M. V. Wolkin, J. Jorne, P. M. Fauchet, G. Allan, and C. Delerue. Electronic states and luminescence in porous silicon quantum dots: the role of oxygen. *Phys. Rev. Lett.*, 82:197, 1999.

[28] A. S. Moskalenko, J. Berakdar, A. A. Prokofiev, and I. N. Yassievich. Single-particle states in spherical Si/SiO_2 quantum dots. *Phys. Rev. B*, 76:085427, 2007.

[29] N. B. Nguyen, C. Dufour, and S. Petit. Atomic and electronic structure of silicon nanocrystals embedded in a silica matrix. *J. Phys: Coondens. Matter*, 20:455209, 2008.

[30] A. J. Kenyon. Erbium in silicon. *Semicond. Sci. Tech.*, 20:R65, 2005.

[31] X. Zou and T. Izumitani. Spectroscopic properties and mechanisms of excited state absorption and energy transfer upconversion for Er^{3+}-doped glasses. *J. Non-Cryst. Solids*, 162:68, 1993.

[32] P. Urquhart. Review of rare earth doped fibre lasers and amplifiers. *IEE Proc. J*, 135:385, 1988.

[33] E. Desurvire, C.R. Giles, and J.R. Simpson. Gain saturation effects in high-speed, multichannel erbium-doped fiber amplifiers at lambda=1.53 μm. *J. Lightwave Technol*, 7:2095, 1989.

[34] M. Fukushima and J. Miura. Recent progress of erbium-doped fiber amplifiers and their components. *Proc. of SPIE*, 6775:677502, 2007.

[35] A J Kenyon, P F Trwoga, M Federighi, and C W Pitt. Optical properties of PECVD erbium-doped silicon-rich silica: evidence for energy transfer between silicon microclusters and erbium ions. *J. Phys.: Condens. Matter*, 6:L319, 1994.

[36] M. Fujii, M. Yoshida, Y. Kanzawa, S. Hayashi, and K. Yamamoto. 1.54 μ m photoluminescence of Er^{3+} doped into SiO_2 films containing Si nanocrystals: Evidence for energy transfer from Si nanocrystals to Er^{3+}. *App. Phys. Lett.*, 71:1198, 1997.

[37] J.H. Shin, Jinku Lee, Hak seung Han, Ji-Hong Jhe, Jee Soo Chang, Se-Young Seo, Hansuek Lee, and Namkyoo Park. Si nanocluster sensitization of Er-doped silica for optical amplet using top-pumping visible LEDs. *IEEE J. Sel. Top. Quant.*, 12:783, 2006.

[38] P. Pellegrino, B. Garrido, J. Arbiol, C. Garcia, Y. Lebour, and J. R. Morante. Site of Er ions in silica layers codoped with Si nanoclusters and Er. *App. Phys. Lett.*, 88:121915, 2006.

[39] G. Franzo, S. Boninelli, D. Pacifici, F. Priolo, F. Iacona, and C. Bongiorno. Sensitizing properties of amorphous Si clusters on the 1.54-μ m luminescence of Er in Si-rich SiO_2. *App. Phys. Lett*, 82:3871, 2003.

[40] Oleksandr Savchyn, Forrest R. Ruhge, Pieter G. Kik, Ravi M. Todi, Kevin R. Coffey, Haritha Nukala, and Helge Heinrich. Luminescence-center-mediated excitation as the dominant Er sensitization mechanism in Er-doped silicon-rich SiO_2 films. *Phys. Rev. B*, 76:195419, 2007.

[41] Oleksandr Savchyn, Pieter G. Kik, Ravi M. Todi, and Kevin R. Coffey. Effect of hydrogen passivation on luminescence-center-mediated Er excitation in Si-rich SiO_2 with and without Si nanocrystals. *Phys. Rev. B*, 77:205438, 2008.

[42] Oleksandr Savchyn, Ravi M. Todi, Kevin R. Coffey, and Pieter G. Kik. Multilevel sensitization of Er^{3+} in low-temperature-annealed silicon-rich SiO_2. *App. Phys. Lett.*, 93:233120, 2008.

[43] Oleksandr Savchyn, Ravi M. Todi, Kevin R. Coffey, Luis K. Ono, Beatriz Roldan Cuenya, and Pieter G. Kik. Excitation wavelength independent sensitized Er^{3+} concentration in as-deposited and low temperature annealed Si-rich SiO_2 films. *App. Phys. Lett*, 95:231109, 2009.

[44] Oleksandr Savchyn, Ravi M. Todi, Kevin R. Coffey, and Pieter G. Kik. Observation of temperature-independent internal Er^{3+} relaxation efficiency in Si-rich SiO_2 films. *App. Phys. Lett.*, 94:241115, 2009.

[45] Oleksandr Savchyn, Kevin R. Coffey, and Pieter G. Kik. Determination of optimum Si excess concentration in Er-doped Si-rich SiO_2 for optical amplification at 1.54 μ m. *App. Phys. Lett.*, 97:201107, 2010.

[46] F. Gourbilleau, C. Dufour, M. Levalois, J. Vicens, R. Rizk, C. Sada, F. Enrichi, and G. Battaglin. Room-temperature 1.54 μm photoluminescence from Er-doped Si-rich silica layers obtained by reactive magnetron sputtering. *J. App. Phys.*, 94:3869, 2003.

[47] F. Iacona, G. Franzo, M. Miritello, R. L. Savio, E. F. Pecora, A. Irrera, and F. Priolo. Er-based materials for Si microphotonics. *Opt. Mater.*, 31:1269, 2009.

[48] I. Izeddin, D. Timmerman, T. Gregorkiewicz, A. S. Moskalenko, A. A. Prokofiev, I. N. Yassievich, and M. Fujii. Energy transfer in Er-doped SiO_2 sensitized with Si nanocrystals. *Phys. Rev. B*, 78:035327, 2008.

[49] P. G. Kik, M. L. Brongersma, and A. Polman. Strong exciton-erbium coupling in Si nanocrystal-doped SiO_2. *App. Phys. Lett.*, 76:2325, 2000.

[50] A. Polman and F. C. J. M. van Veggel. Broadband sensitizers for erbium-doped planar optical amplifiers: review. *J. Opt. Soc. Am. B*, 21:871, 2004.

[51] D. Navarro-Urrios, A. Pitanti, N. Daldosso, F. Gourbilleau, R. Rizk, B. Garrido, and L. Pavesi. Energy transfer between amorphous Si nanoclusters and Er^{3+} ions in a SiO_2 matrix. *Phys. Rev. B*, 79:193312, 2009.

[52] D. L. Dexter. A theory of sensitized luminescence in solids. *J. Chem. Phys.*, 21:836, 1953.

[53] T. Förster. Zwischenmolekulare energiewanderung und fluoreszenz. *Ann. der Physik*, 437:55, 1948.

[54] Y. W. Lu, B. Julsgaard, M. C. Petersen, R. V. S. Jensen, T. G. Pedersen, K. Pedersen, B. B. Nielsen, and A. L. Nylandsted. Erbium diffusion in silicon dioxide. *App. Phys. Lett.*, 97:141903, 2010.

[55] Ji-Hong Jhe, Jung H. Shin, Kyung Joong Kim, and Dae Won Moon. The characteristic carrier–Er interaction distance in Er-doped a-Si/SiO_2 superlattices formed by ion sputtering. *App. Phys. Lett.*, 82:4489, 2003.

[56] S. Nunez-Sanchez, P. M. Roque, R. Serna, and A. K. Petford-Long. Si nanoparticle-Er^{3+} coupling through contact in as-deposited nanostructured films. *App. Phys. Lett.*, 98:151109, 2011.

[57] A. A. Prokofiev, A. S. Moskalenko, and I. N. Yassievich. Excitation of Er^{3+} ions in SiO_2 with Si nanocrystals. *Semiconductors*, 42:971, 2008.

[58] A. Jayraman, W. Klement, and G. C. Kennedy. Melting and polymorphism at high pressure in some group IV elements and III-V compounds with the diamond/zincblende structure. *Phys. Rev.*, 130:540, 1963.

[59] T. G. Pedersen, C. Fisker, and R. V. S. Jensen. Tight-binding parameterization of α-Sn quasiparticle band structure. *J. Phys. Chem. Solids*, 71:18, 2010.

[60] R. J. Walters, G. I. Bourianoff, and H. A. Atwater. Field-effect electroluminescence in silicon nanocrystals. *Nat. Mater.*, 4:143, 2005.

[61] L. Pavesi, L. Dal Negro, C. Mazzoleni, G. Franzo, and F. Priolo. Optical gain in silicon nanocrystals. *Nature*, 408:440, 2000.

[62] Victor I. Klimov. Mechanisms for photogeneration and recombination of multiexcitons in semiconductor nanocrystals: Implications for lasing and solar energy conversion. *J. Phys. Chem. B*, 110:16827, 2006.

[63] M. F. Fyhn, J. Chevallier, and A. Nylandsted Nielsen. α-Sn and β-Sn precipitates in annealed epitaxial $Si_{0.95}Sn_{0.05}$. *Phys. Rev. B*, 60:5770, 1999.

[64] I. Arslan, N. D. Browning T. J. V. Yates, and P. A. Midgley. Embedded nanostructures revealed in three dimensions. *Science*, 309:2195, 2005.

[65] R. Ragan and H. A. Atwater. Diamond cubic Sn-rich nanocrystals: synthesis, microstructure and optical properties. *App. Phys. A*, 80:1335, 2005.

[66] Y. Lei, P. Mock, T. Topuria, R. Ragan N. D. Browning, K. S. Min, and H. A. Atwater. Void-mediated formation of Sn quantum dots in a Si matrix. *Appl. Phys. Lett*, 82:4262, 2003.

[67] R. Ragan, K. S. Min, and H. A. Atwater. Direct energy gap group IV semiconductor alloys and quantum dot arrays in Sn_xGe_{1-x}/Ge and Sn_xSi_{1-x}/Si alloys systems. *Mater. Sci. Eng. B*, 87:204, 2001.

[68] C. Kittel. *Introduction to solid state physics.* Wiley, 2005.

[69] J. C. Slater and G. F. Koster. Simplified LCAO method for the periodic potential problem. *Phys. Rev.*, 94:1498, 1954.

[70] T. J. Lenosky, J. D. Kress, Inhee K., Arthur F. V., Byard E., David F. R., Sang Y., and James B. A. Highly optimized tight-binding model of silicon. *Phys. Rev. B*, 55:1528, 1997.

[71] T. G. Pedersen. *Electric, Optical and Magnetic properties of nanostructures.* Aalborg University, 2006.

[72] T. G. Pedersen, K. Pedersen, and T. B. Kristensen. Optical matrix elements in tight-binding calculations. *Phys. Rev. B*, 63:201101, 2001.

[73] A. H. Macdonald, S. H. Vosko, and P. T. Coleridge. Extension of the tetrahedron method for evaluating spectral properties of solids. *J. Phys. C: Solid State Phys.*, 12:2991, 1979.

[74] G. Gilat and N. R. Bharatiya. Tetrahedron method of zone integration: Inclusion of matrix elements. *Phys. Rev. B*, 12:3479, 1975.

[75] E. D. Palik. *Handbook of optical constants of solids.* Academic Press, 1985.

[76] P. Hohenberg and W. Kohn. Inhomogeneous electron gas. *Phys. Rev.*, 136:B864, 1964.

[77] W. Kohn and L. J. Sham. Self-consistent equations including exchange and correlation effects. *Phys. Rev.*, 140:A1133, 1965.

[78] L. J. Sham and M. Schlüter. Density-functional theory of the energy ap. *Phys. Rev. Lett.*, 51:1888, 1983.

[79] J. P. Perdew and M. Levy. Physical content of the exact Kohn-Sham orbital energies: band gaps and derivative discontinuities. *Phys. Rev. Lett.*, 51:1884, 1983.

[80] L. J. Sham and M. Schlüter. Density-functional theory of the band gap. *Phys. Rev. B*, 32:3883, 1985.

[81] L. Hedin. New method for calculating the one-particle Green's function with application to the electron-gas problem. *Phys. Rev.*, 139:A796, 1965.

[82] R. W. Godby and M. Schlüter. Accurate exchange-correlation potential for silicon and its discontinuity on addition of an electron. *Phys. Rev. Lett.*, 56:2415, 1986.

[83] M. S. Hybertsen and S. G. Louie. Theory and calculation of quasiparticle energies and band gaps. *Comments on Cond. Mat. Phys*, 13:223, 1987.

[84] M. Rohlfing, P. Krüger, and J. Pollman. Quasiparticle band-structure calculations for C, Si, Ge, GaAs, and SiC using Gaussian-orbital basis sets. *Phys. Rev. B*, 48:17791, 1993.

[85] A. B. Anderson. Vibrational potentials and structures in molecular and solid carbon, silicon, germanium, and tin. *J. Chem. Phys.*, 63:4430, 1975.

[86] C. Jo and K. Lee. Semiempirical tight binding method study of small Ge and Sn clusters. *J. Chem. Phys.*, 113:7268, 2000.

[87] C. Majumder, V. Kumar, H. Mizuseki, and Y. Kawazoe. Atomic and electronic structures of neutral and cation Sn_n (n=2-20) clusters: A comparative theoretical study with different exchange-correlation functionals. *Phys. Rev. B*, 71:035401, 2005.

[88] P. Moontragoon, N. Vukmirovic, Z. Ikonic, and P. Harrison. Electronic structure and optical properties of Sn and SnGe quantum dots. *J. App. Phys.*, 103:103712, 2008.

[89] P. Vogl, Harold P. Hjalmarson, and John D. Dow. A semi-empirical tight-binding theory of the electronic structure of semiconductors. *J. Phys. Chem. Solids*, 44:365, 1983.

[90] D. W. Jenkins and J. D. Dow. Electronic properties of metastable Ge_xSn_{1-x} alloys. *Phys. Rev. B*, 36:7994, 1987.

[91] B. Akdim, D. A. Papaconstantopoulos, and M. J. Mehl. Tight-binding description of the electronic structure and total energy of tin. *Phil. Mag. B*, 82:47, 2002.

[92] S Albrecht, L Reining, R D Sole, and G Onida. *Ab Initio* calculation of the excitonic effects in the optical spectra of semiconductors. *Phys. Rev. Lett.*, 80:4510, 1998.

[93] A Aguado. First-principles study of elastic properties and pressure-induced phase transitions of Sn: LDA versus GGA results. *Phys. Rev. B*, 67:212104, 2003.

[94] B H Cheong and K J Chang. First-principles study of the structural properties of Sn under pressure. *Phys. Rev. B*, 44:4103, 1991.

[95] P Pavone, S Baroni, and de S Gironcoli. $\alpha \leftrightarrow \beta$ phase transition in tin: A theoretical study based on density-functional perturbation theory. *Phys. Rev. B*, 57:10421, 1998.

[96] C Filippi, D J Singh, and C J Umrigar. All-electron local-density and generalized-gradient calculations of the structural properties of semiconductors. *Phys. Rev. B*, 50:14947, 1994.

[97] Y Juan and E Kaxiras. Application of gradient corrections to density-functional theory for atoms and solids. *Phys. Rev. B*, 48:14944, 1993.

[98] I Lee and R M Martin. Applications of the generalized-gradient approximation to atoms, clusters, and solids. *Phys. Rev. B*, 56:7197, 1997.

[99] L F Mattheiss and J R Patel. Electronic stacking-fault states in silicon. *Phys. Rev. B*, 23:5384, 1981.

[100] Jennifer L. Corkill and Marvin L. Cohen. Band gaps in some group-IV materials: A theoretical analysis. *Phys. Rev. B*, 47:10304, 1993.

[101] E. Snoeks, G. N. van den Hoven, and A. Polman. Optical doping of soda-lime glass with erbium by ion implantation. *J. App. Phys.*, 73:8179, 1993.

[102] A. Polman. Erbium implanted thin film photonic materials. *J. App. Phys.*, 82:1, 1997.

[103] I Y Kim, J H Shin, and K J Kim. Extending the nanocluster-si/erbium sensitization distance in er-doped silicon nitride: The role of Er-Er energy migration. *Appl. Phys. Lett.*, 95:221101, 2009.

[104] K Choy, F Lenz, X X Liang, F Marsiglio, and A Meldrum. Geometrical effects in the energy transfer mechanism for silicon nanocrystals and Er^{3+}. *App. Phys. Lett.*, 93:261109, 2008.

Appendix A

J. Phys. Chem. Solids, 71, 18 (2010)

Journal of Physics and Chemistry of Solids 71 (2010) 18–23

Contents lists available at ScienceDirect

Journal of Physics and Chemistry of Solids

journal homepage: www.elsevier.com/locate/jpcs

Tight-binding parameterization of α-Sn quasiparticle band structure

Thomas G. Pedersen *, Christian Fisker, Rasmus V.S. Jensen

Department of Physics and Nanotechnology, Aalborg University, DK-9220 Aalborg Øst, Denmark

ARTICLE INFO

Article history:
Received 20 April 2009
Received in revised form
26 August 2009
Accepted 4 October 2009

Keywords:
A: Semiconductors
A: Nanostructures
C: Ab initio calculations
D: Electronic structure
D: Optical properties

ABSTRACT

The diamond structure of tin (α-Sn) can be stabilized in nanocrystals embedded in a suitable host. We developed highly accurate parameterizations for tight-binding simulation of such structures incorporating strain and spin–orbit interaction. Parameters are obtained by fitting to *ab initio* GW quasiparticle band structures of unstrained α-Sn as well as geometries under uniform compressive or tensile strain. The optical response calculated from this fit is in excellent agreement with experiments. As an application, confinement induced band gaps in strained and unstrained 3 nm nanocrystals are computed. It is found that compressive and tensile strain raises and lowers the gap, respectively.

1. Introduction

Tin is iso-electronic with the important group IV semiconductors carbon, silicon and germanium but its properties differ significantly in several respects. Primarily, the stable crystal structure at room temperature and low pressure is the β-Sn form, which is a metallic body-centred tetragonal structure. The diamond structure α-Sn is stable only at lower temperatures [1]. Secondly, even in the α-Sn diamond structure, the material is a direct zero-gap semiconductor in contrast to the other group IV semiconductors that all possess finite indirect band gaps. Finally, Sn is a sufficiently heavy element that spin–orbit interaction (SOI) is a very significant perturbation. Due to these differences, Sn is usually not considered for semiconductor applications. However, α-Sn can be stabilized by embedding the material as nanoparticles in an appropriate host material such as Si [2–4] and Ge [5]. Apparently, tensile strain prevents the lattice from collapsing to the much denser β-Sn form. Moreover, in a nanoparticle, a finite energy gap develops as a result of confinement. Importantly, provided the α-Sn form remains stabilized, this gap can be tuned nearly all the way to zero by increasing the particle size since the bulk material has a vanishing gap. This opens the possibility of utilizing Sn in novel applications requiring small band gaps.

Compared to other group IV elements, the theoretical understanding of α-Sn is quite rudimentary. In particular, calculations of nanocrystal properties are very limited. Small clusters Sn_n with upper limits of n between 13 and 20 have been analyzed using a molecular orbital method [6], simple tight-binding (TB) [7] and *ab initio* methods [8]. The information on larger structures is limited, however, to a combined $\vec{k}\cdot\vec{p}$ and effective mass approach [9]. In addition, TB parameterizations of bulk bands exist [10–12]. The TB method is capable of accurately simulating the properties of nanocrystals containing thousands of atoms and to account for effects of surface termination. The existing parameterizations are not sufficiently accurate, however. The model of Ref. [7] uses universal Harrison parameters and overlap as well as SOI is neglected. In Ref. [10], a nearest-neighbor sp^3s^* parameterization ignoring overlap and SOI is used. The models of Refs. [11,12] are more realistic in that Ref. [11] includes SOI (but ignores overlap) whereas Ref. [12] includes overlap (but ignores SOI). Both of these fits fail to produce the correct behavior of the lowest conduction band along the important $\Gamma\rightarrow X$ direction, though, as is evident from their comparison with pseudopotential [11] and density-functional theory (DFT) [12] band structures. Moreover, none of the existing parameterizations incorporate strain. In the present work, we provide an improved tight-binding parameterization suitable for α-Sn nanoparticles including the effects of uniform strain and spin–orbit interaction. The parameterization is based on fits of *ab initio* band structures for crystal structures in the equilibrium geometry and under uniform strain, i.e. for lattices uniformly compressed or expanded. Consequently, the present model is limited to simulating nanoparticles under hydrostatic strain by the host material and does not apply to e.g. particles under orthorhombic strain.

A difficulty in this approach is that DFT is unable to account for the zero-gap character of α-Sn and incorrectly predicts a metallic band structure [13,14]. This deficiency can be remedied by incorporating quasiparticle effects, however. Rohlfing et al. [14]

* Corresponding author.
E-mail address: tgp@nano.aau.dk (T.G. Pedersen).

0022-3697/$ - see front matter © 2009 Elsevier Ltd. All rights reserved.
doi:10.1016/j.jpcs.2009.10.002

found that quasiparticle corrections within the GW approximation restores the zero-gap character by shifting the conduction bands upwards at the L point of the Brillouin zone while leaving the Γ point essentially unchanged. This is in marked contrast to the usual trend that GW corrections tend to shift all conduction bands upwards rigidly [15]. Accordingly, in the present work, GW corrected band structures are applied in the fitting procedure. As an application of this parameterization, we compute the density of states of 3 nm α-Sn nanoparticles in the equilibrium geometry and under strain emulating the influence of the host material.

2. Tight-binding parameterization

It is essential that accurate band structures are applied in the parameterization of TB parameters. In the present work, GW corrected bands are therefore computed using the *ab initio* code Abinit [16] within the GW extension [17,18]. A dense $8\times8\times8$ Monkhorst–Pack lattice of k-points is applied for all calculations. As a first step, DFT band structures in the local density approximation with and without SOI were obtained. In both cases, the Teter–Pade parameterization of exchange-correlation terms [19] was applied and for bands without SOI we used Troullier–Martins pseudopotentials [20] whereas SOI corrected bands were computed using Hartwigsen–Goedecker–Hutter pseudopotentials [21]. The latter has previously been successfully applied for the description of SOI-split bands in β-Sn [22]. The theoretical equilibrium geometry is obtained using DFT including SOI and setting the plane-wave energy cut-off to 15 Ha. The calculated total energy vs. lattice constant for α-Sn is shown in Fig. 1 together with a quadratic fit to the data points near equilibrium. We find an equilibrium lattice constant of a_0=12.11 Bohr. In addition, the fitted curvature 0.02065 Ha/Bohr^2 corresponds to a bulk modulus of B=0.02065 $(8/9a_0)$=1.52 mHa/Bohr^3=45 GPa. Both lattice constant and Bulk modulus are in reasonable agreement with the experimental values. The experimental lattice constant at 250 K and 90 K are 6.489 Å and 6.483 Å [23], respectively, and extrapolate to a 0 K value of 12.24 Bohr. The theoretical bulk modulus is to be compared to the experimental value of 54 GPa [24]. Hence, both lattice constant and bulk modulus are slightly underestimated theoretically. This level of agreement is reasonable considering the incorrect metallic state predicted by DFT near the equilibrium. To eliminate errors related to the incorrect geometry, however, we will use the equilibrium lattice constant a=12.23 Bohr obtained using a linearized augmented plane-wave approach to DFT by Akdim et al. [12] in excellent agreement with experiment. In addition, we consider α-Sn under 5% compressive strain (a=11.62 Bohr) as well as 5% tensile strain (a=12.84 Bohr), as indicated in Fig. 1. These strains are much larger than the experimental values (<0.5 % tensile [2]) but were selected in order to clearly expose the influence of lattice deformation. Also, an arbitrary strain in the -5–5% range may be studied using simple quadratic interpolation based on the parameters derived for these three cases.

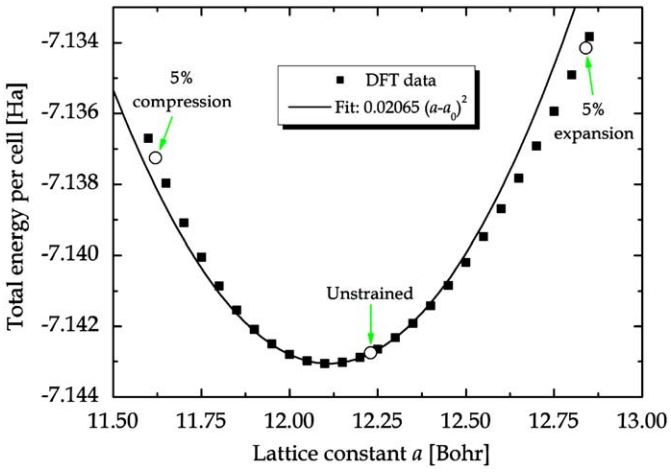

Fig. 1. Total DFT energy vs. lattice constant a and a quadratic fit to the central data points. Tight-binding parameterizations are found for the points indicated by circles.

In *Abinit*, the GW extension takes as input the self-consistent DFT bands and wave functions. This information is applied to construct the susceptibility matrix using the random phase approximation and, subsequently, the dielectric and self-energy matrices. To this end, the frequency dependence is simplified using the single plasmon-pole approximation [17]. We use the DFT settings above but lower the plane wave cut-off to 8 Ha due to computational limitations (see also [18]). The GW extension is not capable of handling SOI and an approximate procedure is therefore required. For clarity, we will refer to density functional band structures with and without SOI as DFT(SO+) and DFT(SO$-$), respectively. Hence, due to the aforementioned limitations in the Abinit code, we compute the GW corrections based on DFT(SO$-$) bands. Subsequently, the GW *corrections* for each DFT(SO$-$) band are transferred to each corresponding DFT(SO+) band. Essentially this means, that SOI-split DFT(SO+) bands are shifted by an approximate amount computed from their degenerated DFT(SO$-$) counterpart. It is this approximate GW corrected DFT(SO+) band structure, which we denote GW(SO+) below, that we finally use as input for TB fitting. Recently, a similar approach based on TB fitting of Abinit GW bands was applied to Si, Ge and SiGe [25].

It is known that the sp^3 TB parameterization of Mattheiss and Patel [26] including interactions up to third nearest neighbors and nonorthogonality of atomic orbitals provides a highly accurate fit of the silicon band structure. For this reason, a similar model will be adopted in the present work. In addition, our TB parameterization includes atomic SOI factors $\Delta=\langle 5p_x,\uparrow|H_{SO}|5p_z,\downarrow\rangle = i\langle 5p_x,\uparrow|H_{SO}|5p_y,\uparrow\rangle$ as introduced in the usual prescription [11]. Hence, 27 parameters need to be fitted: SOI constant Δ and onsite energies E_s and E_p as well as Hamilton (energy) matrix elements $H_{ss\sigma}$, $H_{sp\sigma}$, $H_{pp\sigma}$, $H_{pp\pi}$ and overlap elements $S_{ss\sigma}$, $S_{sp\sigma}$, $S_{pp\sigma}$, $S_{pp\pi}$ for first, second and third nearest neighbors. The fits are obtained by minimizing the mean square difference between TB and GW band structures for 13 selected k-points along the $\Gamma\rightarrow L$ and $\Gamma\rightarrow X$ directions in the Brillouin zone, cf. Figs 2 and 3. Also, we restrict fitting to the important bands 2 through 5 when counted from below. These bands are the ones responsible for behavior in the vicinity of the Fermi-level and, hence, to a large extent determine the band gap properties. For strained and unstrained geometries, the fitted parameters are given in Table 1.

In the unstrained case, our DFT(SO$-$) results predict a metallic band structure with the L_{6c} energy 0.09 eV lower than the Γ_{7c} point. With the GW correction, an upwards shift of the L_{6c} point with respect to Γ_{7c} by 0.33 eV restores the zero-gap structure, in good agreement with the 0.3 eV shift found by Rohlfing et al. [14]. At 5% compressive strain, α-Sn develops an indirect band gap with the top of the valence band in the zone centre and the conduction band minimum displaced approximately 85% along the $\Gamma\rightarrow X$ direction, similar to the case of unstrained Si. Within DFT(SO$-$), an indirect band gap of 0.25 eV is obtained. In addition, the indirect L–Γ gap is 0.63 eV. Hence, compressed α-Sn is a narrow indirect gap semiconductor. Finally, the expanded lattice leads to a metallic DFT(SO$-$) band structure as illustrated in the upper panel of Fig. 2. The L–Γ gap is only $\div$0.06 eV, however.

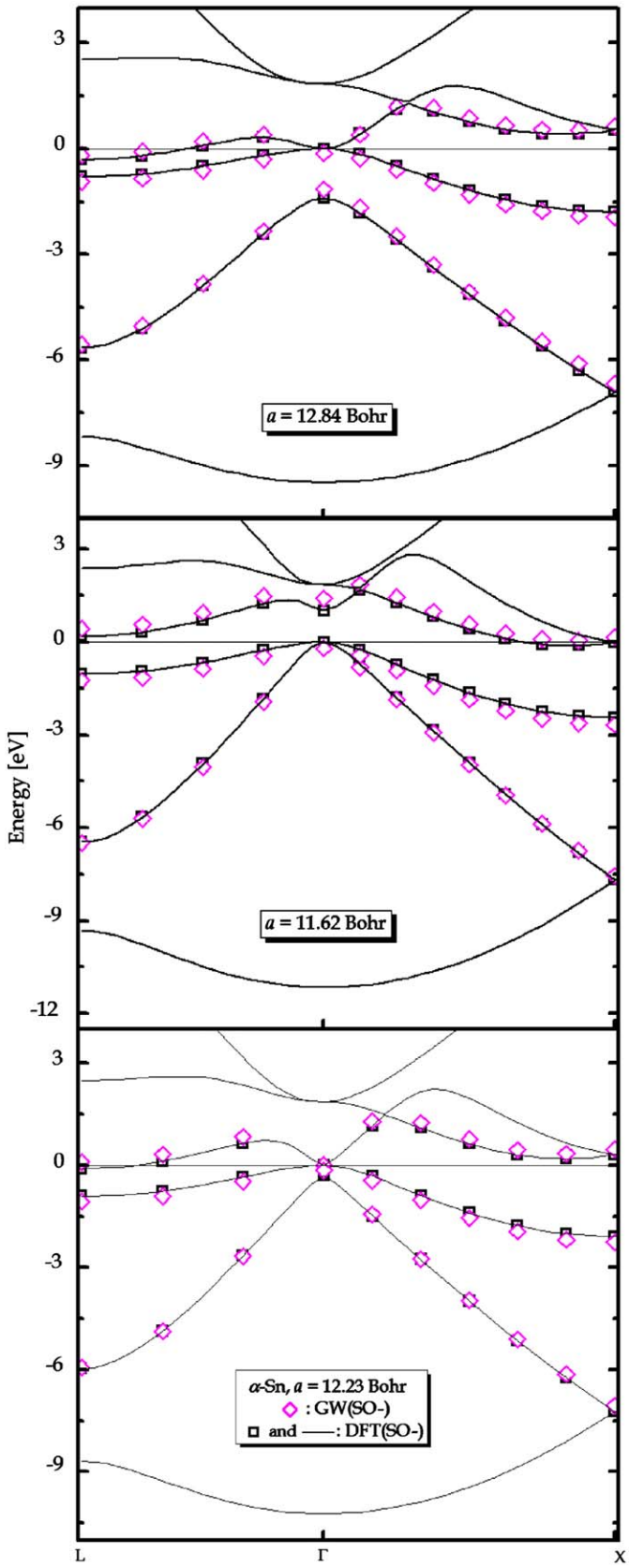

Fig. 2. Comparison between GW (diamonds) and DFT (squares and lines) bands without SOI. The panels illustrate cases without strain (bottom), and under compressive strain (middle) and tensile strain (top), respectively, with a the corresponding lattice constants.

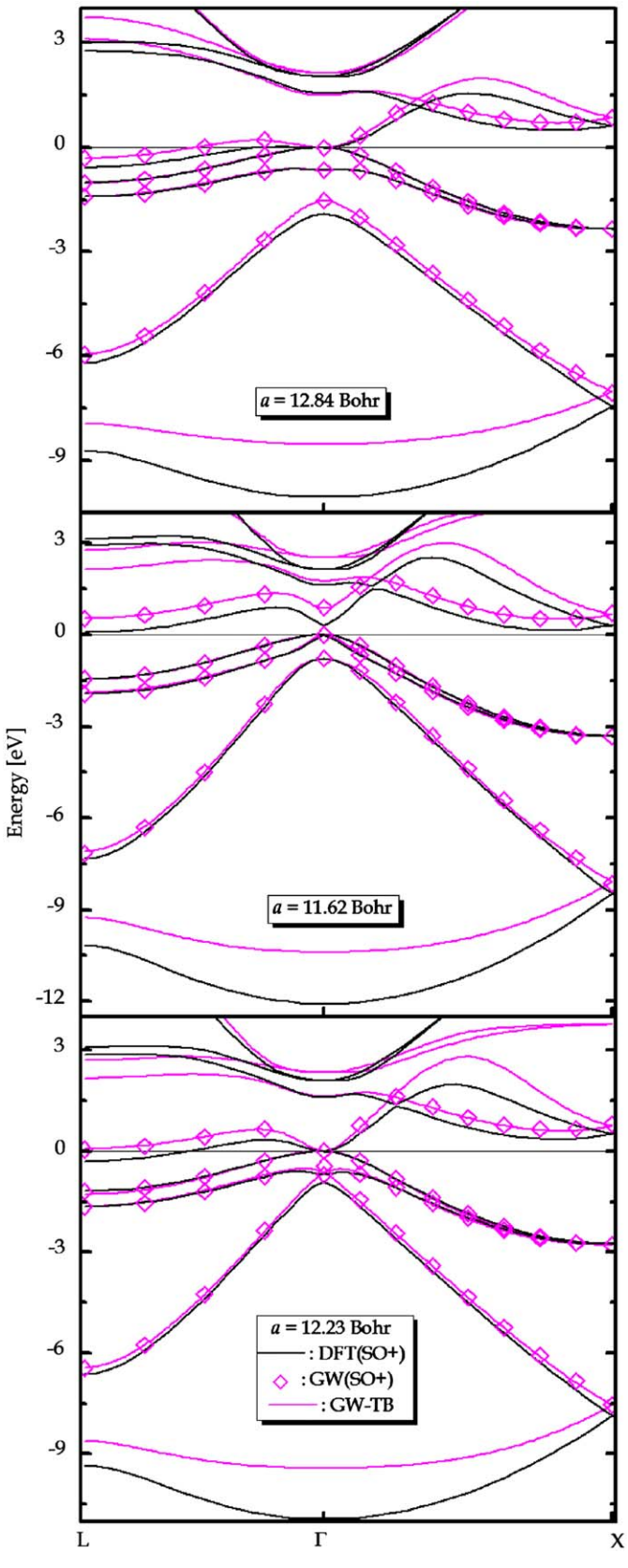

Fig. 3. GW corrected TB and uncorrected DFT band structures including SOI for strained and unstrained lattices.

Table 1
Tight-binding parameters for the nonorthogonal sp^3 model including SOI and interactions up to 3 nearest neighbors.

TB parameters a=12.84 Bohr				
Onsite	E_s=−7.5098 eV		E_p=−1.3709 eV	
SOI	Δ=0.1705 eV			
Overlap	$S_{ss\sigma}$	$S_{sp\sigma}$	$S_{pp\sigma}$	$S_{pp\pi}$
1. nn	0.2579	−0.3366	−0.2969	0.2135
2. nn	0.0276	−0.0416	−0.1055	0.0260
3. nn	0.0067	−0.0075	−0.0406	0.0000
Energy [eV]	$H_{ss\sigma}$	$H_{sp\sigma}$	$H_{pp\sigma}$	$H_{pp\pi}$
1. nn	−2.4072	2.4153	1.6590	−0.8136
2. nn	−0.2769	0.4436	0.6805	−0.1018
3. nn	−0.0689	0.1182	0.2444	−0.0216
TB parameters a=11.62 Bohr				
Onsite	E_s=−7.2342 eV		E_p=−1.0007 eV	
SOI	Δ=0.1830 eV			
Overlap	$S_{ss\sigma}$	$S_{sp\sigma}$	$S_{pp\sigma}$	$S_{pp\pi}$
1. nn	0.2667	−0.3114	−0.2853	0.2105
2. nn	0.0252	−0.0380	−0.1115	0.0180
3. nn	0.0058	−0.0108	−0.0401	0.0000
Energy [eV]	$H_{ss\sigma}$	$H_{sp\sigma}$	$H_{pp\sigma}$	$H_{pp\pi}$
1. nn	−2.6245	2.6504	1.4926	−0.7877
2. nn	−0.3165	0.5596	0.8047	−0.0816
3. nn	−0.0731	0.1285	0.2755	−0.0076
TB parameters a=12.23 Bohr				
Onsite	E_s=−7.1615 eV		E_p=−1.2060 eV	
SOI	Δ=0.1591 eV			
Overlap	$S_{ss\sigma}$	$S_{sp\sigma}$	$S_{pp\sigma}$	$S_{pp\pi}$
1. nn	0.2449	−0.3206	−0.2972	0.2101
2. nn	0.0270	−0.0367	−0.0975	0.0124
3. nn	0.0072	−0.0115	−0.0480	0.0000
Energy [eV]	$H_{ss\sigma}$	$H_{sp\sigma}$	$H_{pp\sigma}$	$H_{pp\pi}$
1. nn	−2.4025	2.5459	1.4457	−0.7349
2. nn	−0.2770	0.4863	0.7584	−0.0909
3. nn	−0.0731	0.1352	0.2452	−0.0215

In Fig. 3, the DFT(SO+) as well as our TB fits of the GW(SO+) bands are illustrated. The excellent agreement between GW points and fitted TB band structures is evident. The figure also clearly illustrates the pronounced split of the top valence bands resulting from the SOI correction. The conclusions regarding material characteristics (semiconducting vs. metallic, etc.) obtained without considering SOI remain valid. Hence, the unstrained structure remains a zero-gap semiconductor, while compressive strain produces a narrow indirect band gap of 0.5 eV, i.e. an additional opening of 0.25 eV compared to the DFT(SO−) value. Finally, the metallic character under tensile strain is now enhanced with a negative L–Γ gap of $\div$0.31 eV. The total densities of states (DOS) for the GW–TB bands, obtained through tetrahedron integration, are compared in Fig. 4. It is clear that all three structures display very similar trends in the vicinity of the Fermi level. Even in the metallic (a=12.84 Bohr) case, the DOS is only 0.05 eV^{-1} $cell^{-1}$ at the Fermi level. The top valence band DOS increases systematically with lattice constant while the DOS of the lowest conduction band is only slightly affected.

The accuracy of the parameterization is best checked by comparison with experiments. A sensitive test is the optical response because any error in the band structure will reveal itself if critical points or band splittings are compared. The experimental dielectric constant of unstrained α-Sn in the photon energy range 1.2–5.5 eV measured by Viña, Höchst and Cardona [27] is applied to this end. Besides the band structure, the momentum matrix elements are needed for the computation of the dielectric constant. We adopt the method of Ref. [28] for this purpose and, thus, separate the matrix element into intra- and inter-atomic contributions. The latter is entirely determined by the band structure and the lattice geometry. In contrast, the intra-atomic term requires fitting of an atomic transition momentum value $p_{sp}=\langle 5s,\uparrow|\partial/\partial x|5p_x,\uparrow\rangle\hbar^2/m$. We fit this parameter such that theoretical and experimental spectra agree

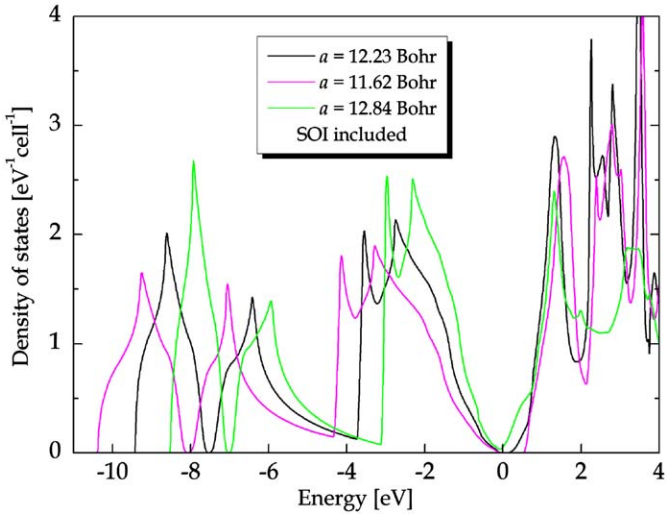

Fig. 4. Density of states for different lattice constants a computed from TB parameterizations including SOI and strain.

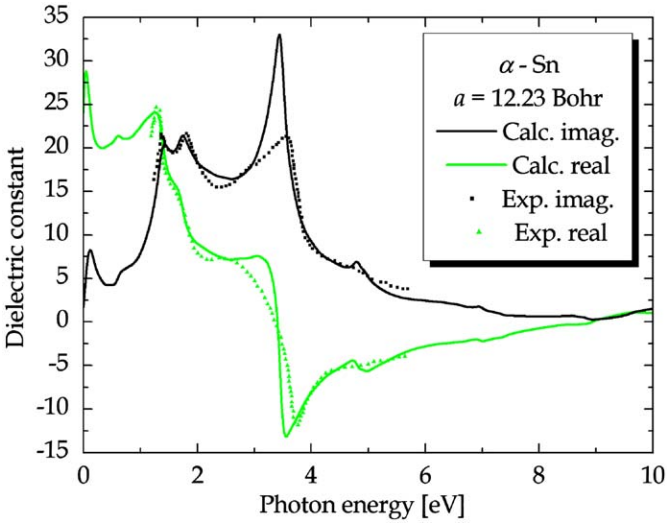

Fig. 5. Comparison between calculated (solid lines) and experimental (dots, Ref. [27]) dielectric constants.

in the low photon energy range. In this manner, the value p_{sp}=3.2 eVÅ is found. Theoretical spectra are computed using tetrahedron integration and convolution with a Gaussian line shape function $\exp(-E^2/\Gamma^2)/\Gamma\sqrt{\pi}$ with Γ=60 meV. The calculated and experimental results in the full range are compared in Fig. 5. It is clear that excellent agreement is obtained. The locations of the E_1 (1.35 eV) and $E_1+\Delta$ (1.8 eV) peaks that are produced mainly by transitions in the vicinity of the L point of the Brillouin zone are reproduced with very high accuracy. The E_2 resonance, which is dominated by transitions near the X point, is slightly redshifted in the calculations (3.4 eV) compared to measurements (3.7 eV). In addition, the intensity of this transition is overestimated. The overall agreement in the range for which experimental data exist is rather convincing, however. We take this as further evidence that our GW–TB parameterization produces reliable band structure predictions.

3. Application to 3 nm nanocrystals

A primary purpose of developing an accurate TB parameterization is to provide a tool for simulation of α-Sn nanostructures. The

systematic application of the parameterization to α-Sn nanocrystals will be presented elsewhere and in the present work we restrict ourselves to a single illustrative example. To this end, an $Sn_{633}H_{300}$ nanocrystal with and without strain is considered. This structure has a core diameter between 32 Å and 35 Å dependent on the strain. Thus, it is in the range of realistic geometries for experiments. The geometry of the Sn core is constructed simply as a spherical section of the bulk diamond lattice. Thus, relaxation of the nanoparticle geometry is not taken into account. Moreover, faceting is typically observed in experimental samples. In general, small nanoparticles may be severely affected by reconstruction [8] whereas the bulk crystal symmetry is approximately preserved in the core of larger ones [2,5]. Also, sufficiently large particles are found to be roughly spherical [5]. Hence, to estimate the influence of strain on energy gaps in nanoparticles we believe the simple geometry is adequate. We emphasize that the large strains of ±5% are outside the realistic range but, similar to the bulk case, were chosen in order to clearly display the effect of strain. More realistic strains can be studied, however, using a simple quadratic interpolation of all parameters in Table 1. Thus, if the values of a given parameter f at 0, +5%, −5% strain are denoted as f_0, f_+ and f_-, respectively, an interpolated value is readily obtained from the expression

$$f(\varepsilon) \approx f_0 + \frac{f_+ - f_-}{2}\frac{\varepsilon}{\varepsilon_0} + \frac{f_+ + f_- - 2f_0}{2}\left(\frac{\varepsilon}{\varepsilon_0}\right)^2,$$

where $\varepsilon=(a-a_0)/a_0$ is an arbitrary strain in the range $\pm\varepsilon_0$ with ε_0=5% and a_0=12.23 Bohr.

The H-termination is an artificial means of eliminating dangling surface bonds in order to remove such states from the band gap, as described in Ref. [29]. These pseudo H-atoms are modeled as a single *s*-type orbital with zero onsite energy and H–Sn interaction parameters $H_{ss\sigma}=-4$eV and $H_{sp\sigma}=4$ eV and non-orthogonality neglected. They are positioned along the directions of the dangling bonds. In Fig. 6, the DOS of strained and unstrained nanocrystals are displayed. The curves have been smoothed by a Gaussian with Γ=50 meV. In all cases, a confinement induced band gap appears. The gaps, calculated from the un-smoothed DOS, are: 0.95 eV (a=12.23 Bohr), 1.42 eV (a=11.62 Bohr) and 0.45 eV (a=12.84 Bohr). Thus, the induced band gap tends to follow the lattice constant systematically, with a large gap for compressed lattices. Under tensile strain, an isolated state approximately 0.31 eV below the practically continuous conduction band DOS brings about the substantially lower band gap. Hence, in the absence of this isolated state, the nanocrystal under tensile strain would enlarge its gap to 0.76 eV, still significantly below the other cases. Experimentally, the realistic scenario is that embedded nanocrystals are under slight tensile strain ($<0.5\%$) by the host lattice [2]. Hence, the present results predict that such particles in the 3–4 nm diameter range will exhibit band gaps in the order of 1 eV. Realistically, then, nanocrystals ranging from a few to a dozen nm in diameter will produce band gaps in the ∼0.1–1 eV range of great practical interest for e.g. solar cells.

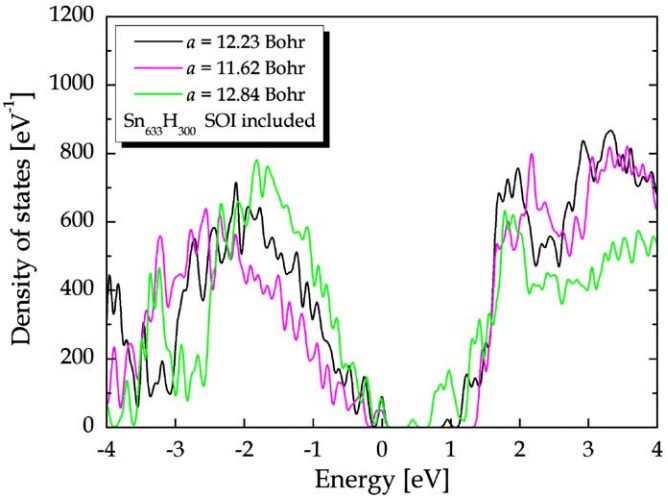

Fig. 6. Smoothed density of states computed for H-terminated α-Sn nanocrystals with and without strain indicated by the lattice constant a.

4. Summary

In summary, *ab initio* GW quasiparticle band structures have been applied to provide an accurate tight-binding parameterization for α-Sn. Unstrained structures as well as lattices uniformly compressed or expanded have been considered and separate parameterizations are presented. Moreover, spin–orbit interaction is included in the tight-binding model. Unstrained α-Sn and geometries under 5% compressive or tensile strain are found to be zero-gap semiconducting, narrow indirect gap semiconducting and weakly metallic, respectively. The quality of the parameterization is demonstrated by the excellent agreement between calculated and measured dielectric constants. The properties of 3 nm nanocrystals have been simulated using the new parameterizations. We find that unstrained nanocrystals exhibit band gaps of nearly 1 eV whereas 5% compressive or tensile strain leads to a substantial raising or lowering of the energy gap, respectively.

Acknowledgement

Financial support from FTP grant #274-07-0523 project SERBINA is gratefully acknowledged. Computations were carried out at the Fyrkat grid, Aalborg University.

References

[1] A. Jayaraman, W. Klement, G.C. Kennedy, Phys. Rev. 130 (1963) 540.
[2] M.F. Fyhn, J. Chevallier, A. Nylandsted Larsen, R. Feidenhans'l, M. Seibt, Phys. Rev. B60 (1999) 5770.
[3] Y. Lei, P. Möck, T. Topuria, N.D. Browning, R. Ragan, K.S. Min, H.A. Atwater, Appl. Phys. Lett. 82 (2003) 4262.
[4] I. Arslan, T.J.V. Yates, N.D. Browning, P.A. Midgley, Science 309 (2005) 2195.
[5] R. Ragan, H.A. Atwater, Appl. Phys. A 80 (2005) 1335.
[6] A.B. Anderson, J. Chem. Phys. 63 (1975) 4430.
[7] C. Jo, K. Lee, J. Chem. Phys. 113 (2000) 7268.
[8] C. Majumder, V. Kumar, M. Mizuseki, Y. Kawazoe, Phys. Rev. B64 (2001) 233405; C. Majumder, V. Kumar, M. Mizuseki, Y. Kawazoe, Phys. Rev. B71 (2005) 035401.
[9] P. Moontragoon, N. Vukmirovic, Z. Ikonic, P. Harrison, J. Appl. Phys. 103 (2008) 103712.
[10] P. Vogl, H.P. Hjalmarson, J.D. Dow, J. Phys. Chem. Solids 44 (1983) 365.
[11] D.W. Jenkins, J.D. Dow, Phys. Rev. B36 (1987) 7994.
[12] B. Akdim, D.A. Papaconstantopoulos, M.J. Mehl, Phil. Mag. B. 82 (2002) 47.
[13] T. Brudevoll, D.S. Citrin, M. Cardona, N.E. Christensen, Phys. Rev. B48 (1993) 8629.
[14] M. Rohlfing, P. Krüger, J. Pollmann, Phys. Rev. B57 (1998) 6485.
[15] M. Rohlfing, P. Krüger, J. Pollmann, Phys. Rev. B48 (1993) 17791.
[16] X. Gonze, J.-M. Beuken, R. Caracas, F. Detraux, M. Fuchs, G.-M. Rignanese, L. Sindic, M. Verstraete, G. Zerah, F. Jollet, M. Torrent, A. Roy, M. Mikami, Ph. Ghosez, J.-Y. Raty, D.C. Allan, Comput. Mater. Sci. 25 (2002) 478.
[17] X. Gonze, G.-M. Rignanese, M. Verstraete, J.-M. Beuken, Y. Pouillon, R. Caracas, F. Jollet, M. Torrent, G. Zerah, M. Mikami, Ph. Ghosez, Veithen M., J.-Y. Raty, V. Olevano, F. Bruneval, L. Reining, R. Godby, G. Onida, D.R. Hamann, D.C. Allan, Zeit. Kristallogr. 220 (2005) 558.
[18] The following Abinit settings were used: ecut=8.0 Ha, ecutwfn(screening)=3.6 Ha, ecuteps=6.0 Ha, ecutwfn(GW)=5.0 Ha, ppmfrq=16.7 eV.
[19] S. Goedecker, M. Teter, J. Hutter, Phys. Rev. B54 (1996) 1703.

[20] N. Troullier, J.L. Martins, Phys. Rev. B43 (1991) 1993.
[21] C. Hartwigsen, S. Goedecker, J. Hutter, Phys. Rev. B58 (1998) 3641.
[22] T.G. Pedersen, P. Modak, K. Pedersen, N.E. Christensen, M.M. Kjeldsen, A. Nylandsted Larsen, J. Phys.: Condens. Matter 21 (2009) 115502.
[23] D.L. Price, J.M. Rowe, Solid State Commun. 7 (1969) 1433.
[24] C.J. Buchenauer, M. Cardona, F.H. Pollak, Phys. Rev. B3 (1971) 1243.
[25] Y.M. Niquet, D. Rideau, C. Tavernier, H. Jaouen, X. Blase, Phys. Rev. B79 (2009) 245201.
[26] L.F. Mattheiss, J.R. Patel, Phys. Rev. B23 (1981) 5384.
[27] L. Viña, H. Höchst, M. Cardona, Phys. Rev. B31 (1985) 958.
[28] T.G. Pedersen, K. Pedersen, T.B. Kristensen, Phys. Rev. B63 (2001) 201101.
[29] M.P. Persson, H.Q. Xu, Appl. Phys. Lett. 81 (2002) 1309.

Appendix B

J. Phys.: Condens. Matter, 23, 345501 (2011)

J. Phys.: Condens. Matter **23** (2011) 345501 (7pp) doi:10.1088/0953-8984/23/34/345501

Quasiparticle electronic and optical properties of the Si–Sn system

Rasmus V S Jensen[1], **Thomas G Pedersen**[1] **and Arne N Larsen**[2]

[1] Department of Physics and Nanotechnology, Aalborg University, 9220 Aalborg Øst, Denmark
[2] Department of Physics and Astronomy, Aarhus University, 8000 Aarhus C, Denmark

E-mail: tgp@nano.aau.dk

Received 20 May 2011, in final form 14 July 2011
Published 12 August 2011
Online at stacks.iop.org/JPhysCM/23/345501

Abstract
The $Si_{1-x}Sn_x$ material system is an interesting candidate for an optically active material compatible with Si. Based on density functional theory with quasiparticle corrections we calculate the electronic band structure of zinc-blende SiSn under both compressive and tensile strain. At 2.2% tensile strain the band gap becomes direct with a magnitude of 0.85 eV. We develop an accurate tight-binding parameterization of the electronic structure and calculate the optical properties of SiSn. Furthermore, the silicide $SiSn_2$ is investigated and found to have metallic character.

(Some figures in this article are in colour only in the electronic version)

1. Introduction

An ongoing, intense field of research is the search for optoelectronic structures that can be integrated with silicon technology. The indirect band gap of silicon, however, does not directly facilitate the production of light emitting or absorbing devices. A host of different approaches have been taken to overcome this inherent shortcoming of silicon, notably including the use of quantum confined silicon structures [1] and the growth of III–V overlayers via buffer layers [2]. These have only seen limited success in a commercial sense, however. A promising option is the use of group IV binary or ternary overlayers with Sn which in sufficiently high concentrations gives rise to a direct band gap, owing to the direct zero-gap nature of bulk α-Sn. One of the simplest examples of such a system is $Si_{1-x}Sn_x$, which has been investigated both experimentally [3, 4] and theoretically [4–9]. In terms of theoretical approaches, predicted electronic structure and optical properties in the binary SiSn system have been calculated applying simple interpolation between band structures [5], empirical pseudopotentials [6, 7], optical bowing parameters [8], as well as local density approximation (LDA) density functional theory (DFT) [4, 9]. In order to assess the usefulness of SiSn in optoelectronic applications, accurate estimates of the band structure and optical spectra are necessary. Also, in such overlayer systems, strain is often present which to our knowledge has not been investigated in detail yet.

In this work we shall calculate the electronic properties of zinc-blende SiSn using DFT with quasiparticle self-energy corrections, in order to get a more accurate estimate of the band gap. The quasiparticle correction is analyzed using the *GW* approximation [10]. It is well established that DFT without quasiparticle corrections leads to a dramatic underestimation of the Si band gap [10] by roughly 50% and even fails to reproduce the zero-gap nature of α-Sn [11, 12]. Thus, such corrections are expected to be equally important for Si–Sn alloys. We subsequently fit sp^3 tight-binding parameters to the electronic band structures and calculate the optical spectra based on the obtained parameters. We will treat both bulk, unstrained SiSn as well as SiSn under both tensile and compressive uniform strain in particular with regards to the changes in the electronic structure. Due to the computational complexity of the *GW* method, we will not investigate cases of biaxial strain although such effects are probably important for layered samples grown on crystalline substrates. Finally, the possibility of mixed Si–Sn alloys forming Sn-rich structures is investigated via the electronic structure of the silicide $SiSn_2$ and whether it is likely to form locally.

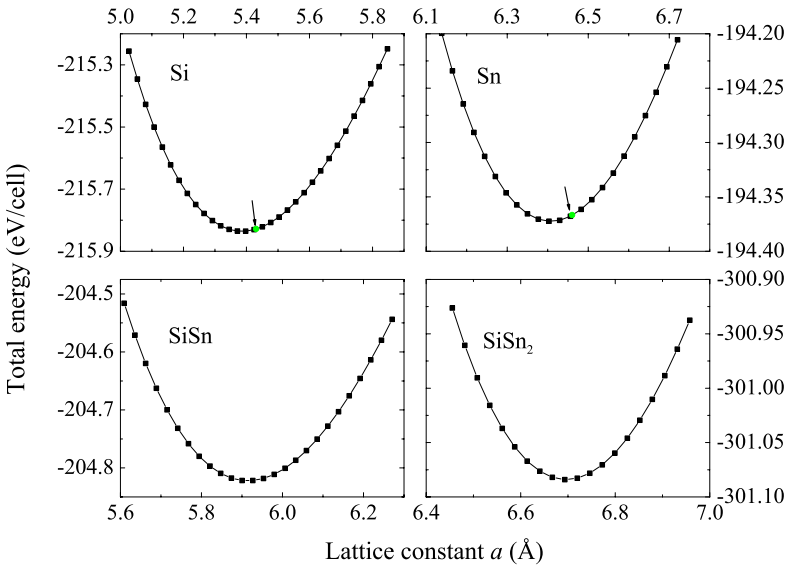

Figure 1. Total DFT energy versus lattice constant, a, as obtained for Si (top left), α-Sn (top right), SiSn (lower left) and $SiSn_2$ (lower right). Experimental lattice constants for Si and α-Sn are marked by a green point and an arrow.

2. Calculations

The electronic band structure was calculated on the basis of DFT, using the *ab initio* software package *Abinit* [13, 14]. As spin–orbit interaction (SOI) plays a large role in Sn [12, 15, 16], it is also expected to be significant in SiSn. It is currently not possible to include SOI in the *GW* calculation in *Abinit*, and so we instead calculate the band structure including SOI using the LDA and then correct this band structure with the shifts obtained from the *GW* calculation, similarly to the procedure applied in [12]. For all calculations, a dense $8\times8\times8$ Monkhorst–Pack grid of $\vec{k}$-points was applied as well as a plane wave energy cut-off of 14 Ha. Initially, a two-atom SiSn unit cell having zinc-blende symmetry was constructed and relaxed using Hartwigsen–Goedecker–Hutter pseudopotentials [17], the Teter–Pade exchange–correlation parameterization [18] and including SOI. A plot of the total DFT energy versus lattice constant is shown in figure 1. We find the lattice constant of SiSn to be $a_0 = 5.93$ Å, which, as expected, is in between the values found for bulk Si and α-Sn, 5.40 and 6.41 Å, respectively. This is in reasonable agreement with the experimental values of 5.43 and 6.49 Å, respectively, and in accordance with similar theoretical results and the general tendency of LDA to underestimate lattice constants [19]. Specifically, LDA values between 6.38 and 6.46 Å have been reported [20–22] for α-Sn, whereas the generalized gradient approximation (GGA) value is 6.74 Å [20]. For Si, typical values reported using LDA are between 5.37 and 5.41 Å [19, 23, 24].

In order to assess the stability of SiSn we compare the total energy per cell of the SiSn unit cell with the Si and α-Sn cells in table 1. As expected, SiSn is less energetically favourable than segregated, unstrained Si and Sn. However, the lattice mismatch between Si and Sn facilitates a strain energy comparable to the formation energy of SiSn. Thus, SiSn turns out to be a metastable phase, similarly to α-Sn at room temperature. We also investigate the silicide, $SiSn_2$, which is formed by a three-atom basis with Si at (0, 0, 0) and Sn at $\pm(\frac{1}{4}, \frac{1}{4}, \frac{1}{4})$ in an fcc lattice, as illustrated in figure 2. As per table 1, $SiSn_2$ may actually form more favourably than SiSn. It is clearly still unstable but under suitable conditions may be stabilized by strain similarly to SiSn. We are not aware of any reports of $SiSn_2$ bulk structures in the literature. This is in agreement with our finding that the structure is unstable and, furthermore, indicates that the material cannot easily be stabilized by strain.

Table 1. Calculation of total energy per cell in Si, α-Sn, SiSn and $SiSn_2$ along with the cost of formation per atom for SiSn and $SiSn_2$ relative to α-Sn and Si.

Compound	Energy/cell (eV)	Cost of formation/atom (eV)
Si	−215.84	0
α-Sn	−194.37	0
SiSn	−202.04	3.07
$SiSn_2$	−300.97	0.41

The LDA band structure was calculated for unstrained SiSn and under 5% tensile and compressive strain. While 5% strain is on the large side of what would usually be encountered under experimental conditions, this clearly elucidates the influence at strain on the electronic properties. Furthermore, from the tight-binding fits, parameters for smaller strains can be obtained by a quadratic interpolation of the three obtained parameter sets. After this, we calculated the *GW* corrections in the different strain configurations using Troullier–Martins pseudopotentials [25] and Teter–Pade exchange–correlation terms. The DFT wavefunctions with the same parameters as above were used as input to the plasmon-pole dielectric matrix needed in the *GW* calculation.

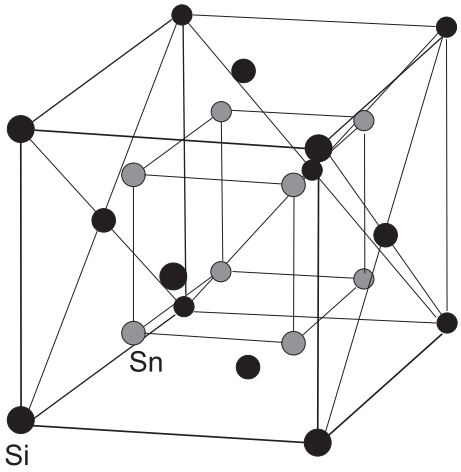

Figure 2. Illustration of the crystal structure of $SiSn_2$.

This dielectric function should not be confused with the optical dielectric constant computed in a separate calculation below. As mentioned, currently the *GW* calculation cannot be made including SOI in *Abinit*. To compensate for this shortcoming, we correct the individual bands in our LDA band structures including SOI with the *GW* corrections for each band, to obtain the approximate, final band structures.

The *GW* corrected band structure is extremely accurate but also very computationally demanding. To enable calculations of densities of states and response functions that require dense $\vec{k}$-point sampling to reach convergence, we therefore use tight-binding models to fit the bands. Below, these fits are subsequently used to compute the optical response using a very dense sampling of the irreducible Brillouin zone (BZ), which is partitioned into 12 288 tetrahedra. Moreover, such fits could be useful in simulations of various SiSn nanostructures. For the tight-binding (TB) parameterization, we have chosen an sp^3 basis, which includes up to third nearest neighbour interaction, non-orthogonal atomic orbitals and SOI. Such a basis has proven successful both in accurate descriptions of the Si [26] and α-Sn [12] band structures and we expect it to yield an accurate fit to the SiSn band structure. This leaves us with 41 unique parameters to fit, the SOI constant Δ, onsite elements E_s and E_p, and Hamilton matrix elements $H_{ss\sigma}$, $H_{sp\sigma}$, $H_{pp\sigma}$, $H_{pp\pi}$ along with overlap elements $S_{ss\sigma}$, $S_{sp\sigma}$, $S_{pp\sigma}$, $S_{pp\pi}$ for the first, second and third nearest neighbours, for both Si and Sn. The constants are fitted by minimizing the mean square difference in band energy values between the *GW* corrected band structure and the calculated TB band structure at 23 $\vec{k}$-points along the $X \rightarrow \Gamma \rightarrow L$ path in the BZ. The obtained TB parameters may be seen in tables A.1–A.3 and the TB band structures as well as the DFT band structures are shown in figure 3. In these plots, we have illustrated the DFT and TB band structures along the $L \rightarrow \Gamma \rightarrow X \rightarrow U \rightarrow \Gamma$ route in $\vec{k}$-space in order to assess how well the TB parameters reproduce the band structure outside their fitted interval. Even outside the fitted range, valence band fits remain excellent and only the higher

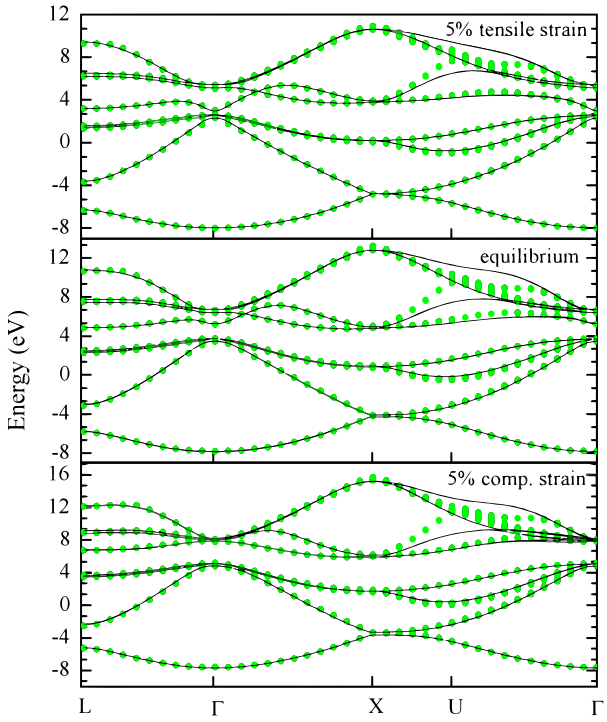

Figure 3. Calculated DFT band structure with *GW* corrections (points) and TB fits (lines). The top panel illustrates the case under tensile strain, the middle in equilibrium and the bottom under compressive strain.

conduction bands have some inaccuracies. This will, however, only have an effect on the high-energy part of the optical spectra and therefore is acceptable.

For the unstrained SiSn we predict an indirect band gap of 0.97 eV across the $\Gamma \rightarrow X$ transition, which is in good agreement with the indirect gap of 0.91 eV reported for SiSn by [6], using empirical pseudopotentials. We find a $\Gamma_v \rightarrow \Gamma_c$ gap of 1.48 eV, in contrast to the 1.14 eV reported using empirical pseudopotentials. In [4] a random alloy of $Si_{0.50}Sn_{0.50}$ was modelled using DFT with an empirical correction to the band gap. In this case a band gap of 0.8 eV was identified. We attribute this significantly lower band gap to more 'α-Sn'-like phases in the unit cell, which will pull it towards a direct gap, semi-metallic character like that found in bulk α-Sn. Under compressive strain, the indirect band gap decreases slightly to 0.75 eV, but the $\Gamma \rightarrow \Gamma$ gap increases to 2.72 eV. This is a dramatic strain effect, as is also seen in α-Sn [12]. Under 5% tensile strain the band gap shifts to become direct and is found to be 0.46 eV. This shifting towards a more direct band gap is also reported by [6] and [9]. In order to further investigate this shift from indirect to direct gap we perform new *GW* corrected band structure calculations for SiSn under tensile strains of 1–5%. From these we extract the energy gap across the first Γ–L, Γ–Γ and Γ–X transitions, as shown in figure 4. As can be seen, around 2.2% tensile strain, the band gap becomes a direct one as a consequence of the applied strain. This effect becomes more pronounced as the strain is increased, due to the steeper

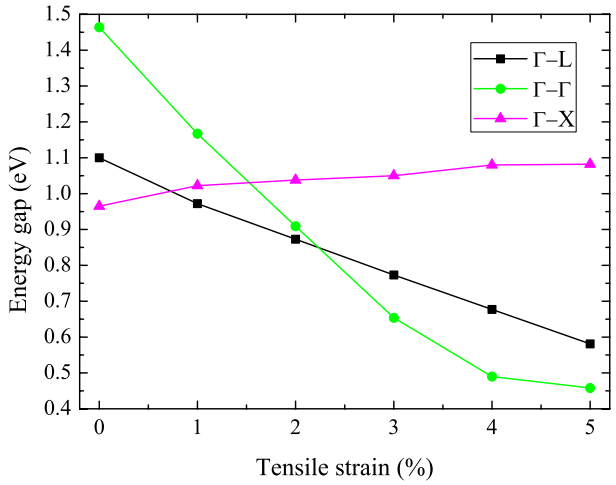

Figure 4. Calculated energy gaps of the Γ–L, Γ–Γ and Γ–X transitions in SiSn for varying degrees of tensile strain, marked by the points. The line serves as a guide to the eye.

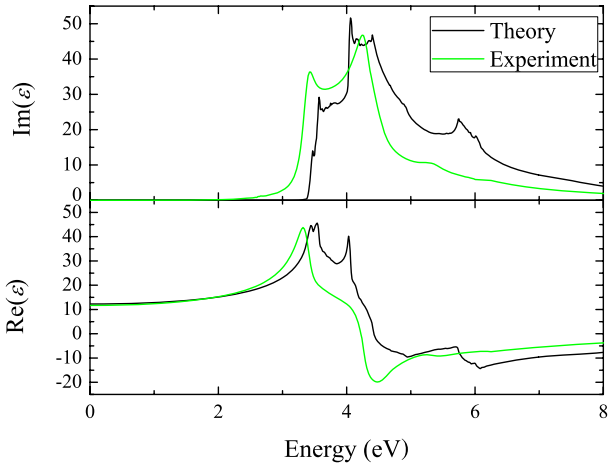

Figure 6. Calculated optical spectra of Si and comparison with experimental values, taken from [29].

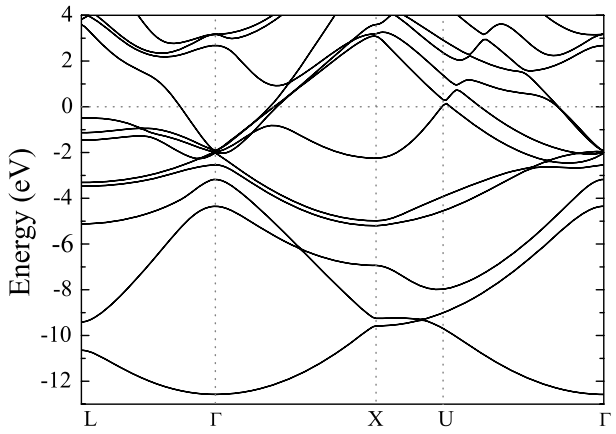

Figure 5. DFT band structure of $SiSn_2$, with the Fermi level at 0 eV, marked by the dotted line.

slope of the Γ–Γ curve as compared to the Γ–L curve. This effect is also observed in other group IV semiconductors and is in good agreement with the findings in [9], except that we report slightly higher band gap values, due to the more accurate estimate of the conduction bands in the *GW* corrected calculation. This also highlights the possibilities afforded through strain engineering of SiSn compounds.

The semiconducting nature of SiSn can be contrasted with the DFT band structure of $SiSn_2$, which is illustrated in figure 5. It is apparent that this structure has metallic characteristics that we ascribe to Sn being in a more β-like configuration. As the β-phase is the energetically more favourable one at room temperature, this would also explain the more favourable formation energy of $SiSn_2$ compared to SiSn. This low formation energy, however, comes at the cost of a large lattice mismatch with Si. The metallic nature of $SiSn_2$ could be detrimental to optoelectronic devices based on Si–Sn alloys with excess Sn.

Next, in order to investigate the properties of SiSn in optical applications, we calculate the dielectric constant of SiSn in both the strained and unstrained geometries, using the TB parameters to determine the band structure in the irreducible wedge of the BZ. For the calculation, we adopt the method in [27], where the contributions to the matrix element are split into intra- and inter-atomic terms. Whereas the latter is determined solely from the band structure and the lattice constant, the former requires fitting the momentum matrix element $p_{\mathrm{sp}} = \hbar^2/m\langle s|\partial/\partial x|p\rangle$ for transitions between atomic s and p orbitals. The $\vec{k}$-point integration over the BZ is carried out by summation over tetrahedra [28]. For α-Sn we adopt the value $p_{\mathrm{sp,Sn}} = 3.2$ eV Å from [12], however we have no readily available value for Si. To obtain the momentum matrix value for Si, we carry out the above mentioned calculation on bulk Si, using the TB parameters from [26], then calculating the optical spectra and fitting the momentum matrix element to the experimental values from [29] such that the low energy features are replicated. Based on this we arrive at $p_{\mathrm{sp,Si}} = 5.2$ eV Å. As illustrated in figure 6, the real part of the dielectric constant is then determined by Kramers–Krönig transformation of the imaginary part. In these spectra, excitonic effects are ignored and distinct features therefore simply reflect single-electron transitions. Hence, the observed peaks should not be associated with excitonic resonances but, rather, with intense transitions at band edges. Similarly, the discrepancy between calculated and experimental absorption edges near the direct band gap is partly due to omitted excitonic effects. Obviously, an improved spectrum including excitonic effects may be obtained by solving the Bethe–Salpeter equation, as has been done for Si and other materials [30, 31]. Given these shortcomings of the present model, however, the reproduction of the low energy part of the absorption spectrum is satisfactory in the sense that it replicates the important

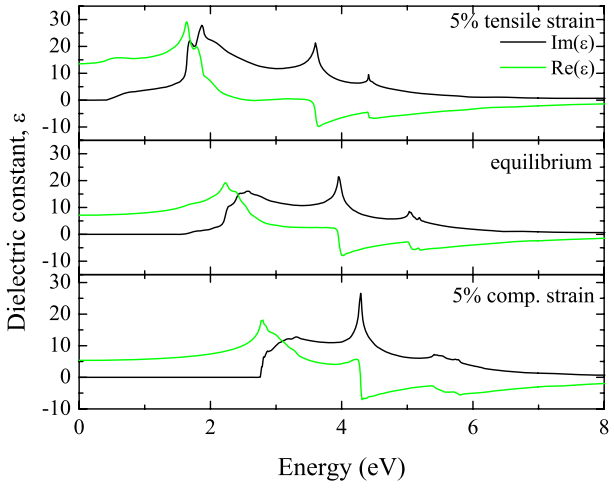

Figure 7. Calculated real and imaginary parts of the dielectric constants for SiSn. The top panel illustrates the case under tensile strain, the middle in equilibrium and the bottom under compressive strain.

features in the spectrum due to transitions near the band edges.

The optical spectra of SiSn may then be calculated following the same method. A plot of the dielectric constant for the strained and unstrained geometries is seen in figure 7. For the unstrained geometry, there is a slow onset of absorption at 1.48 eV, corresponding to the direct Γ–Γ transition, which is the lowest direct transition, as seen from figure 3. The rapid rise at 2.2 eV is due to the E_1 and $E_1 + \Delta$ transitions becoming available along the L region in the band structure. As expected, the compressed structure has an absorption onset at higher energies, however this rises very rapidly as there are a large number of available direct transitions at similar energies along the L → Γ path in the BZ. The structure under tensile strain starts absorbing at 0.45 eV corresponding to the direct gap at Γ found in this case.

3. Conclusion

We have calculated the electronic band structure of SiSn using DFT with *GW* correction in strained and unstrained geometries. In the unstrained case we find an indirect gap of 0.97 eV. Under tensile strain the band gap decreases and at 2.2% strain we find a transition to a direct band gap of 0.85 eV. On the other hand, compressive strain is found to increase the band gap. We then presented TB parameterizations to replicate the band structures. From the TB band structures we have calculated the dielectric constants for varying degrees of strain. Finally we investigated the silicide $SiSn_2$, which is found to show metallic character and have relatively low formation energy.

Acknowledgment

Financial support from FTP grant no. 274-07-0523, project SERBINA, is gratefully acknowledged.

Appendix. Tight-binding parameters

Table A.1. Tight-binding parameters for unstrained SiSn.

Tight-binding parameters, $a = 11.2$ Bohr				
SOI	$\Delta = 0.0707$ eV			
Onsite (eV)	$E_{s,Si} = -6.8506$	$E_{p,Si} = -0.9360$	$E_{s,Sn} = -7.2198$	$E_{p,Sn} = -0.8446$
Energy, Si (eV)	$H_{ss\sigma}$	$H_{sp\sigma}$	$H_{pp\sigma}$	$H_{pp\pi}$
(1) NN	−2.6557	2.7191	1.5158	−0.7672
(2) NN	−0.3067	0.5299	0.7937	−0.0960
(3) NN	−0.0725	0.1199	0.2632	−0.0133
Energy, Sn (eV)	$H_{ss\sigma}$	$H_{sp\sigma}$	$H_{pp\sigma}$	$H_{pp\pi}$
(1) NN	−2.6557	2.8244	1.5158	−0.7672
(2) NN	−0.3421	0.5870	0.8582	−0.0960
(3) NN	−0.0725	0.1793	0.2632	−0.0133
Overlap, Si	$S_{ss\sigma}$	$S_{sp\sigma}$	$S_{pp\sigma}$	$S_{pp\pi}$
(1) NN	0.2275	−0.2625	−0.3551	0.2337
(2) NN	0.0158	−0.0311	−0.0925	0.0223
(3) NN	0.0035	−0.0134	−0.0440	0.0000
Overlap, Sn	$S_{ss\sigma}$	$S_{sp\sigma}$	$S_{pp\sigma}$	$S_{pp\pi}$
(1) NN	0.2275	−0.2676	−0.3661	0.2337
(2) NN	0.0135	−0.0373	−0.1216	0.0167
(3) NN	0.0035	−0.0139	−0.0440	0.0000

Table A.2. Tight-binding parameters for SiSn under 5% tensile strain.

Tight-binding parameters, $a = 11.76$ Bohr				
SOI	$\Delta = 0.0720$ eV			
Onsite (eV)	$E_{s,Si} = -7.0198$	$E_{p,Si} = -1.0503$	$E_{s,Sn} = -7.3831$	$E_{p,Sn} = -0.9974$
Energy, Si (eV)	$H_{ss\sigma}$	$H_{sp\sigma}$	$H_{pp\sigma}$	$H_{pp\pi}$
(1) NN	−2.4303	2.5283	1.5697	−0.7564
(2) NN	−0.2025	0.4856	0.7469	−0.0698
(3) NN	−0.0636	0.1477	0.2624	−0.0141
Energy, Sn (eV)	$H_{ss\sigma}$	$H_{sp\sigma}$	$H_{pp\sigma}$	$H_{pp\pi}$
(1) NN	−2.4303	2.7767	1.5697	−0.7564
(2) NN	−0.3154	0.4725	0.7323	−0.1068
(3) NN	−0.0636	0.1131	0.2624	−0.0141
Overlap, Si	$S_{ss\sigma}$	$S_{sp\sigma}$	$S_{pp\sigma}$	$S_{pp\pi}$
(1) NN	0.2082	−0.2533	−0.3442	0.2260
(2) NN	0.0118	−0.0361	−0.1118	0.0158
(3) NN	0.0047	−0.0054	−0.0377	0.0000
Overlap, Sn	$S_{ss\sigma}$	$S_{sp\sigma}$	$S_{pp\sigma}$	$S_{pp\pi}$
(1) NN	0.2082	−0.2870	−0.3442	0.2260
(2) NN	0.0155	−0.0270	−0.0956	0.0233
(3) NN	0.0047	−0.0115	−0.0377	0.0000

Table A.3. Tight-binding parameters for SiSn under 5% compressive strain.

Tight-binding parameters, $a = 10.64$ Bohr				
SOI	$\Delta = 0.0761$ eV			
Onsite (eV)	$E_{s,Si} = -6.5077$	$E_{p,Si} = -0.7204$	$E_{s,Sn} = -7.4791$	$E_{p,Sn} = -0.9248$
Energy, Si (eV)	$H_{ss\sigma}$	$H_{sp\sigma}$	$H_{pp\sigma}$	$H_{pp\pi}$
(1) NN	−2.7651	3.2122	1.6350	−0.8385
(2) NN	−0.3085	0.6413	0.8675	−0.0895
(3) NN	−0.0570	0.1200	0.3004	−0.0057
Energy, Sn (eV)	$H_{ss\sigma}$	$H_{sp\sigma}$	$H_{pp\sigma}$	$H_{pp\pi}$
(1) NN	−2.7651	2.6199	1.6350	−0.8385
(2) NN	−0.3400	0.5725	1.0385	−0.1098
(3) NN	−0.0570	0.1417	0.3004	−0.0057
Overlap, Si	$S_{ss\sigma}$	$S_{sp\sigma}$	$S_{pp\sigma}$	$S_{pp\pi}$
(1) NN	0.2241	−0.2668	−0.3657	0.2303
(2) NN	0.0105	−0.0165	−0.0808	0.0189
(3) NN	0.0012	−0.0103	−0.0337	0.0000
Overlap, Sn	$S_{ss\sigma}$	$S_{sp\sigma}$	$S_{pp\sigma}$	$S_{pp\pi}$
(1) NN	0.2241	−0.2476	−0.3657	0.2303
(2) NN	0.0076	−0.0400	−0.1019	0.0141
(3) NN	0.0012	−0.0163	−0.0337	0.0000

References

[1] Zacharias M, Heitmann J, Scholz R, Kahler U, Schmidt M and Bläsing J 2002 *Appl. Phys. Lett.* **80** 661

[2] Fang A W, Park H, Cohen O, Jones R, Paniccia M J and Bowers J E 2006 *Opt. Express* **14** 9203

[3] Prasad K G, Kurup M B and Bhagawat A 1986 *Nucl. Instrum. Methods Phys. Res.* B **15** 698

[4] Tolle J, Chizmeshya A V G, Fang Y-Y, Kouvetakis J, D'Costa V R, Hu C-W, Menéndez J and Tsong I S T 2006 *Appl. Phys. Lett.* **89** 231924

[5] Soref R A and Perry C H 1990 *J. Appl. Phys.* **69** 539

[6] Amrane N, Abderrahmane S A and Aourag H 1995 *Infrared Phys. Technol.* **36** 843

[7] Zaoui A, Ferhat M, Certier M, Khelifa B and Aourag H 1996 *Infrared Phys. Technol.* **37** 483

[8] D'Costa V R, Cook C S, Menéndez J, Kovetakis J, Tolle J and Zollner S 2006 *Solid State Commun.* **138** 309

[9] Corkill J L and Cohen M L 1993 *Phys. Rev.* B **47** 10304

[10] Rohlfing M, Krüger P and Pollmann J 1993 *Phys. Rev.* B **48** 17791

[11] Rohlfing M, Krüger P and Pollmann J 1998 *Phys. Rev.* B **57** 6485
[12] Pedersen T G, Fisker C and Jensen R V S 2010 *J. Phys. Chem. Solids* **71** 18
[13] Gonze X *et al* 2009 *Comput. Phys. Commun.* **180** 2582
[14] Gonze X *et al* 2005 *Z. Kristallogr.* **220** 558
[15] Pedersen T G, Modak P, Pedersen K, Christensen N E, Kjeldsen M M and Larsen A N 2009 *J. Phys.: Condens. Matter.* **21** 115502
[16] Jensen R V S, Pedersen T G and Pedersen K 2011 *Phys. Status Solidi* c **8** 1002
[17] Hartwigsen C, Goedecker S and Hutter J 1998 *Phys. Rev.* B **58** 3641
[18] Goedecker S, Teter M and Hutter J 1996 *Phys. Rev.* B **54** 1703
[19] Filippi C, Singh D J and Umrigar C J 1994 *Phys. Rev.* B **50** 14947
[20] Aguado A 2003 *Phys. Rev.* B **67** 212104
[21] Cheong B H and Chang K J 1991 *Phys. Rev.* B **44** 4103
[22] Pavone P, Baroni S and de Gironcoli S 1998 *Phys. Rev.* B **57** 10421
[23] Juan Y and Kaxiras E 1993 *Phys. Rev.* B **48** 14944
[24] Lee I and Martin R M 1997 *Phys. Rev.* B **56** 7197
[25] Troullier N and Martins J L 1991 *Phys. Rev.* B **43** 1993
[26] Mattheiss L F and Patel J R 1981 *Phys. Rev.* B **23** 5384
[27] Pedersen T G, Pedersen K and Kristensen T B 2001 *Phys. Rev.* B **63** 201101
[28] Rath J and Freeman A J 1975 *Phys. Rev.* B **11** 2109
[29] Palik E D 1985 *Handbook of Optical Constants of Solids* (New York: Academic)
[30] Albrecht S, Reining L, Sole R D and Onida G 1998 *Phys. Rev. Lett.* **80** 4510
[31] Schmidt W G, Glutsch S, Hahn P H and Bechstedt F 2003 *Phys. Rev.* B **67** 085307

Appendix C

Phys. Stat. Sol. C, 8, 1002 (2011)

Phys. Status Solidi C **8**, No. 3, 1002–1005 (2011) / **DOI** 10.1002/pssc.201000397

physica status solidi c
www.pss-c.com
current topics in solid state physics

Optical properties and size/shape dependence of α-Sn nanocrystals by tight binding

Rasmus Vincentz S. Jensen*, Thomas Garm Pedersen, and Kjeld Pedersen

Department of Physics and Nanotechnology, Aalborg University, 9220 Aalborg Øst, Denmark

Received 6 June 2010, revised 29 October 2010, accepted 29 October 2010
Published online 2 February 2011

Keywords tight binding, Sn, nanocrystals, grey tin, group IV nanocrystals

* Corresponding author: e-mail rj@nano.aau.dk

The semiconducting diamond structure of α-Sn may be stabilized by embedding nanocrystals in a suitable host. Based on a very accurate tight binding parametrization we calculate electronic and optical properties of round, as well as faceted nanocrystals, under both no, tensile and compressive strain. Nanocrystals with radii up to 2.6 nm are treated and are found to cover an energy range starting at near-zero band gap energy, with both size and also strain playing a significant role in determining the electronic properties. The HOMO-LUMO optical transition is found to be strong even for larger crystals, making them an attractive candidate in many potential NIR applications. Furthermore, exciton effects are estimated for bulk and nanocrystals and are found to be weak.

1 Introduction Tin is, unlike the other highly important group IV semiconductors, a metal at standard laboratory conditions, where it is found in its β-form, with body-centered tetragonal structure. However, tin may be found in its α-form at lower temperatures [1], where it takes on diamond structure. Even in this form tin still differs from the other group IV semiconductors in that it is a direct zero gap material, in contrast to the finite indirect band gap nature of the group IV semiconductors. As such, bulk α-Sn is usually not considered for semiconductor applications, however, particles of α-Sn can be stabilized in a suitable matrix host, which has been demonstrated in both Si and Ge [2–5]. In these cases it is believed that the tensile strain from the matrix prevents the particles from collapsing to the denser β form. As the size of these particles enters the nano regime, a band gap opens as a consequence of quantum confinement effects. Due to the zero gap nature of the bulk form, this band gap may be tuned over a wide energy range and may be promising in small gap nanocrystal applications which have been previously unavailable to Si and Ge based devices due to the intrinsic lower limit of the band gap in nanocrystals of these elements. As such, applications may include NIR diodes [6], optical amplifiers [7], lasers and solar cells [8]. Just like Si and Ge, Sn may be readily used in CMOS processes. While the treatment of Ge and Si nanocrystals in the litterature is vast and carried out in many frameworks, the available litterature on α-Sn nanocrystals is similarly scarce and only structures up to 20 Sn atoms have been treated by molecular orbital [9], tight binding [10] and ab initio methods [11]. For larger structures, only a combined $\mathbf{k}\cdot\mathbf{p}$ and effective mass approach exists [12]. Tight-binding is a suitable method for accurately treating nanocrystals with thousands of atoms. Until recently, tight binding treatments of α-Sn have not included both spin-orbit interaction (SOI), which plays a large role in Sn, as well as overlap and strain parameters [13]. In order to fully realise the potential of α-Sn nanoparticles, we explore the size-dependence of the electronic and optical properties. Furthermore, we include uniformly strained and faceted nanocrystals in our analysis, as it is likely that this is the form that will be encountered in real applications [2,3]. We base our calculations on a previous tight-binding paramerization of α-Sn two-center interactions, including strain, SOI and quasi-particle effects in the

density functional theory framework [13]. This provides a very accurate description of the bulk band structure as well as showing excellent agreement with the bulk optical properties of α-Sn.

2 Electronic properties To initialize the nanocrystal geometry, we consider cutouts of the atom-centered diamond lattice, applying both a spherical cutout as well as an octaeder truncated by (111) facets. In addition, the surface is saturated with hydrogen in order to eliminate dangling bonds. Various faceted and round nanocrystals are illustrated in Fig. 1. We then use the sp^3 tight binding parameterization including up to third nearest neighbour interaction and SOI described in [13], which accurately describes the band structure in α-Sn, as shown in Fig. 2 along with the calculated absorption spectrum. The terminating H-atoms are treated as s-orbitals with zero onsite energy and H-Sn interaction parameters given by $H_{ss\sigma} = -4$ eV and $H_{sp\sigma} = 4$ eV, considering only the nearest neighbour interaction. Nanocrystals ranging from SnH_4 up to $Sn_{2317}H_{756}$ for round species and up to $Sn_{2293}H_{756}$ for faceted species are treated, corresponding to nanocrystal radii up to 2.65 nm, which covers what has been encountered so far in the laboratory regarding pure α-Sn nanocrystals [2]. Unstrained geometries are treated along with ones under 5% uniform tensile and compressive strain. Plots of the energy gap versus the nanocrystal radius are plotted in Fig. 3 for round crystals and faceted. The radii of the faceted nanocrystals were calculated according to the number of Sn atoms in an equivalent round nanocrystal as $r_{eff} = (\frac{3}{32\pi}a^3 N_{\mathrm{Sn}})^{\frac{1}{3}}$, with a the lattice constant and N_{Sn} the number of Sn atoms. The band gap for both faceted and round nanocrystals appear similar with regards to size and as such the band gap is believed to be predominantly size dependent, with both converging towards the bulk value of 0 eV for large, unstrained nanocrystals, as expected. The energy scale of the α-Sn nanocrystals, which to the best of our knowledge has not been specifically addressed before, covers a wide range of energies and in particular for strained nanocrystals an energy range (0.1-1 eV) that is normally not easily accesible to relatively small nanocrystals is opened up. Given good optical properties, α-Sn nanocrystals may see application for capturing IR radiation in both solar cells as well as detectors. Also we see that strain plays a fairly large role, with a 0.5 eV seperation between unstrained and tensile strained nanocrystals, making strain play a potentially very important role in real world applications.

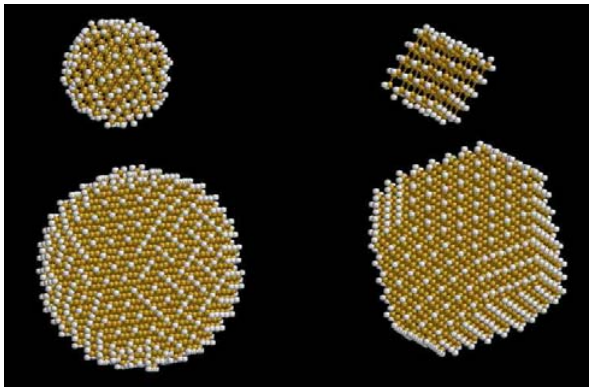

Figure 1 Illustration of round nanocrystals (left) and faceted nanocrystals (right), golden atoms are Sn and white surface atoms are hydrogen atoms, applied to eliminate dangling bonds.

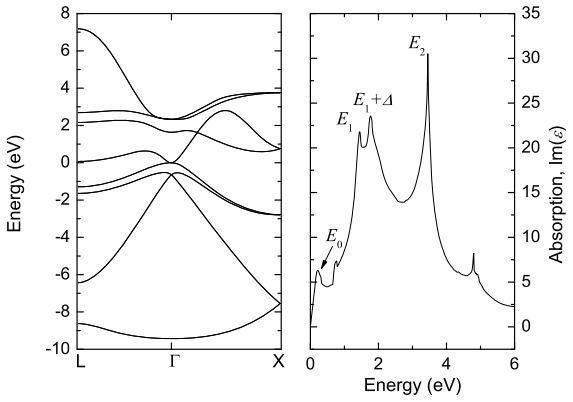

Figure 2 Calculated band structure of unstrained α-Sn (left) and absorption spectrum (right). Transitions arising from around the Γ point are marked with E_0, E_1 and $E_1 + \Delta$ are arising from mainly around the L-point, Δ being the SOI energy and E_2 transition being dominantly from around the X point.

3 Optical properties To obtain the optical properties of α-Sn nanocrystals, we apply the method in [14], which splits the contributions to the matrix elements into inter- and intra-atomic terms, in this the inter-atomic contribution is determined from the band structure while the intra-atomic term requires fitting an atomic momentum value. We adopt the value $p_{sp} = 3.2$ eVÅ from Ref. [13], which describes the optical properties in bulk α-Sn excellently. The imaginary parts of the dielectric constant of both large and small, round and faceted nanocrystals are plotted in Figs. 4 and 5 for round and faceted species, respectively and the bulk spectrum illustrated in Fig. 2. For larger nanocrystals in particular, both the E_0, E_1, $E_1 + \Delta$ and E_2 resonances arising from transitions near the Γ, X and L points in the bulk spectrum are reproduced in the nanocrystal spectra as well, which is expected as the size effects diminish and the nanocrystal start to take on more bulk-like character. We observe a distinct peak corresponding to the HOMO-LUMO E_0 transition at small energies, for both large and small large nanocrystals, which is stronger

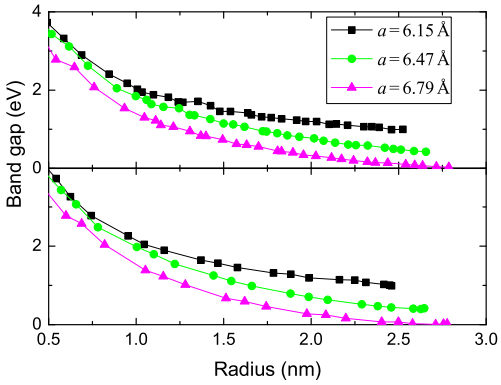

Figure 3 Band gap versus the radius of spherical α-Sn nanocrystals (top) and (111) faceted nanocrystals (bottom) in both unstrained ($a = 6.47$ Å) and strained geometries. Line serves as a guide to the eye only.

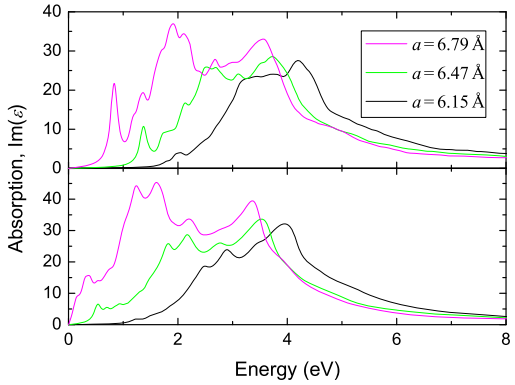

Figure 4 Imaginary part of the dielectric constant for round α-$Sn_{275}H_{172}$ (top) and α-$Sn_{1863}H_{605}$ (bottom) nanocrystals in unstrained ($a = 6.47$ Å) and strained geometries.

than the corresponding peak in the bulk spectrum and enhanced by decreasing size. This is contrary to, for instance, Si nanocrystals, where the nanocrystals exhibit some of the indirect band gap nature of the bulk [15,16] - the direct gap nature of α-Sn ensures good absorption characteristics even for larger sized nanocrystals. This is of utmost importance in applications where α-Sn nanocrystals are to be used as absorbers of low energy photons, for instance in photovoltaic applications. Observing the oscillator strength, it varies slightly, with the tensile strained being slightly (on the order of 10%) stronger, however most of the stronger absorption for tensile strained nanocrystals owe to the $1/E$ dependence of the absorption.

The optical spectra obtained above are calculated without considering exciton effects. In general, the Coulomb coupling between electrons and holes modfiies the spectra and may be of importance for optical applications. For instance, strong exciton binding is a severe obstacle to carrier separation in solar cells and photodetectors. Hence, a estimate of exciton binding is important. The scale of the binding energies is set by the effective Rydberg given by $Ry^* = 13.6\text{eV} \cdot \mu/\epsilon^2(0)$, where μ is the reduced effective electron-hole pair mass in units of the free-electron value m_0 and $\epsilon(0)$ is the static dielectric constant. Using experimental values [17,18] of the light electron mass $0.028m_0$ and heavy hole mass $0.195m_0$ we find $\mu = 0.024m_0$. For bulk and nanoparticle α-Sn, the dielectric screening $\epsilon(0)$ can be determined from the low frequency limit of the real part of the dielectric constant, which is found from a Kramers-Kronig transformation of the imaginary parts described above. In this manner, it is found that $\epsilon(0)$ is approximately 25 for unstrained bulk α-Sn and 12 and 82 under compressive and tensile strain, respectively. In fact, in the latter case, the material becomes metallic and, hence,

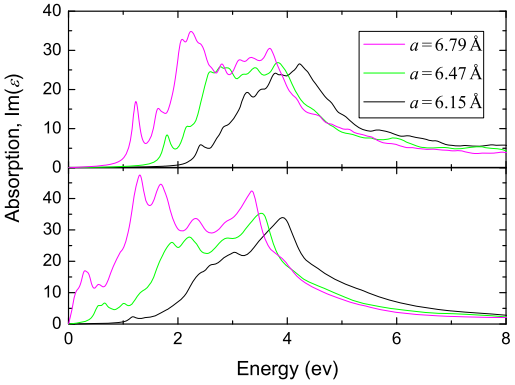

Figure 5 Imaginary part of the dielectric constant for faceted α-$Sn_{165}H_{100}$ (top) α-$Sn_{1669}H_{484}$ (bottom) nanocrystals in unstrained ($a = 6.47$ Å) and strained geometries.

additional intraband contributions to the screening should be considered. Moreover, at finite temperatures, even the unstrained zero-gap material supports intraband transitions due to the broadened Fermi distribution. In a simple parabolic band model, the squared plasma frequency $\omega^2_{p,metal}$ of a genuine metal at low temperature scales linearly with the electron density $n \propto E_F^{3/2}$, where E_F is the Fermi energy measured relative to the band edge. Conversely, for a parabolic zero-gap material with the Fermi level at the band edge a simple calculation, based e.g. on [19], shows that the squared plasma frequency $\omega^2_{p,zero-gap}$ varies as

$(k_BT)^{3/2}$. More precisely,

$$\frac{\omega^2_{p,zero-gap}}{\omega^2_{p,metal}} = 3\sqrt{\pi}\left(\frac{1}{2}-\frac{1}{2^{3/2}}\right)\zeta(3/2)\left(\frac{k_BT}{E_F}\right)^{3/2} \approx 2.03\left(\frac{k_BT}{E_F}\right)^{3/2},$$

where $\zeta(x)$ is the zeta function. Hence, intraband transitions in unstrained α-Sn are greatly suppressed compared to metallic (tensile strained) α-Sn. By ignoring intraband screening, an upper bound on the effective exciton Rydberg is found. Thus, in this manner we find bulk effective Rydbergs of 0.58 meV for unstrained material and 2.3 and 0.053 meV for crystals under compressive and tensile strain, respectively. These values will be further reduced by intraband screening and it follows that exciton effects are negligible at room temperature in bulk α-Sn. In the corresponding nanocrystals, however, size effects may substantially reduce screening. In order to evaluate the significance of this effect, we have calculated the electronic screening for various sizes of rounded nanocrystals as illustrated in Fig. 6. In these curves, the dependence on strain clearly agrees with the bulk cases, although the values for $a = 6.47$ Å and $a = 6.15$ Å appear to "'overshoot"' slightly before reaching the bulk values. This behavior is attributed to the simplistic method used to determine nanocrystal volume that ignores electron spill-out at the surface. Thus, for the unstrained nanocrystals the value of $\epsilon(0)$ reaches values slightly above the bulk value of 25. As expected, the screening diminishes in smaller nanocrystals, but even for nanocrystals in the 1 nm size range, the effective Rydberg does not exceed 5 meV, irrespective of strain. Thus, for nanoparticles embedded in a Si matrix (dielectric constant ≈ 12) exciton effects are not expected to be significant. It follows that electron-hole separation in α-Sn nanocrystals is unlikely to be seriously affected by exciton binding.

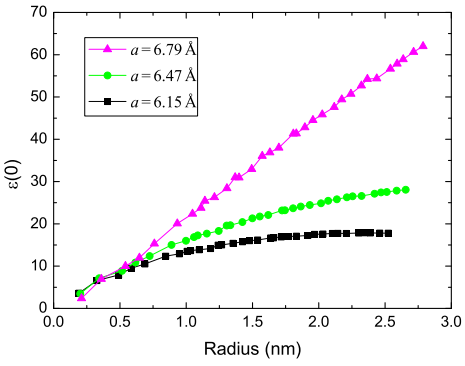

Figure 6 The electronic screening $\epsilon(0)$ versus nanocrystal radius for round α-Sn nanocrystals in unstrained ($a = 6.47$ Å) and strained geometries.

4 Conclusion Applying tight binding theory, we have calculated the electronic band gap of α-Sn nanocrystals, in both strained and unstrained geometries and for both round and faceted nanocrystals, saturated with hydrogen at the surface to passify dangling bonds. Nanocrystals with radii ranging up to 2.6 nm yield a widely tunable band gap, almost down to 0 eV, which may make α-Sn nanocrystals a promising candidate in many optoelectronic applications. Optical spectra were calculated and the lowest energy transition is found to be enhanced compared to bulk α-Sn. In both cases, the properties are mainly influenced by the size of the nanocrystal, with shape playing only a minor role. Exciton effects have also estimated and are believed to play only a minor role in α-Sn and nanocrystals.

Acknowledgements Financial support from FTP grant #274-07-0523, project SERBINA, is gratefully acknowledged.

References

[1] A. Jayraman, W. Klement, and G. C. Kennedy, Phys. Rev. **130**, 540 (1963).
[2] M. F. Fyhn, J. Chevallier, and A. N. Nielsen, Phys. Rev. B **60**, 5770 (1999).
[3] I. Arslan, N. D. B. T. J. V. Yates, and P. A. Midgley, Science **309**, 2195 (2005).
[4] R. Ragan and H. A. Atwater, Appl. Phys. A **80**, 1335 (2005).
[5] Y. Lei, P. Mock, T. Topuria, R. R. N. D. Browning, K. S. Min, and H. A. Atwater, Appl. Phys. Lett **82**, 4262 (2003).
[6] R. J. Walters, G. I. Bourianoff, and H. A. Atwater, Nature Mater. **4**, 143 (2005).
[7] L. Pavesi, L. Dal Negro, C. Mazzoleni, G. Franzo, and F. Priolo, Nature **408**, 440 (2000).
[8] V. I. Klimov, J. Phys. Chem. B **110**(August), 16827 (2006).
[9] A. B. Anderson, J. Chem. Phys **63**, 4430 (1975).
[10] C. Jo and K. Lee, J. Chem. Phys. **113**, 7268 (2000).
[11] C. Majumder, V. Kumar, H. Mizuseki, and Y. Kawazoe, Phys. Rev. B **71**, 035401 (2005).
[12] P. Moontragoon, N. Vukmirovic, Z. Ikonic, and P. Harrison, J. Appl. Phys **103**, 103712 (2008).
[13] T. G. Pedersen, C. Fisker, and R. V. S. Jensen, J. Phys. Chem. Solids **71**, 18 (2010).
[14] T. G. Pedersen, K. Pedersen, and T. B. Kristensen, Phys. Rev. B **63**, 201101 (2001).
[15] C. Delerue, G. Allan, and M. Lannoo, Phys. Rev. B **48**, 11024 (1993).
[16] D. Kovalev, H. Heckler, G. Polisski, and F. Koch, Phys. Status Solidi B **215**, 871.
[17] S. H. Groves, C. R. Pidgeon, A. W. Ewald, and J. Wagner, J. Phys. Chem. Solids **31**, 2031 (1970).
[18] T. Brudevoll, D. S. Citrin, M. Cardona, and N. E. Christensen, Phys. Rev. B **48**, 8629 (1993).
[19] T. G. Pedersen, M. Paritosh, K. Pedersen, N. E. Christensen, M. M. Kjeldsen, and A. N. Nielsen, J. Phys.: Condens. Matter **21**, 115502 (2009).

Appendix D

App. Phys. Lett, 97, 141903 (2010)

Erbium diffusion in silicon dioxide

Ying-Wei Lu,[1, a)] B. Julsgaard,[1] M. Christian Petersen,[1] R. V. Skougaard Jensen,[2] T. Garm Pedersen,[2, 3] K. Pedersen,[2, 3] and A. Nylandsted Larsen[1, 3]

[1)] *Department of Physics and Astronomy, Aarhus University, DK-8000 Aarhus C, Denmark*

[2)] *Department of Physics and Nanotechnology, Aalborg University, DK-9220 Aalborg Ø, Denmark*

[3)] *Interdisciplinary Nanoscience Center-iNANO, Denmark*

(Dated: 27 August 2010)

Erbium diffusion in silicon dioxide layers prepared by magnetron sputtering, chemical vapor deposition, and thermal growth has been investigated by secondary ion mass spectrometry, and diffusion coefficients have been extracted from simulations based on Fick's second law of diffusion. Erbium diffusion in magnetron sputtered silicon dioxide from buried Er distributions has in particular been studied, and in this case a simple Arrhenius law can describe the diffusivity with an activation energy of 5.3 ± 0.1 eV. Within a factor of two, the Er diffusion coefficients at a given temperature are identical for all investigated matrices.

Light emission from erbium ions (Er^{3+}) embedded in a silicon dioxide (SiO_2) matrix is one of the most important candidates for a light source for fiber-optic communication techniques since the emitted wavelength, at around 1.5 μm, corresponds to the minimum attenuation and dispersion in quartz optical fibers.[1] Moreover, the Er^{3+} emission has attracted intensive attention since it is remarkably enhanced by introducing some kind of sensitizer into the matrix, such as silicon nanocrystals (nc-Si).[2–5] This enhancement is believed to be due to an interaction between the Er^{3+} ions and a nc-Si following the *Förster* or *Dexter* mechanism.[6–9] The distance, x, between the Er^{3+} ions and the nc-Si must plays a key role for this coupling no matter which physical principle dominates since both mechanisms are distance-dependent: the interaction decreases with the distance as x^{-6} for the *Förster* mechanism, and as $\exp(-x/x_0)$ for the *Dexter* mechanism where x_0 is the characteristic interaction distance.[10]

In order to study this interaction mechanism it is of decisive importance to have well-defined separations between the Er^{3+} ions and the nc-Si. Well-defined nc-Si positions can be realized by employing multilayer structures even after heat treatment at the high forming temperature of nc-Si.[11–13] The high temperature, however, might result in Er diffusion in the SiO_2 matrix, and accordingly introduce confusion as to the exact interaction distance. To our knowledge there are no reports in the literature as to the diffusional behavior of Er in SiO_2. In previous studies Er precipitation in SiO_2 were demonstrated for temperatures above 1100 °C, however, these studies did not discuss the diffusional aspects of Er in SiO_2.[14,15] The aim of the present study is thus to explore the diffusional behavior of Er in SiO_2 matrices prepared in different ways: by magnetron sputtering, chemical vapor deposition (CVD), and thermal growth. Ideally, Er diffusion in the different types of SiO_2 matrices should have been studied from buried Er distributions in order to minimize the effects of the surface. This was, however, not possible for all the types of matrices. Instead, Er diffusion was thoroughly studied from a buried Er distribution in magnetron sputtered SiO_2, and the activation energy and pre-exponential factor determined. Diffusion coefficients determined for Er in-diffusion from a surface source into SiO_2 layers produced either by magnetron sputtering, CVD, or thermal growth were then compared to those determined from the buried distribution. In this way it has been possible to compare Er diffusion in the three different matrices.

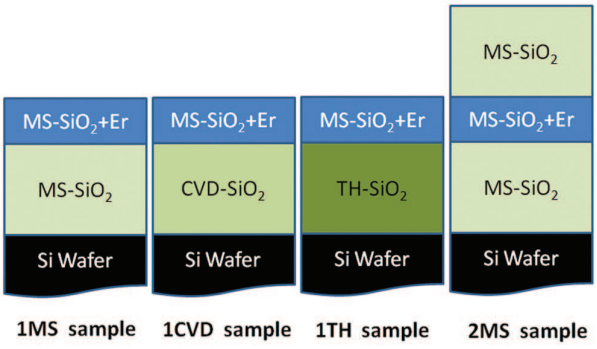

FIG. 1. (Color online) Sketches of film structures. The thicknesses of pure SiO_2 layers are 350 nm for magnetron sputtered SiO_2 and thermally grown SiO_2 layers, 220 nm for CVD grown SiO_2 layer, respectively. The thickness of SiO_2 containing Er layer is around 50 nm in all cases.

The three different types of pure SiO_2 layers were deposited on Si wafers by magnetron sputtering without substrate heating using a homemade system, by plasma enhanced CVD at 250 °C from a Surface Technology System (STS Multiplex CVD), and by thermal growth from a wet oxygen ambiance at 1100 °C. Accordingly, these samples are labeled 1MS, 1CVD, and 1TH, respectively. Subsequently, on top of these SiO_2 layers a SiO_2

[a)] Author to whom correspondence should be addressed. Electronic mail: luyw@phys.au.dk. Tel.: +45 89423746. FAX: +45 86120740.

layer containing Er with a concentration in the order of 0.2 *at.* % was deposited on each of them by magnetron sputtering at room temperature (the layer composition of these samples can be seen in Fig. 1). Then each sample was cut into several pieces and heated in N_2 at different temperatures ranging from 1000 to 1100 °C in steps of 25 °C. The duration of heat treatment were 6 hours for the 1000 °C heating and 4 hours for the other temperatures. At each temperature the three types of samples were put in the oven together which means that they were heat treated under exactly the same conditions. The sample with the buried Er distribution was prepared by magnetron sputtering at room temperature as a sandwich structure (see Fig. 1); this sample is labeled 2MS. It was also cut into several pieces, and heat treated in N_2 for 1.5 hours at different temperatures ranging from 1020 to 1100 °C in steps of 20 °C. The 1000 °C sample was heated for 7 hours.

The Er diffusion at a given temperature was investigated by measuring the Er concentration profiles before and after heat treatment using secondary ion mass spectrometry (SIMS) with a "TOF.SIMS^5" instrument based on time of flight.[16] Here, the analysis was accomplished in positive polarity using bismuth ions (Bi^+) at 25 keV rastering an area of $100\mu m \times 100\mu m$. Cesium ions (Cs^+) at 10 keV were used to sputter material away for depth profiling. In this way Er profiles as function of sputtering time are obtained. In order to convert the sputtering time to a depth scale in the SIMS profiles a Veeco Dektak 150 surface profiler was used to measure the depths of the craters (formed by the Cs^+ ions). This conversion is based on the assumption that the sputtering rate was constant during the whole SIMS measurement which is a reasonable assumption since all of the SIMS spectra were acquired in steady state conditions, and the Er concentration is too low to give rise to differences in the sputtering rate of a pure SiO_2 layer and a SiO_2 layer containing Er atoms.

To extract the diffusion coefficient, $D(T)$, as a function of temperature, T, the Er SIMS profile was compared for each sample to the profile of an as-deposited sample. The latter profile was convolved with the Gaussian function, $f(x) = A/(\sqrt{2\pi}\sigma)\exp(-x^2/2\sigma^2)$, and fitted to the former by χ^2-minimization. The convolution by the function, $f(x)$, resembles diffusion according to Fick's second law when $\sigma^2 = 2Dt$, where D is the diffusion coefficient and t is the duration of the heat treatment. The front factor, A, is of the order of unity and compensates for slightly different areas under the initial and final distributions.

The depth scale obtained by the surface profiler is estimated to be accurate within 2%, and before the fitting procedure the depth scale of the heat-treated profile was adjusted slightly in order to overlap its center to that of the as-deposited profile. This improves the accuracy and is justified since all samples originate from the same wafer and since the diffusion is symmetric for the 2MS samples.

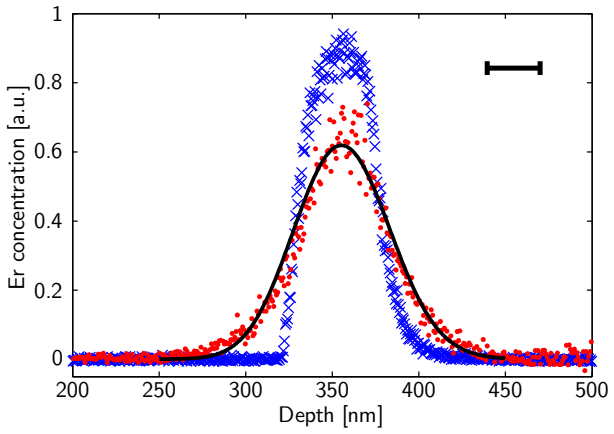

FIG. 2. (Color online) The Er SIMS profiles of the 2MS sample before (blue crosses) and after heat treatment at 1100 °C (red dots) together with the fitting result (black solid curve). The inserted scale bar of 31 nm is the corresponding diffusion length, $L = 2\sqrt{Dt}$.

Typical SIMS profiles of the 2MS sample before and after heat treatment at 1100 °C, and the fitted profile are shown in Fig. 2. It is clearly seen that the Er atoms have diffused from the initial layer into the pure SiO_2 layers on both sides of the Er distribution as a result of the heat treatment and that effects from the surface can be totally neglected. The diffusion coefficients are shown in Fig. 4 as black squares for all temperatures investigated. The error bars denote the statistical uncertainty from the fitting procedure. The data was fitted by the Arrhenius equation:

$$D(T) = D_{T_0} \exp\left[-\frac{\Delta E}{k_B} \times \left(\frac{1}{T} - \frac{1}{T_0}\right)\right], \qquad (1)$$

where k_B is the Boltzmann constant and T is the temperature of the heat treatment (in Kelvin). The activation energy was determined to be: $\Delta E = 5.3 \pm 0.1$ eV, and the pre-factor, $D_{T_0} = 1.76 \pm 0.08 \times 10^{-16}$ cm^2/s, denotes the value of the diffusion coefficient at a reference temperature, $T_0 = 1346$ K, chosen in order to minimize the correlation between the fitting parameters, D_{T_0} and ΔE. The 2% uncertainty of the absolute depth scale determination was included in the uncertainty estimate of D_{T_0}. Extrapolating to infinite temperature we obtain: $D(\infty) = 1.3 \pm 1.2 \times 10^4$ cm^2/s.

Figure 3 shows SIMS profiles of as-deposited and 1050 °C heat treated 1MS samples, and the fitting curve. As can be seen, a significant redistribution of the Er atoms takes place during the heat treatment. In the heat treated sample there is pile up of Er atoms at the surface, but it is outside the scope of this work to understand the details of surface effects, which are also left out in the fitting procedure. Instead we ensure that the beginning of the fitting range is always at least a diffusion length, $L = 2\sqrt{Dt}$, away for the region where surface effects are in play. In Fig. 3 the diffusion length is shown in the

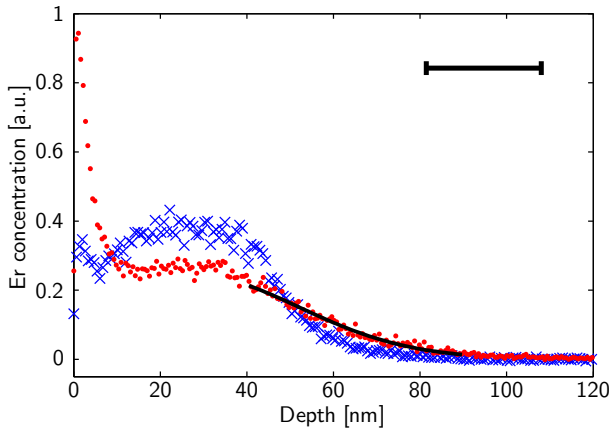

FIG. 3. (Color online) The Er SIMS profiles of the 1MS sample before (blue crosses) and after heat treatment at 1050 °C (red dots) together with the fitting curve (black solid curve). The inserted scale bar of 27 nm is the diffusion length of the heated sample.

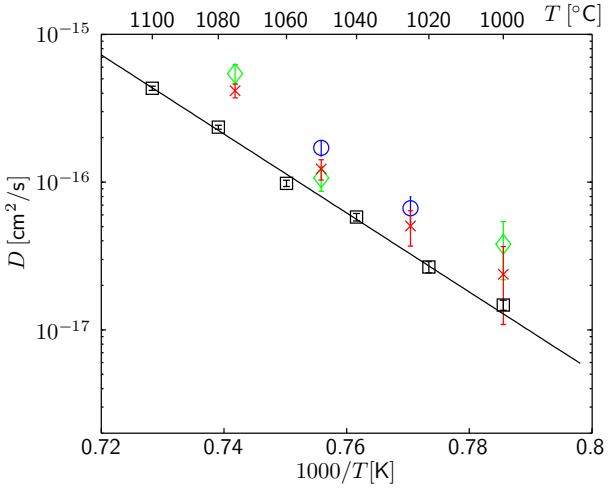

FIG. 4. (Color online) Temperature dependence of the diffusion coefficients of Er in thermally grown SiO_2 (blue circles), CVD grown SiO_2 (green diamonds), and magnetron sputtered SiO_2 (red crosses for 1MS samples, black squares for 2MS samples). The black straight line denotes Eq. (1) fitted to the data of the 2MS samples.

upper, right corner, and the range of the fitting curve is restricted accordingly.

Diffusion coefficients for several temperatures have been added in Fig. 4 for the 1MS, 1CVD, and 1TH samples. The error bars include both statistical errors from the fitting procedure and the absolute depth scale uncertainty. For the highest temperatures it turned out that a consistent fitting range could not be found and data for these temperatures were not included in Fig. 4. Two more data points (1025 °C of the 1CVD sample and 1000 °C of the 1TH sample) were excluded due to the problems with the surface profiler measurements.

Intuitively, one would expect that the Er diffusion in magnetron sputtered SiO_2 would be faster than that in both CVD and thermally grown SiO_2 due to the less compact structure of magnetron sputtered SiO_2. However, from the overall comparison between the diffusion coefficients determined for the four different types of samples shown in Fig. 4 we note the following points: (1) The buried samples (2MS) are more trustworthy due to the lack of surface effect, (2) the diffusion coefficients determined from the in-diffusion experiments from a surface source are identical within uncertainty which indicates that the Er diffusion is not very sensitive to the origin of SiO_2, (3) the observation that the diffusion coefficients of the two purely magnetron sputtered samples (1MS and 2MS) differ by approximately a factor of two, indicates a systematic effect (experimental or possibly a physical surface effect) which is not understood so far. These points taken together, we are confident about the fitting parameters of Eq. (1) for a magnetron sputtered sample, and the diffusion coefficient is comparable for the thermally grown or CVD grown SiO_2.

In summary, Er diffusion in different SiO_2 matrices prepared by magnetron sputtering, CVD, and thermal growth have been characterized by SIMS, and diffusion coefficients have been extracted from simulations. Very accurate diffusion coefficients have been extracted for diffusion of a buried Er distribution in a magnetron sputtered SiO_2 layer. In this case a simple Arrhenius law can describe the diffusivity in the whole investigated temperature range with an activation energy of diffusion of $\Delta E = 5.3 \pm 0.1$ eV. Furthermore, comparable diffusion coefficients for all four types of samples indicate that there is no significant difference between Er diffusion in the magnetron sputtered, CVD deposited or thermally grown SiO_2 layers used in the present investigation.

This work was supported by a grant from the Danish Council for Technology and Innovation, FTP grant #274-07-0523 project SERBINA. BJ acknowledges support from the Danish Council for Independent Research | Natural Sciences (FNU). We acknowledge Department of Micro- and Nanotechnology at the Technical University of Denmark for supplying the CVD deposited and thermally grown SiO_2 samples. We also thank J. Chevallier for the sample preparation by magnetron sputtering, and J. Lundsgaard Hansen for valuable SIMS discussions.

[1] A. Polman, J. Appl. Phys. **82**, 1 (1997).
[2] M. Fujii, M. Yoshida, S. Hayashi, and K. Yamamoto, J. Appl. Phys. **84**, 4525 (1998).
[3] C. E. Chryssou, A. J. Kenyon, T. S. Iwayama, C. W. Pitt, and D. E. Hole, Appl. Phys. Lett. **75**, 2011 (1999).
[4] F. Priolo, G. Franzó, D. Pacifici, V. Vinciguerra, F. Iacona, and A. Irrera, J. Appl. Phys. **89**, 264 (2001).
[5] H. Rinnert, G. Wora Adeola, and M. Vergnat, J. Appl. Phys. **105**, 036101 (2009).
[6] J. Jhe, J. H. Shina, K. J. Kim, and D. W. Moon, Appl. Phys. Lett. **82**, 4489 (2003).
[7] F. Gourbilleau, R. Madelon, C. Dufour, and R. Rizk, Opt. Mater. **27**, 868 (2005).

[8]B. Garrido, C. García, P. Pellegrino, D. Navarro-Urrios, N. Daldosso, L. Pavesi, F. Gourbilleau, , and R. Rizk, Appl. Phys. Lett. **89**, 163103 (2006).
[9]I. Izeddin, D. Timmerman, T. Gregorkiewicz, A. S. Moskalenko, A. A. Prokofiev, I. N. Yassievich, and M. Fujii, Phys. Rev. B **78**, 035327 (2008).
[10]D. L. Dexter, J. Chem. Phys. **21**, 836 (1953).
[11]G. F. Grom, D. J. Lockwood, J. P. McCaffrey, H. J. Labbe, P. M. Fauchet, B. White Jr., J. Diener, D. Kovalev, F. Koch, and L. Tsybeskov, Nature **407**, 358 (2000).
[12]M. Zacharias, J. Heitmann, R. Scholz, U. Kahler, M. Schmidt, and J. Bläsing, Appl. Phys. Lett. **80**, 661 (2002).
[13]J. Heitmann, F. Müller, M. Zacharias, and U. Gösele, Adv. Mater. **17**, 795 (2005).
[14]A. Polman, D. C. Jacobson, D. J. Eaglesham, R. C. Kistler, and J. M. Poate, J. Appl. Phys. **70**, 3778 (1991).
[15]M. W. Sckerl, S. Guldberg-Kjaer, M. Rysholt Poulsen, P. Shi, and J. Chevallier, Phys. Rev. B **59**, 13494 (1999).
[16]R. E. Goacher, H. Luo, and J. Joseph A. Gardella, Anal. Chem. **80**, 3261 (2008).

Appendix E

Phys. Rev. B, 84, 085403 (2011)

Er sensitization by a thin Si layer: Interaction-distance dependence

B. Julsgaard,[1,*] Y.-W. Lu,[1] R. V. Skougaard Jensen,[2] T. G. Pedersen,[2] K. Pedersen,[2] J. Chevallier,[1] P. Balling,[1] and A. Nylandsted Larsen[1]

[1]*Department of Physics and Astronomy, Aarhus University, DK-8000 Aarhus C, Denmark*

[2]*Department of Physics and Nanotechnology, Aalborg University, DK-9220 Aalborg East, Denmark*

(Received 30 May 2011; revised manuscript received 5 July 2011; published 19 August 2011)

From photoluminescence measurements on sensitized erbium in a-Si/SiO_2:Er/SiO_2 multilayers, we determine the characteristic interaction length of the sensitization process from the silicon-layer sensitizer to the erbium-ion receiver to be 0.22 ± 0.02 nm. By using sufficiently low temperatures in the fabrication steps, we ensure that diffusion of erbium ions does not affect our results. In addition, we demonstrate that saturation of the erbium $^4I_{13/2} \rightarrow {}^4I_{15/2}$ transition may lead to an exaggerated estimate of the interaction distance.

DOI: 10.1103/PhysRevB.84.085403 PACS number(s): 71.35.Gg, 76.30.Kg, 78.67.Bf

I. INTRODUCTION

Since the discovery that Er^{3+} can be sensitized by, for example, silicon (Si) nanocrystals,[1,2] there has been a great effort in understanding the mechanisms behind the energy transfer process from the silicon-based sensitizer to the erbium (Er) receiver ions. It has been demonstrated that not only silicon nanocrystals can sensitize Er^{3+} but luminescence centers can act as efficient sensitizers,[3] and the sensitization is enabled even at low annealing temperatures in samples based on either silicon layers[4] or silicon-rich silica,[5] which gives rise to a higher concentration of Si-grain sensitizers and, hence, more effective Er luminescence as compared to Si-nanocrystal sensitization.

The sensitizer-to-receiver distance dependence of the energy transfer has also been investigated in great detail in order to understand the actual physical origin of the interaction mechanism.[6–12] In particular, two mechanisms have been proposed:[13] (1) the Dexter mechanism in which the sensitizer and receiver exchange electrons—this process requires an overlap of sensitizer and receiver wave functions leading to a transfer efficiency decreasing exponentially with the distance, and (2) the Förster resonant energy transfer in which the near field from the sensitizer and receiver optical dipoles are coupled with a characteristic x^{-6} point-to-point dependence. Most studies suggest that the Dexter mechanism is responsible for the energy transfer,[6–9,12] while it has been pointed out that by taking the three-dimensional nature of the process into account, both processes lead to similar plane-to-plane distance dependencies.[10]

However, apart from a recent experiment using room-temperature fabrication steps,[12] the above-mentioned studies have ignored the possibility that the Er ions diffuse during the sample annealing process. In the present study, we examine the energy transfer efficiency as a function of interaction distance using Si/SiO_2:Er/SiO_2 multilayer samples subject to annealing temperatures sufficiently low to exclude effects of Er diffusion. Furthermore, we demonstrate that if the optical excitation of the sensitizer is too strong, the Er^{3+} transition at 1.5 μm will saturate with an overestimated interaction distance as a result. Simplified theoretical models are given in order to estimate the effects of Er diffusion and saturation.

This paper is organized as follows. In Sec. II we describe the sample fabrication process, while details of the optical measurement setup is given in Sec. III. The actual optical characterization is covered in Sec. IV, while the interpretation and main results are discussed in Sec. V. After the final conclusion in Sec. VI, two Appendices present the simplified modeling of Er diffusion (Appendix A) and saturation effects (Appendix B).

II. SAMPLE FABRICATION

The samples were fabricated by radio-frequency-magnetron sputtering with substrate heating at 200 °C. The sample layout is depicted in Fig. 1(a). On a Si wafer, a 10-nm layer of SiO_2 was deposited followed by ten multilayers, each of which consists of a pure SiO_2 layer of thickness $10 - d$ nm, an Er-doped SiO_2 layer of thickness d followed by a 1.5-nm Si layer. Hence, each SiO_2 layer is fixed to a total thickness of 10 nm. Finally, the samples were capped by 50 nm of SiO_2. The thickness d of the Er-rich SiO_2 layers was varied between the nominal values (in nanometers) 0, 0.3, 0.6, 0.9, 1.2, 1.5, 2.0, and 3.0. The thickness of the Er-rich layers was controlled by varying the deposition time while keeping the sputtering power constant.

The samples were annealed for one hour at 700 °C in N_2 (2.0 Bar) followed by a 1-hour passivation step at 500 °C in a N_2(95%) + H_2(5%) atmosphere (2.0 Bar). The sample-to-sample standard deviation in Er concentration was eight percent measured by secondary ion mass spectrometry—all Er-related photoluminescence (PL) yields have been corrected for this slight variation. In comparison to a sample with a known Er concentration (measured by Rutherford backscattering spectrometry), the absolute Er concentration was estimated to be 0.3 atomic percent. According to the estimates of Appendix A, the heat treatment at 700 °C will not give rise to any diffusion of Er ions. A transmission electron micrograph of the sample is presented in Fig. 1(b).

III. EXPERIMENTAL SETUP

The samples were attached in an optical characterization setup as depicted in Fig. 2. As an excitation source we used a continuous-wave diode laser at 405 nm. The excitation intensity was controlled by adjusting the pumping power and (for the lowest intensities) by increasing the spot size of the excitation beam at the sample position. Beam sizes

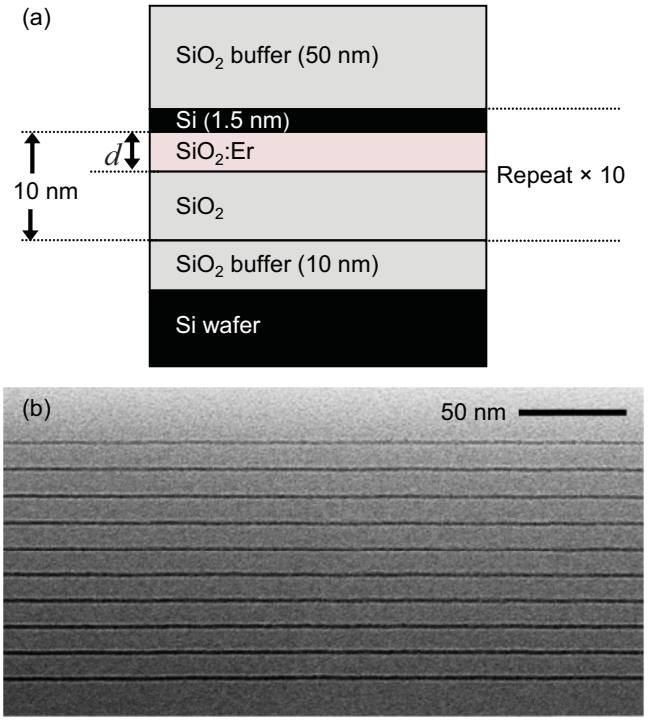

FIG. 1. (Color online) (a) Schematic view of the sample preparation steps. (b) Transmission electron micrograph of the sample with a nominal layer thickness $d = 3.0$ nm after annealing at 700 °C. The dark horizontal lines correspond to the Si layers.

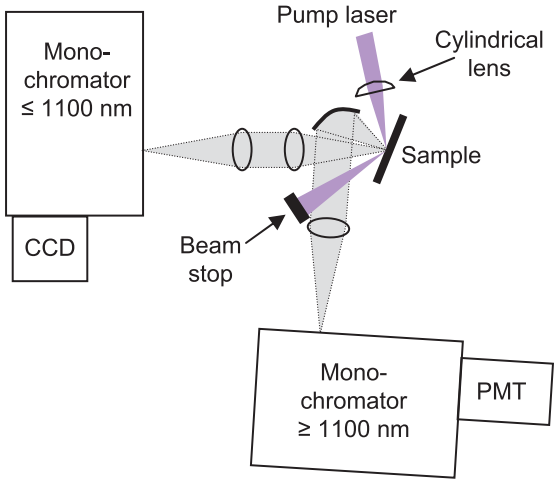

FIG. 2. (Color online) The optical characterization apparatus. The sample is mounted in a sample holder and subjected to pump light (p polarized), a focus of which can be adjusted down to approximately 100 microns by translation of a cylindrical lens. Different spectral parts of the emitted light is collected simultaneously by two monochromators. One is equipped with a charge-coupled device (CCD), and the other with a photomultiplier tube (PMT).

were estimated by illuminating a charge-coupled device (CCD)-camera chip, and intensities have been corrected for the incidence angle and for the reflection from the sample surface. The photoluminescence at wavelengths above 1100 nm was detected by a liquid-nitrogen-cooled photomultiplier tube (Hamamatsu R5509-73) attached to a McPherson 218 monochromator. In the wavelength range 700–1100 nm, the PL was detected by a CCD camera (Princeton Instruments, PIXIS 100BR) attached to an Acton Research 300-mm focal length monochromator.

IV. OPTICAL CHARACTERIZATION

The spectrum from an Er-rich sample is displayed in Fig. 3 and shows the following features: (1) the luminescence from the Er transition $^4I_{13/2} \rightarrow {}^4I_{15/2}$, which peaks at 1535 nm, (2) a luminescence band characteristic of the silicon bulk band gap peaking around 1137 nm (1.091 eV), (3) a peak at 983 nm from the Er transition $^4I_{11/2} \rightarrow {}^4I_{15/2}$, and (4) a broad feature extending from 700 nm to the Si-bulk-related peak. We attribute the latter feature to luminescence from the deposited 1.5-nm silicon layers.

The luminescence peak at 1535 nm is used as the figure of merit for the energy transfer from the Si layer to the Er ions. At the same time, the integrated luminescence in the range 700–950 nm brings information about the dynamics of electrons and holes in the sensitizing Si layer.

A. Saturated erbium excitation

The Er and Si-layer PL yields are plotted in Fig. 4 as a function of pumping intensity and reveal a very significant feature: the Si-layer PL yield increases proportionally with the intensity in the entire range examined. Hence, there are no saturation effects in the sensitizer part of the sensitization process. In contrast, the Er-related PL yield shows a significant saturation effect for high excitation intensities; the finite number of Er ions together with their radiative decay rate sets the ultimate upper limit for the luminescence yield.

In a simplified one-dimensional model of the energy transfer process (details are given in Appendix B), we let the excitation rate $P(x)$ of the $^4I_{13/2}$ state in an Er ion depend on the Si-layer-to-Er-ion distance x as $P(x) = P_0 \exp(-x/x_0)$, where x_0 is the characteristic interaction distance. Taking Γ as the decay rate of the $^4I_{13/2}$ state, the luminescence yield Y can

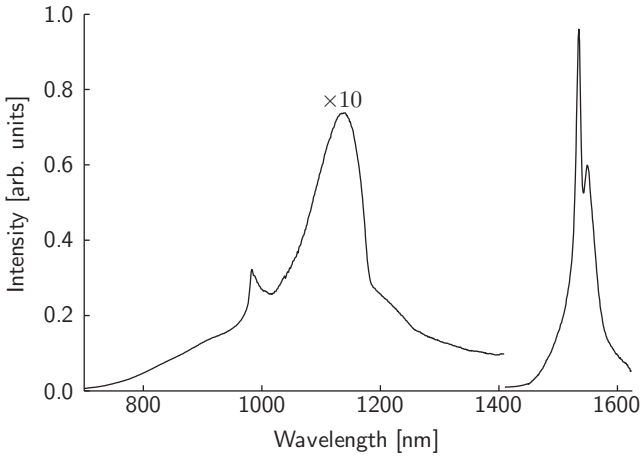

FIG. 3. The emitted spectrum from the sample with nominal Er-layer thickness of 3.0 nm under continuous pumping at 405 nm with intensity $I = 10^4$ W/m^2. The part below 1400 nm has been multiplied by a factor of ten for clarity.

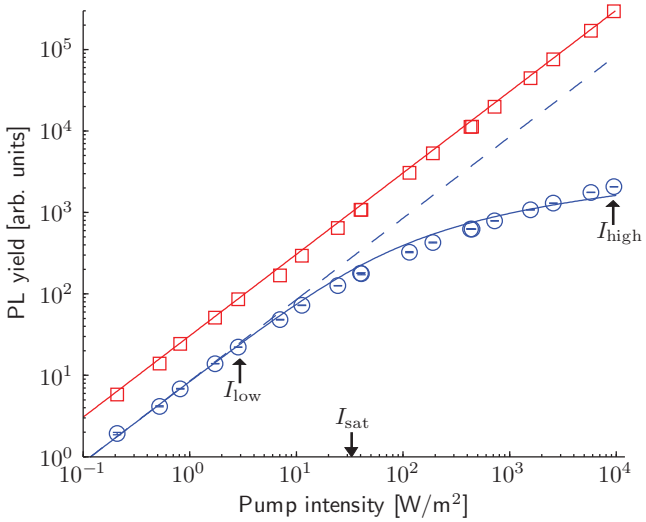

FIG. 4. (Color online) The photoluminescence yield at 1535 nm (circles) and in the range 700–950 nm (squares) vs pumping intensity for the sample with 3.0 nm Er-layer thickness. The vertical position of each data set is arbitrary. The straight lines denote proportionality fits of the data, the dashed line is fitted to the five lowest-intensity points only. The solid line through the circles represents a fit to the expression in Eq. (1) with A fixed at the slope of the dashed line and the saturation intensity fitted to $I_{sat} = 33\ \mathrm{W/m^2}$. The data points corresponding to the low and high intensities, $I_{low} = 3.0\ \mathrm{W/m^2}$ and $I_{high} = 0.94 \times 10^4\ \mathrm{W/m^2}$, are marked on the graph.

be found as a function of the Er-layer thickness d for a given ratio P_0/Γ, see Eq. (B1). In the limit $d \gg x_0$, we obtain

$$Y_\infty = C \ln\left(\frac{P_0}{\Gamma} + 1\right) \equiv A I_{sat} \ln\left(\frac{I}{I_{sat}} + 1\right), \qquad (1)$$

where I_{sat} is defined as the intensity required for having the pumping rate P_0 equal to the decay rate Γ. The front factor A represents the slope in the linear regime, $I \ll I_{sat}$. The above model is fitted to the experimental data in Fig. 4. It is clear that the fit is not perfect, however, by its logarithmic behavior at large intensities it includes the experimental feature that although the increase in PL yield slows down, there is not a specific upper limit within reach.

In the data analysis to follow, we will use two specific excitation intensities I_{low} and I_{high}, which are marked in Fig. 4. The lower intensity I_{low} is clearly in the linear regime, whereas the higher one I_{high} leads to saturation of the Er-receiver system (but not the Si-related sensitizer system). In the following section, we examine the effect of saturation on the distance-dependent sensitizer-receiver interaction.

B. Distance dependence of erbium excitation

In the optical characterization apparatus, the photoluminescence yield from each of the samples was measured, the result of which can be used to estimate the distance dependence of the sensitizer-receiver interaction. The PL yield (normalized to the mean yield of the data points with $d \geqslant 1.2$ nm) for excitation intensities I_{low} and I_{high} are plotted in Fig. 5, panel (a) and (b), respectively. Each data point was obtained in eight steps, in which the luminescence at 1535 nm (resolution 8 nm)

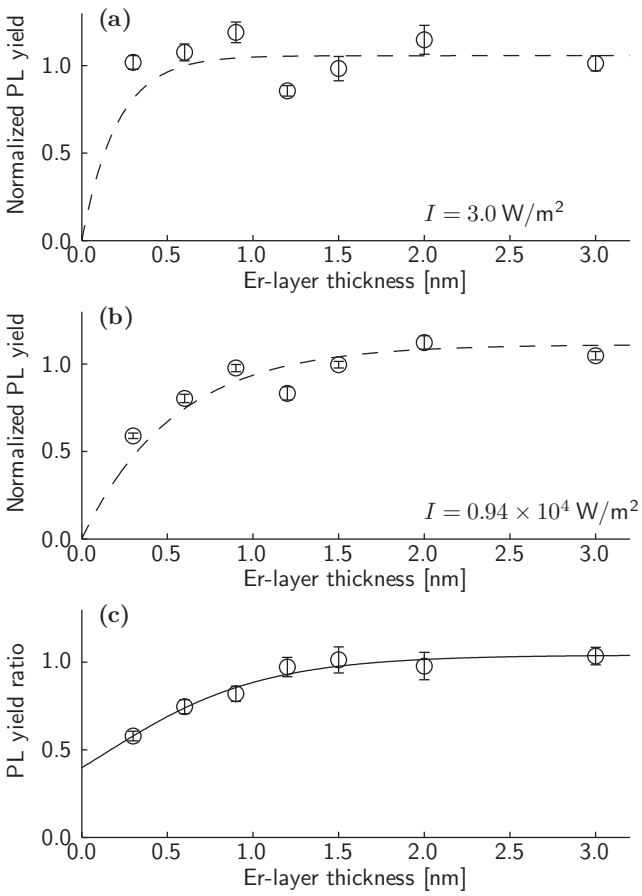

FIG. 5. The dependence of the 1535-nm normalized PL yield on the Er-layer thickness. Panels (a) and (b) show the luminescence yield obtained at low and high pump intensities, respectively. The data in panel (c) is the PL yield ratio $Y_{I=I_{high}}/Y_{I=I_{low}}$, i.e., the data of panel (b) normalized to the data of panel (a). The solid line in panel (c) is a fit to Eq. (2), and the dashed lines in panels (a) and (b) show the in-growth function $y = A[1 - \exp(-x/x_0)]$ with x_0 fixed at the fitted values x_{low} and x_{high}, respectively.

was accumulated for one minute. Between each step the sample was moved slightly in order to average out possible sample inhomogeneities. The error bars in Fig. 5 represent the statistical uncertainty of the averaged luminescence yield—the dominant source of uncertainty is in fact given by the reproducibility of each step, i.e., by sample inhomogeneities.

Comparing the data in panels (a) and (b) of Fig. 5, we also observe a systematic source of error; the data points show a slight scattering common to the two graphs (most pronounced is the point at 1.2 nm thickness, which has fallen well below its neighbors). We attribute this to sample-to-sample variations—the scattering represents the precision of the fabrication process. Nonetheless, the two data sets are clearly different as the luminescence increases slower in panel (b) compared to panel (a), i.e., the effect of saturation causes an apparently longer interaction distance. In order to examine this effect further, we plot in panel (c) the "PL yield ratio" defined as the data in panel (b) normalized to that of panel (a), i.e., panel (c) represents the high-excitation-intensity normalized PL yield divided by the low-excitation-intensity normalized

PL yield. The effect of saturation has now become very clear as the PL yield ratio is definitely increasing as a function of Er-layer thickness. But more importantly, the PL yield ratio is insensitive to the systematic sample-to-sample variations as the luminescence yields at low and high intensities are affected equally by these variations [this is evident from the fact that in panel (c) the scattering is within the statistical error bars in contrast to panels (a) and (b)]. For this reason the curve-fitting analysis to follow is based entirely on the data of Fig. 5(c).

In modeling the photoluminescence yields, we choose (in any case independent on the level of saturation) the functional dependence, $Y = A[1 - \exp(-x/x_0)]$, which corresponds to a one-dimensional, unsaturated exchange (Dexter) model. This simplified description is a practical choice, which in fact, with its few free parameters, fits the data nicely. As mentioned in Appendix B it is theoretically inadequate if saturation effects are significant in which case Eq. (B2) should be used instead. However, there could be additional effects that are not covered by the model of Appendix B; as mentioned in the introduction, a more complete three-dimensional theory exists[10] in which the sensitization process is integrated over the sensitizer-layer thickness, and which also discusses the possibility of Förster resonant energy transfer. However, the authors behind this theory could not distinguish between the transfer mechanisms in practice, and it may even be questioned whether it is correct to integrate over the sensitizer layer thickness since the luminescence centers responsible for the sensitization[3] could be located on the surface only. Furthermore, effects of excited-state absorption and cooperative up-conversion[14,15] are also not included. The available data, anyway, will not allow us to distinguish among all these various details, and the simplified model is retained.

Taking the low-intensity data of Fig. 5(a) to represent the model $Y_{\text{low}} = A_{\text{low}}[1 - \exp(-x/x_{\text{low}})]$ and the high-intensity data of panel (b) to reflect $Y_{\text{high}} = A_{\text{high}}[1 - \exp(-x/x_{\text{high}})]$, where x_{low} and x_{high} are the characteristic interaction distances when $I = I_{\text{low}}$ and $I = I_{\text{high}}$, respectively, we can model the PL yield ratio of panel (c) as

$$\frac{Y_{\text{high}}}{Y_{\text{low}}} = A\frac{1 - \exp(-x/x_{\text{high}})}{1 - \exp(-x/x_{\text{low}})}. \tag{2}$$

As can be see from Fig. 5(c), this model apparently fits the data, and we extract the fitting parameters: $x_{\text{low}} = 0.21 \pm 0.06$ nm, $x_{\text{high}} = 0.54 \pm 0.10$ nm, and $x_{\text{high}}/x_{\text{low}} = 2.6 \pm 0.4$. The individual yield models Y_{low} and Y_{high} have been added in panels (a) and (b) for comparison, and we stress that the parametrization of these curves is based on the fit to the data in panel (c). If instead the data in only panel (a) had been used to extract a value x_{low} for the characteristic interaction distance, the single left-most data point at $d = 0.3$ nm would essentially determine x_{low}, which would lead to a rather uncertain value due to the sample-to-sample scattering. Indeed, it is the comparison to the corresponding data point in panel (b), which allows for the more accurate estimate of the interaction distance.

So far, the results can be summarized to an effective sensitizer-receiver interaction distance measured by the parameter $x_{\text{low}} = 0.21 \pm 0.06$ nm, which in practice appears larger by a factor $x_{\text{high}}/x_{\text{low}} = 2.6 \pm 0.4$ when the excitation intensity is increased to $I_{\text{high}} = 0.94 \times 10^4$ W/m^2. In comparison, the inverse slope of Eq. (B2) in the limit $d \to 0$ (which present a rough estimate of the interaction distance under the influence of saturation) predicts an enhancement factor $x_{\text{high}}/x_{\text{low}} = 5.7$ when taking $\frac{P_0}{\Gamma} = \frac{I_{\text{high}}}{I_{\text{sat}}}$ and $I_{\text{sat}} = 33$ W/m^2 (fitted value, see Fig. 4). The discrepancy in the enhancement factor is not surprising since the model of Appendix B presents a simplified, qualitative description of the saturation effects.

C. Distance dependence of Si-layer luminescence

In order to examine the Si-layer luminescence, we plot in Fig. 6 as a function of the Er-layer thickness, the intensity integrated over the wavelength range 700–950 nm (thus excluding possible impacts from the Er luminescence line at 983 nm). The results in panel (a) and (b) correspond to intensities I_{low} and I_{high}, respectively, and the error bars reflect the statistical uncertainty of the average of eight measurement steps (just as in the case of the 1535-nm luminescence in Fig. 5). We note the following features common to both panels: (1) there is a significant decrease for increasing layer thicknesses below 0.5 nm, (2) the decrease continues in the entire range investigated, and (3) there seems to be no drastic effects of saturation in panel (b) as compared to panel (a).

A quantitative investigation of the data is performed by fitting the data to the model $y = A_1 \exp(-d/x_1) + A_2 \exp(-d/x_2)$. As mentioned in Sec. IV B, there are numerous effects needed to be taken into account for a detailed theory, which is outside the scope of the present work. Instead, we use an exponential dependence as a descriptive model, which includes most importantly (by the fitting parameter x_1 of the first exponential term) the initial short-distance-scale decrease. The continued decrease in PL yield is accounted for by the second term, and since there are no indications whether the

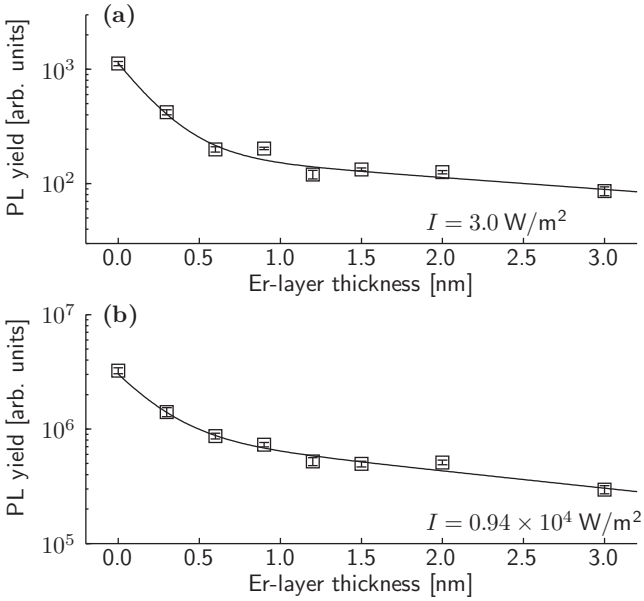

FIG. 6. The dependence of the integrated photoluminescence yield in the range 700–950 nm on the Er-layer thickness. Panels (a) and (b) show the yield obtained at low and high pump intensities, respectively. The solid lines are fits to a double-exponential model.

data would converge toward zero or any other value at larger Er-layer thicknesses, the second-term length scale x_2 should only be taken as a free parameter to match the data.

The fitting results in Fig. 6(a) are $x_1 = 0.21 \pm 0.03$ nm, $x_2 = 4.2 \pm 1.2$ nm, and $A_2/A_1 = 0.19 \pm 0.04$. In panel (b), we obtain $x_1 = 0.24 \pm 0.05$ nm, $x_2 = 2.9 \pm 0.6$ nm, and $A_2/A_1 = 0.40 \pm 0.09$. Remarkably, within uncertainties the short-distance scale x_1 is independent on the intensity and agrees with the low-intensity sensitizer-receiver interaction distance x_{low} from the 1535-nm luminescence yield of Fig. 5. Assuming that the two x_1 values from Fig. 6 and x_{low} from Fig. 5 are independent measurements of the characteristic sensitizer-receiver interaction distance, we find a combined value of 0.22 ± 0.02 nm.

It is indeed reasonable that the short-distance scale x_1 of Fig. 6 is independent of the excitation intensity and that the two panels of Fig. 6 appear very similar in general; the Si-layer photoluminescence yield does not show any saturation (see Fig. 4), but since it is always quenched by the presence of Er ions (both for low and high pump intensity, see Fig. 6), we conclude that energy always flows from the Si-layer to the Er ions, i.e., independently of the excitation intensity. Hence, Er ions do always receive a large fraction of the energy available from the Si layer. If the $^4I_{13/2}$ state is already highly populated, e.g., in the strongly saturated case, the Er ion is just excited to an even higher energy state (and subsequently decaying back to possibly the $^4I_{13/2}$ state).

A convenient estimate of the Si-layer-luminescence quenching specifically due to the short-distance-scale energy transfer mechanism (with 0.22 nm characteristic interaction distance) is given by the fitted value of A_2/A_1 in Fig. 6. In panel (a), the "direct-quenching fraction" is $\frac{A_1}{A_1+A_2} = \frac{1}{1+A_2/A_1} = 0.84 \pm 0.03$, whereas in panel (b), we find 0.71 ± 0.05. In addition, when increasing the Er-layer thickness from 1.0 to 3.0 nm, the Si-layer luminescence is quenched by approximately a further factor of two. Since this is not accompanied by a corresponding increase in the Er PL (Fig. 5), we suggest that a separate Er-related quenching mechanism must be present.

V. DISCUSSION

Saturation of the $^4I_{13/2} \rightarrow {}^4I_{15/2}$ transition at 1535 nm definitely plays a role in the estimation of the characteristic interaction distance as seen directly by the data in Fig. 5. Such an increase of the apparent interaction distance together with the constant length scale of the Si-related PL has in fact been reported previously.[11] In this study, it was suggested that energy transfer processes between individual Er ions was responsible for the additional length scale. We can not exclude that such a transfer takes place; however, we find that the saturation effect must be dominant since in the nonsaturated limit the two length scales (x_{low} in Fig. 5 and x_1 in Fig. 6) coincide.

We also wish to note that the thinnest nominal Er-rich layer thickness and the derived characteristic interaction distance are both comparable to interatomic distances. Hence, it is clear that the experimental resolution is reaching ultimate limits and one could in fact speculate whether the increase in Er PL as a function of the Er-layer thickness d is a purely statistical feature, i.e., if it would require a rather thick layer (compared to an atomic bond length) to ensure that the entire Si layer has been covered with Er-rich SiO_2. We cannot exclude that our results are influenced slightly by such statistical effects; however, the flatness of the Si layers observed from Fig. 1(b) suggests that the deposition process runs predominantly in a layer-by-layer fashion. In any case, there must be a real physical dependence of the energy transfer efficiency on the Er-ion-to-Si-layer distance. Otherwise, all sensitized ions would always behave in the exact same manner and, in particular, be saturated to the same level at high excitation intensities. This contradicts the observed distance dependence of the PL yield ratio in Fig. 5(c).

As already mentioned, Er ions, which are already excited to the $^4I_{13/2}$ state, can easily receive more energy and become further excited. This effect is not included in the modeling of saturation in Appendix B. In addition, effects of cooperative up-conversion[14,15] could also play a role in the dynamics. It is clear that our saturation model is too simple to match exactly the experimental data in Fig. 4. Anyway, the model delivers an intuitive explanation of the overestimated (power broadened) interaction distance as observed from Fig. 5(b).

The modeling of the distance dependence is based on an exponential dependence, $P(x) = P_0 \exp(-x/x_0)$, which leads to a satisfactory fit to the experimental data. It is thus tempting to conclude that the Dexter mechanism is responsible for the energy transfer. However, in the light of a more elaborate three-dimensional analysis,[10] which concludes that the Dexter and Förster mechanisms lead to similar plane-to-plane features, one should be cautious with such a conclusion. In any case, it resides without question that, for the main part of the energy transfer, the effective interaction distance of 0.22 ± 0.02 nm is very short and comparable to the interatomic distance. This indicates that overlap of wave functions is a requirement for the efficient energy transfer, which is in agreement with recent studies on Er^{3+} forced to be in direct contact with Si nanostructures.[12] We remind that the continuing decrease of Si-layer PL in Fig. 6 indicates that further processes may take place in addition to the dominant short-range Si-to-Er energy transfer.

A. The role of Er diffusion

Now let us go through the previously published results on the interaction-distance dependence of Er sensitization, which have been carried out with SiO_2-based samples. In the following, the uncertainties on the diffusion lengths arise from measurements on Er ions embedded far from surfaces inside a magnetron-sputtered host of SiO_2, but we emphasize that, in general, the diffusion length should be valid within a factor of two. See Appendix A for details.

In Ref. 9, all samples were annealed at 900 °C for 1 hour. This corresponds to a diffusion coefficient of $D(900\,^\circ\text{C}) = 2.1(3) \times 10^{-19}$ cm^2/s and a diffusion length of $L = 0.27(2)$ nm. While this number might influence their stated interaction distance of 0.4 ± 0.1 nm for amorphous-Si sensitizers (grown from a 1.8 nm layer of silicon-rich silicon oxide), the authors also state significantly longer interaction distances (up to 5 nm) for crystalline Si sensitizers. The latter case is obviously not an Er-diffusion related artifact.

In Refs. 8 and 15, a uniform distribution of Er ions around Si nanocrystals was assumed. In addition, by assuming that the Si nanocrystal interacts with the nearest unexcited Er ion with a rate $K \propto \exp[-(R - R_{nc})/R_0]$, the authors managed to estimate $R_0 \approx 0.45$ nm from the photon-flux dependence of Er photoluminescence. The samples were annealed for 1 hour at 900 °C, which, as in the above case, translates into a diffusion length of $L = 0.27(2)$ nm. While diffusion does not change the uniformity in a homogeneous medium, the results might be slightly affected by effects near the Si nanocrystals.

For $T = 950$ °C, the diffusion coefficient is $D(950\,^{\circ}\mathrm{C}) = 1.8(2) \times 10^{-18}$ cm^2/s. Exposing a sample to this temperature for five minutes (as was done in the work of Ref. 7) we find a diffusion length $L = 0.23(1)$ nm, which is roughly half of their reported value of the interaction distance 0.5 nm. Hence, some influence of diffusion on this result is possible.

In Ref. 10, a temperature of 1000 °C was used, in which case the diffusion coefficient is $D(1000\,^{\circ}\mathrm{C}) = 1.28(9) \times 10^{-17}$ cm^2/s while the annealing time was unspecified. The authors found a characteristic interaction distance of 5 nm assuming the simple exponential dependence of the Dexter mechanism. This number was stated as nonphysically large and by integrating the Förster mechanism (x^{-6} dependence) over space in three dimensions an alternative explanation was also stated. For comparison, a 1-hour annealing time at 1000 °C leads to a diffusion length of $L = 2.15(7)$ nm.

In Ref. 6, a layer of Er ions was deposited onto a preoxidized sample of porous silicon. In order to activate the optical emission, the samples were annealed at 1200 °C for 30 seconds. This corresponds to a diffusion coefficient of $D(1200\,^{\circ}\mathrm{C}) = 9.0(8) \times 10^{-15}$ cm^2/s and a diffusion length of $L = 5.2(2)$ nm. For comparison, the authors estimate the energy-transfer rate to decrease exponentially with Si-Er distance where the characteristic length is $\frac{1}{0.36\,\mathrm{nm}^{-1}} \approx 2.8$ nm. This result must be heavily influenced by the Er diffusion.

By working through the above examples, we find that the experiments conducted at the lowest temperatures give a characteristic interaction distance of the order of 0.4 nm, and remembering that these results could be overestimated slightly by a diffusion length of approximately 0.2 nm, this is definitely consistent with our somewhat smaller characteristic interaction distance of 0.22 nm in absence of Er diffusion. For comparison, in our experiments the highest heat treatment temperature was 700 °C to which the samples were exposed for 1 hour. The characteristic diffusion length in this case is estimated to be $L(700\,^{\circ}\mathrm{C}) = 1.3 \times 10^{-3}$ nm, which means in practice that Er ions are stationary.

VI. CONCLUSION

We have measured the effective interaction distance between a sensitizing a-Si layer and Er receiver ions to be 0.22 ± 0.02 nm. Our experimental approach excludes effects of Er diffusion and saturation, which can otherwise exaggerate the estimate of the interaction distance. The short range of the interaction is comparable to interatomic distances, which indicates that wave-function overlap is a requirement for the transfer process.

ACKNOWLEDGMENTS

This work was supported by the Danish Council for Independent Research, Technology and Production Sciences (FTP), SERBINA project, by the Danish Council for Independent Research, Natural Sciences (FNU), and by the Carlsberg Foundation. The first two authors contributed equally to this work.

APPENDIX A: INFLUENCE OF ER DIFFUSION

The role of Er diffusion can be estimated from the diffusion coefficient of Er in SiO_2, which follows the Arrhenius law: $D = D_{T_0} \exp[-\frac{\Delta E}{k_B}(T^{-1} - T_0^{-1})]$, where T is the temperature in Kelvin, $T_0 = 1346$ K is a reference temperature at which the diffusion coefficient is $D_{T_0} = (1.76 \pm 0.08) \times 10^{-16}$ cm^2/s, and $\Delta E = (5.3 \pm 0.1)$ eV is the activation energy.[16] The uncertainties on these parameters relate specifically to a magnetron-sputtered SiO_2 host with Er ions located far within the host matrix. However, for Er ions closer to the surface or for Er ions in other types of SiO_2 (thermal oxide or grown by chemical vapor deposition), similar diffusion coefficients within a factor of three were found.[16] If t denotes the time of a heat treatment, the characteristic diffusion length, $L = \sqrt{Dt}$, can thus be conservatively estimated to within a factor of two.

Let us consider (in a simple one-dimensional model) how Er diffusion relates to the particular geometry of our experimental procedure. If an infinitesimal layer of Er with concentration ρ_0 and thickness dx_0 is located within a SiO_2 matrix at position x_0 [see Fig. 7(a)], the impact of diffusion on this layer leads to the x-dependent concentration:

$$\rho(x) = \frac{\rho_0 dx_0}{2L\sqrt{\pi}} \exp\left[-\frac{(x - x_0)^2}{4L^2}\right], \tag{A1}$$

where $L = \sqrt{Dt}$ is the diffusion length. Now, assume that a sensitizer of Er emission is located at $x = 0$, and that the sensitization interaction is short-range (compared to L). Then the Er ions must travel by diffusion to $x = 0$ in order to be sensitized. We stress that Eq. (A1) is, in principle, only applicable within the SiO_2 host in absence of material boundaries. When Er ions reach the sensitizer (e.g., a thin Si layer), we simply assume that they stay there and become optically active. Hence, we assume that the sheet density $\sigma(x_0)dx_0$ of sensitized Er ions originating from the infinitesimal layer at x_0 is given by

$$\sigma(x_0)dx_0 = \int_{-\infty}^{0} \rho(x)dx = \frac{1}{2}\mathrm{erfc}(\xi)\rho_0 dx_0, \tag{A2}$$

where $\mathrm{erfc}(\xi)$ is the complementary error function and $\xi = x_0/2L$. Now, assume the Er ions were initially distributed uniformly with density, ρ_0, in the range $x = 0$ to $x = d$, i.e., an Er layer with thickness d is located right next to a thin sheet of sensitizers. The total sheet density σ_d of Er ions, which by diffusion reach the sensitizer layer, is then

$$\begin{aligned}\sigma_d &= \int_0^d \sigma(x_0)dx_0 \\ &= \frac{\rho_0 L}{\sqrt{\pi}}\left[1 - e^{-\mu^2} + \sqrt{\pi}\,\mu\,\mathrm{erfc}(\mu)\right],\end{aligned} \tag{A3}$$

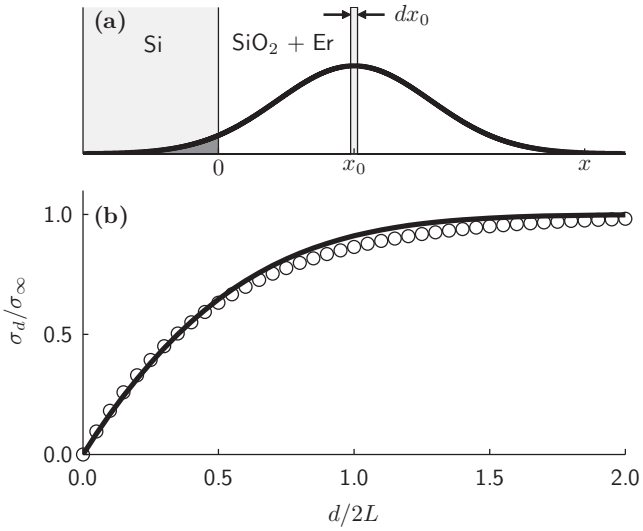

FIG. 7. (a) Schematics of the diffusion model. An initial distribution of Er is located at x_0 within the thickness dx_0. A subsequent heat treatment broadens the Er concentration (solid line, exaggerated in magnitude) according to Eq. (A1). The part, which falls below $x = 0$, is assumed to become optically active. (b) The solid line denotes the analytical sheet carrier density of Eq. (A3). The circles show a simple exponential in-growth with characteristic length L.

where $\mu = d/2L$. This function approaches zero when $d \to 0$ and it saturates at $\sigma_\infty = \rho_0 L/\sqrt{\pi}$ for large d. There is a great similarity with a simple exponential in-growth: $\sigma_d^{(\exp)} = \sigma_\infty[1 - \exp(-d/L)]$, as can be seen from Fig. 7(b). If L is not much larger than the interaction distance x_1, the full result may still be approximated by an exponential, albeit with a better fit if $L_{\text{eff}} = \sqrt{L^2 + x_1^2}$ replaces L.

The above considerations show that if diffusion of Er ions is significant, a short-range sensitization interaction can mistakenly be interpreted as a longer, exponentially dependent interaction mechanism with characteristic interaction distance essentially determined by the diffusion length L.

APPENDIX B: INFLUENCE OF SATURATION

We will employ a one-dimensional model in which the excitation rate $P(x)$ of erbium depends exponentially on the distance x between the Er ion and the sensitizer layer: $P = P_0 \exp(-x/x_0)$. The sensitization mechanism pumps Er ions to the state $^4I_{13/2}$ (possibly via fast-decaying excited states[17]) with a rate $P(x)$. Denoting the decay rate back to the ground state $^4I_{15/2}$ by Γ, the probabilities $\rho_{13/2}$ and $\rho_{15/2}$ of populating the two lowest states are governed by the equations: $\partial\rho_{13/2}/\partial t = P\rho_{15/2} - \Gamma\rho_{13/2}$ and $\rho_{13/2} + \rho_{15/2} = 1$, which in steady state leads to $\rho_{13/2}(x) = \frac{P(x)}{P(x)+\Gamma}$. The total detected photoluminescence yield Y from Er at the 1.5-μm transition is proportional to the population $\rho_{13/2}(x)$ integrated over the Er receiver layer:

$$Y = C \ln\left[\frac{\frac{P_0}{\Gamma} + 1}{\frac{P_0}{\Gamma}\exp(-d/x_0) + 1}\right], \tag{B1}$$

where C is a constant dependent on the radiative decay rate and on details of the measurement apparatus. We note that for a thick Er layer with $d \gg x_0$, the total yield is $Y_\infty = C \ln(P_0/\Gamma + 1)$, which rises linearly with P_0 when $P_0 \ll \Gamma$ and saturates to a logarithmic dependence at high pumping rates. By normalizing the yield to its value at large Er thickness, we find

$$\frac{Y}{Y_\infty} = 1 - \frac{\ln\left[\frac{P_0}{\Gamma}\exp(-d/x_0) + 1\right]}{\ln\left(\frac{P_0}{\Gamma} + 1\right)}, \tag{B2}$$

which in fact reduces to $1 - \exp(-d/x_0)$ when saturation is negligible ($P_0 \ll \Gamma$).

*brianj@phys.au.dk

[1] A. J. Kenyon, P. F. Trwoga, M. Federighi, and C. W. Pitt, J. Phys. Condens. Matter **6**, L319 (1994).

[2] M. Fujii, M. Yoshida, Y. Kanzawa, S. Hayashi, and K. Yamamoto, Appl. Phys. Lett. **71**, 1198 (1997).

[3] O. Savchyn, P. G. Kik, R. M. Todi, and K. R. Coffey, Phys. Rev. B **77**, 205438 (2008).

[4] J. H. Shin, W. Lee, and H. Han, Appl. Phys. Lett. **74**, 1573 (1999).

[5] G. Franzo, S. Boninelli, D. Pacifici, F. Priolo, F. Iacona, and C. Bongiorno, Appl. Phys. Lett. **82**, 3871 (2003).

[6] T. Kimura, H. Isshiki, S. Ide, T. Shimizu, T. Ishida, and R. Saito, J. Appl. Phys. **93**, 2595 (2003).

[7] J. Jhe, J. H. Shina, K. J. Kim, and D. W. Moon, Appl. Phys. Lett. **82**, 4489 (2003).

[8] B. Garrido, C. García, P. Pellegrino, D. Navarro-Urrios, N. Daldosso, L. Pavesi, F. Gourbilleau, and R. Rizk, Appl. Phys. Lett. **89**, 163103 (2006).

[9] F. Gourbilleau, C. Dufour, R. Madelon, and R. Rizk, J. Lumin. **126**, 581 (2007).

[10] K. Choy, F. Lenz, X. X. Liang, F. Marsiglio, and A. Meldruma, Appl. Phys. Lett. **93**, 261109 (2008).

[11] I. Y. Kim, J. H. Shin, and K. J. Kim, Appl. Phys. Lett. **95**, 221101 (2009).

[12] S. Nunez-Sanchez, P. M. Roque, R. Serna, and A. K. Petford-Long, Appl. Phys. Lett. **98**, 151109 (2011).

[13] D. L. Dexter, J. Chem. Phys. **21**, 836 (1953).

[14] A. Polman, J. Appl. Phys. **82**, 1 (1997).

[15] B. Garrido, C. Garcia, S. Seo, P. Pellegrino, D. Navarro-Urrios, N. Daldosso, L. Pavesi, F. Gourbilleau, and R. Rizk, Phys. Rev. B **76**, 245308 (2007).

[16] Y.-W. Lu, B. Julsgaard, M. C. Petersen, R. V. S. Jensen, T. G. Pedersen, K. Pedersen, and A. N. Larsen, Appl. Phys. Lett. **97**, 141903 (2010).

[17] O. Savchyn, R. M. Todi, K. R. Coffey, and P. G. Kik, Appl. Phys. Lett. **93**, 233120 (2008).